Interfacial Microrheology of Biological Films

by

Daniel B. Allan

A dissertation submitted to The Johns Hopkins University in conformity with the requirements for the degree of Doctor of Philosophy.

Baltimore, Maryland

December, 2014

Abstract

This thesis reports experimental studies of the rheology of biological materials, with an emphasis on interfacial layers, including protein layers and bacterial biofilms. Results are presented on layers formed by the proteins lysozyme and Staphylococcal nuclease at the air–water interface, on biofilms formed by Pseudomonas bacteria at the oil–water interface, and on the bulk rheological properties of fibrin and cystic fibrosis mucus with an eye toward its role as an interfacial barrier in the lung. The evolution of interfacial mechanical response through time is interpreted in terms of the changing microscopic structure of the layer.

The studies employ interfacial microrheology, which uses the motion of micrometer-scale particles embedded in the interface to probe the mechanical response of the surrounding material and infer its rheology. Passive measurements, which rely on thermal forces to drive the particles, are complemented by active measurements, in which ferromagnetic nanowires were rotated using magnetic fields. Additionally, the study of fibrin and cystic fibrosis mucus employs a novel technique using custom fluorescent particles that can be selectively "switched on" and used to characterize

ABSTRACT

rheology and particle mobility over physiologically relevant time and distance scales.

This thesis also presents a software toolkit, developed as part of the thesis work to meet the demands of this research, that has found applications by other researchers in other areas.

This work was conducted under the supervision of Professor Robert L. Leheny and Professor Daniel H. Reich.

Primary Reader: Professor Robert L. Leheny

Secondary Reader: Professor Daniel H. Reich

Acknowledgments

First, I am grateful to Bob Leheny for his mentorship. He has been encouraging, patient, generous with his insight and his talent for communicating research, and unfailingly available and attentive. I am also grateful to Dan Reich for his incisive guidance. Together, they have given me great opportunities and provided detailed attention to prepare me to succeed. Additionally, I thank my thesis committee: Prof. Kate Stebe, Prof. Mark Robbins, Prof. Mike Bevan, and Prof. Joelle Frechette. Special thanks go to Mark, as well as Prof. Alex Szalay, for helping support and develop my interest in computing.

Many generous collaborators have enriched my work and brightened my experience. Kate Stebe welcomed me to her group and inspired me with her vigorous enthusiasm. I thank Liana Vaccari for sharing her project with me and accompanying me through the demanding rite of the 24-hour measurement. Likewise, I thank everyone in the Hanes group and in particular Ben Schuster for sharing his broad knowledge and for inviting me to contribute to his exciting projects. I am indebted to Marek Cieplak for involving me in his work and exposing me to a different aspect

of our field. And I am lucky to have found Tom Caswell and Nathan Keim, who have dwelled with me in the details of particle tracking. I have enjoyed great luck in working with many talented undergraduates, including Steve Cardinali, Daniel Firester, Victor Allard, and Bilyana Tzolova, whose dedicated efforts drove much of the work presented here. I am grateful to my predecessors in the Leheny and Reich labs for the tools they built and the guidance they provided—especially Myung Han Lee, Stuart Kirschner, Nate Capallo, Hongyu Guo, and Joel Rovner. Kui Chen, Tristan Sharp, Dan Richman, Nik Hartman, and Nuala McCullagh also provided insights and deeply appreciated camaraderie.

Finally, I am grateful to my father for teaching me that childlike curiosity has no age limit, to my mother for her cheer and encouragement, to my brother for his loyal friendship and inspiring courage, to Kelly for her unwavering confidence and loving support, and to all friends and family who have made these years of study and research enjoyable.

Contents

List of Figures

Chapter 1

Introduction

1.1 Rheology

1.1.1 Fundamentals

Hooke's Law describes a solid as an idealized spring. A small deformation requires an applied force. The larger the deformation, the larger the requisite force, but the force does not depend on the *rate* of the deformation: fast and slow cost the same. A viscous liquid, as described by Newton's laws, behaves in a complementary way: it resists a small strain with a force proportional to the rate of strain but independent of the magnitude of that strain.

Real materials deviate from these simple pictures in two ways. First, if the force or deformation is large, the relationship between the applied stress and the strain (or,

for liquids, strain rate) becomes more complicated than simple proportionality; the response is nonlinear. Second, even if the forces and deformations are small, some materials display both solidlike and liquidlike characteristics. For example, many materials respond elastically on short time scales but flow over long time scales. This temporal behavior reflects a spectrum of relaxation times that is dictated by the material's microstructural dynamics. Materials like these are termed viscoelastic.[2]

The theory of linear viscoelastic materials begins with a constitutive relation, a rheological equation of state relating stress σ to strain γ. The equation states that changes in strain are linear. The shear modulus G is a memory function representing the ratio of stress to strain through a given strain history.

$$\sigma(t) = \int_{-\infty}^{t} G(t - t')\dot{\gamma}(t')\, dt' \tag{1.1}$$

Let us apply this principle to a simple oscillatory strain, where a material is periodically deformed with some amplitude γ_0 at some frequency ω.

$$\gamma(t) = \gamma_0 \sin \omega t \tag{1.2}$$

Eq. (1.1) gives

$$\begin{aligned}\sigma(t) &= \int_0^\infty G(t-t')\gamma_0\,\omega\cos(\omega t')\,dt' \\ &= \gamma_0\,\omega\int_0^\infty G(\Delta t)\cos[\omega(t-\Delta t)]\,d\Delta t \\ &= \gamma_0\left(\left[\omega\int_0^\infty G(\Delta t)\sin\omega\Delta t\,d\Delta t\right]\sin\omega t + \left[\omega\int_0^\infty G(\Delta t)\cos\omega\Delta t\,d\Delta t\right]\cos\omega t\right)\end{aligned} \tag{1.3}$$

Because the bracketed factors depend only on ω, we can define new functions $G'(\omega)$ and $G''(\omega)$, giving

$$\sigma(t) = \gamma_0\,(G'(\omega)\sin\omega t + G''(\omega)\cos\omega t). \tag{1.4}$$

The storage modulus $G'(\omega)$ characterizes the solidlike response, where stress $\sigma(t)$ and strain $\gamma(t)$ are in phase, and the loss modulus $G''(\omega)$ gives the liquidlike response, where stress is 90° out of phase with the strain and hence in phase with the strain rate. They comprise the real and imaginary parts of the complex shear modulus, $G^*(\omega) = G'(\omega) + iG''(\omega)$, which is a fundamental linear response function and a quantity through which contact between theory and experiment is often achieved.

$G^*(\omega)$ provides a complete description of a material's linear shear response. Finite stresses and deformations can reveal rich nonlinear responses, including a yield stress (some nonzero stress above which a solid no longer responds elastically but instead undergoes viscoplastic flow) or shear-thinning or -thickening (where the effective viscosity of the fluid decreases or increases with the applied strain rate).

1.1.2 Measurement Techniques

There is a large family of well-established techniques for measuring a material's frequency-dependent shear modulus $G^*(\omega)$ and nonlinear response. The stress–strain relationship can be probed in either direction, by applying a certain stress and measuring the resultant strain or by measuring the stress necessary to enforce a certain strain. For example, a creep experiment measures the strain in response to a sudden stress, whereas a stress relaxation experiment measures the stress following a sudden strain. Both of these are transient experiments, observing the material's response as a function of time after a sudden change. Oscillatory experiments provide complimentary information, applying a periodic stress or strain at some frequency ω, qualitatively probing the same response as a transient experiment at time $t = 1/\omega$. Oscillatory experiments are especially important for probing short-time scale or (high-frequency) behavior.

Shear rheology measurements, whether transient or oscillatory, strain-controlled or stress-controlled, can be performed in different geometries. Important ones include simple shear flow between translated parallel plates or, equivalently and more commonly, between a rotating cone and plate; shear between rotating coaxial cylinders (Couette geometry); flow inside a rectangular slit; and shear between two rotating parallel plates.

All of these are, of course, subject to limitations. In oscillatory experiments the inertia of the rotating tool can dominate the shear response of the sample at high

frequencies. Also, all experiments contend with the problem of slip, the possibility that the sample might lose mechanical contact with a bounding surface where its velocity is assumed to be zero with respect to the surface.

1.1.3 Interfacial Rheology

Interfacial layers at the boundary between two fluids can exhibit the same complex, non-Newtonian, and nonlinear behavior observed in bulk materials. The central experimental challenge in characterizing these interfaces is isolating the interfacial rheological response from the response of the surrounding fluids, as the flows at the interface and in the bulk fluids are intimately coupled.[3] The relative contribution of surface and bulk forces on a rheological probe is captured by the Boussinesq number[4]

$$\mathrm{Bo} = \frac{\eta_s}{l(\eta_1 + \eta_2)} \tag{1.5}$$

where η_s is the surface viscosity and $\eta_{1,2}$ are the bulk viscosities of the fluids above and below. In many experiments, these viscosities of the fluids are matched ($\eta_1 = \eta_2$) or else one is air and can be neglected ($\eta_1 + \eta_2 \approx \eta_2$). Surface viscosity and bulk viscosity differ by a dimension of a length, and a length scale l is introduced. The definition of l depends on the particulars of the geometry of the technique. Heuristically, l is sometimes presented as the ratio of the interfacial surface area subtended by the probe to its perimeter of contact with the interface. However, this picture of l does

not hold, even qualitatively, for some geometries, such as a rod.[5]

For $Bo \gg 1$, interfacial drag dominates the force on the rheological probe. For $Bo \ll 1$, forces from the bulk fluid dominate. Thus, a well designed technique maximizes Bo by minimizing l. And, unless the contribution from the bulk is negligible, the technique must have an accompanying model for separating the interfacial and bulk contributions.

Eq. (1.5) applies to a simple viscous interface, but Bo can be generalized for viscoelastic interfaces:[6]

$$\mathrm{Bo}(\omega) = \left| \frac{G_s''(\omega) - iG_s'(\omega)}{\omega l(\eta_1 + \eta_2)} \right| \tag{1.6}$$

Experimental techniques tackle the challenge of isolating the interfacial response in very different ways. One approach employs a bicone (two cones joined at the base, giving a diamond-shape profile) or disk lowered onto the surface such that its edge is even with the interface, operated like a traditional rotating-tool rheometer. The torque on the tool is separated into the components using methods of continuum mechanics,[4] initially worked out by Boussinesq himself[7] and later refined.[8] The tool makes a full circular patch in the interface and couples strongly to bulk flows, diminishing its sensitivity to the interfacial rheology. This is quantified by the Boussinesq number: the length scale l is related to the radius of the tool, diminishing Bo for given viscosities η, η_2, η_s.

A newer technique improves sensitivity by replacing the bicone with a double

wall-ring geometry.[9] The open center of the ring diminishes coupling to bulk flows, and the important scale l becomes the thin width of the ring rather than its radius.

Other techniques rely on millimeter- to micron-scale probes manipulated by applied optical or magnetic forces. The most popular of these, dubbed the Interfacial Shear Rheometer (ISR), moves a magnetic needle pinned to the interface by capillary forces through oscillatory translations along its axis[10] within a channel to create the equivalent of a parallel plate rheometer. Others use magnetic force to rotate a thin rod[11,12] or a disk[13] or in the plane of the interface. In part of the work described in this thesis, we employ a rotating micrometer-scale needle.

1.2 Microrheology

Microrheology relates the motion of colloidal particles to the rheology of the surrounding medium. Often, the motion is thermally-driven Brownian fluctuation ("passive microrheology") but in recent years the field has come to encompass "active microrheology", where colloids driven by optical or magnetic forces can probe stiffer materials and larger deformations, extending into the regime of nonlinear response.

1.2.1 Fundamentals

The fundamental relation of microrheology is the Generalized Stokes–Einstein relation (GSE). The "Einstein" part relates a statistical characterization of probe

motion (probe mean-squared displacement $\langle \Delta r^2 \rangle$) to a deterministic property (mobility M), which the "Stokes" part then relates to the rheological properties of the material. For a spherical probe of radius a diffusing in a viscous medium at low Reynolds number, the Stokes–Einstein relation gives

$$\langle \Delta r^2(t) = \frac{N k_B T}{6\pi\eta a} \tag{1.7}$$

for the N-dimensional mean-squared displacement. The Generalized Stokes–Einstein relation posits a frequency-dependent mobility $M(\omega)$ or, equivalently, hydrodynamic drag $\zeta(\omega)$. As originally derived[14,15] and later reviewed in detail,[16] the GSE can be obtained from the generalized Langevin equation, an equation of motion incorporating a random thermal force f_R and a frequency-dependent hydrodynamic drag ζ.

$$m\dot{v}(t) = f_R(t) - \int_0^t \zeta(t-t')v(t')\,dt' \tag{1.8}$$

Because the random force f_R is stochastic, $v(t)$ must be treated statistically. Temperature T is introduced through the equipartition theorem, and the uncorrelated nature of Brownian fluctuations causes f_R to drop out. At low Reynolds number, inertia is negligible compared to hydrodynamic forces, and so the term containing mass m also drops out. The result is the Generalized Stokes–Einstein equation, relating the complex frequency-dependent shear modulus $G^*(\omega)$ to the unilateral Fourier transform of the observed N-dimensional mean-squared displacement:

$$G^*(\omega) = \frac{Nk_BT}{3\pi i\omega\mathcal{F}_u\left\{\langle\Delta r^2(t)\rangle\right\}} \tag{1.9}$$

Alternatively, the GSE can be written in terms of the complex shear compliance $J(t)$,[16] which is related to shear relaxation modulus $G(t)$ through $\int J(t)G(t)\,dt = 1$.[2]

$$J(t) = \frac{Nk_BT}{3\pi a\langle r^2(t)\rangle} \tag{1.10}$$

This expression has the advantage of being algebraic, and thus does not require the data to undergo a numerical integral transform.[17]

1.2.2 Interfacial Microrheology

As described in Section 1.1.3, experimental techniques for measuring interfacial rheology should maximize their sensitivity to the interface relative to the bulk (i.e., maximize Bo), and they should include a procedure for separating the interfacial and bulk contributions. Interfacial microrheology faces the same challenge. Because microrheological probes are typically micron-scale, the geometrical length scale l is small, and sensitivity to the interface is high relative to macrorheology techniques. This sensitivity allows microrheology to characterize interfaces with much smaller interfacial viscosity. Specifically, when microrheological probes are confined to an interface, the technique can be sensitive interfacial viscosities as small as 1 nPa·s·m, several orders of magnitude below the range of traditional techniques, and it can characterize

shear response over a wide of range of frequencies (10^{-2}–10^{4} Hz).[18] Nonetheless, coupling to the bulk at some point becomes appreciable; the problem of separating the contributions of bulk and interface must still be addressed.

Despite these challenges, microrheology has found increasing application in the study of films at fluid-fluid interfaces including not only protein layers[11,12,102–104] but also polymer layers,[23,105,106] lipid monolayers,[107–111] and particle-laden interfaces.[112,113] This work has included studies of both the linear shear rheology and nonlinear mechanical response of interfacial films.

1.2.3 Translational drag on a sphere at an interface

For viscous layers, the translational drag ζ on a circular inclusion in a membrane was first determined by Saffman and Delbruck, who showed that a physically meaningful description of interfacial Stokes drag must incorporate coupling to the surrounding bulk phase(s).[19] Considering this coupling, they derived a form for ζ,

$$\frac{1}{\zeta} = \frac{1}{4\pi\eta_s}\left(\ln(\mathrm{Bo}) - \gamma\right) \tag{1.11}$$

where $\mathrm{Bo} = \eta_s/[(\eta_1+\eta_2)\,a]$ for a sphere of radius a and γ is Euler's constant (0.5772...). The Saffman–Delbruck expression is invalid at low Bo. When $\log(\mathrm{Bo}) < \gamma$, it gives $D < 0$, which is of course unphysical. A more general form was worked out by Hughes[20] and reduced to a closed form by Petrov and Schwille:[21]

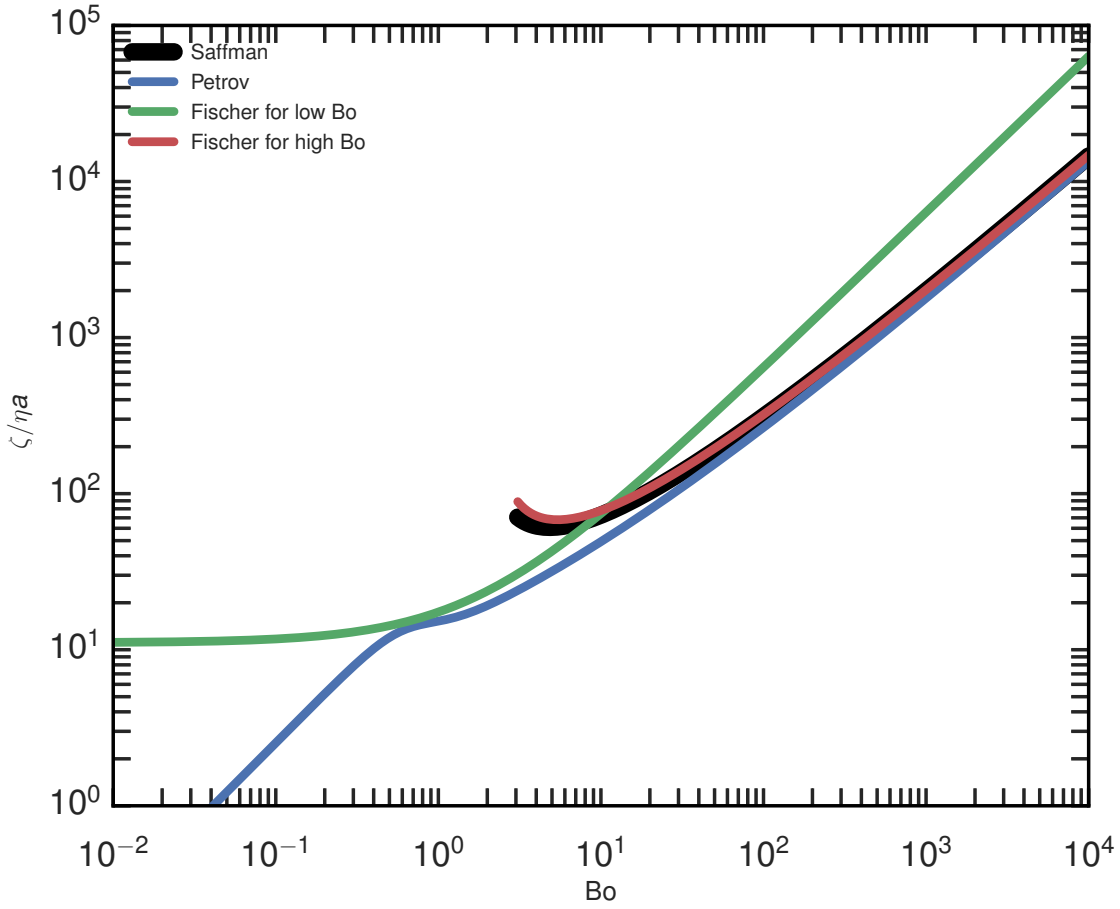

Figure 1.1: A comparison of models for the translation drag on a membrane inclusion. This figure is closely modeled after one by Samaniuk,[1] simply comparing more models.

$$\begin{aligned}\frac{1}{\zeta} =& \frac{1}{4\pi\eta_s} \\ &\times \ \ln(2/\epsilon) - \gamma + 4\epsilon/\pi - (\epsilon^2/2)\ln(2/\epsilon) \\ &\times \ \left[1 - (\epsilon^2/\pi)\ln(2/\epsilon) + c_1\epsilon^{b_1}/(1 + c_2\epsilon^{b_2})\right]^{-1}\end{aligned} \tag{1.12}$$

where ϵ is the inverse Boussinesq number 1/Bo and the numerically-determined constants are $c_1 = 0.73761$, $b_1 = 2.74819$, $c_2 = 0.52119$ and $b_2 = 0.61465$.

A more elaborate model, the Fischer model, accounts for the contact angle θ of a spherical inclusion and the effect of Marangoni forces—surface tension gradients produced by concentration gradients across the interface. At $\mathrm{Bo} \ll 1$, the Fischer model gives the translation drag coefficient ζ as an expansion in Bo[22]

$$\zeta = \eta a(k^{(0)} + \mathrm{Bo}\, k^{(1)} + o(\mathrm{Bo}^2)) \tag{1.13}$$

with coefficients (within 3% accuracy)

$$k^{(0)} \approx 6\pi\sqrt{\tanh[32(d/a+2)/9\pi^2} \tag{1.14}$$

$$k^{(1)} \approx -4\ln\left(\frac{2}{\pi}\tan^{-1}\left(\frac{d+2a}{3a}\right)\right) \tag{1.15}$$

where d is the distance from the apex of the particle to the level of the interface; d is defined to be positive when the particle is fully submerged and negative when the particle is partially embedded. Assuming gravitational and capillary effects are negligible, so that the surface remains flat in the vicinity of the sphere, d can be expressed in terms of the contact angle θ_c as $d = a(\cos\theta_c - 1)$.

In the opposite limit, $\mathrm{Bo} \gg 1$,

$$\zeta = \eta a\left(\frac{4\pi\mathrm{Bo}}{\ln(\mathrm{Bo}\, a/a_s) - \gamma}\right). \tag{1.16}$$

where a_s is the cross-section of the particle at the interface and γ is the Euler number. When Eq. (1.13) and Eq. (1.16) are plotted together in Figure 1.1, boldly extended through and beyond the domains of mathematical validity, including through $0.1 \ll \mathrm{Bo} \ll 10$ where neither is valid, we see agreement at least up to the order of magnitude throughout. As has been previously observed,[1] this agreement may explain the surprising agreement between different theoretical approaches.[23]

1.2.4 Rotational drag on a rod at an interface

As with the diffusivity of the spheres, the mobility of rods rotating at an interface depends on both the interfacial and subphase properties. The relative importance of these contributions can be parametrized by the appropriate form for Boussinesq number. For a highly anisotropic object, such as a wire-shaped colloid, it has been theorized[5] that the characteristic length scale entering the Boussinesq number is the wire length L and that the rotational drag is independent of the object's aspect ratio.

$$\mathrm{Bo} = \frac{\eta_s}{L(\eta_1 + \eta_2)} \tag{1.17}$$

A theory developed by Levine and MacKintosh predicts[5] rotational drag coefficients for all Boussinesq numbers. Measurements on Ni nanowires within viscous protein layers comparing the drag for translation parallel to the wire axis $\zeta_\parallel$ with ζ_r indicate that the results of this theory accurately predict $\zeta_\parallel/\zeta_r$,[12] and we use Levine and MacK-

intosh's theory to analyze the wire rotation. Specifically, we employ their predictions in the limit of high and low Bo: $\zeta_r \to 1.48\eta_s L^2$ and $\zeta_r \to 0.50\eta L^3$, respectively.

1.3 Topics of Thesis Research

In my thesis I have developed passive and active interfacial microrheology techniques and applied them to a set of biological systems including protein layers and bacterial biofilms. A brief introduction to each of these is given in the subsection below, and a detailed description of experiments and results is given in Chapters 4–6. First, in Chapters 2 and 3, I elaborate on the experimental methods in particle tracking and data analysis. Chapter 7 describes related work developing a microrheology method using photoactivated fluorescent nanoparticles to track the motion through biological gels over multiple length scales.

1.3.1 Protein Layers

Under many circumstances proteins adsorb at air–water interfaces.[24] Like small-molecule surfactants, interfacial proteins can stabilize emulsions and foams by reducing surface tension or by forming coalescence-arresting viscoelastic skins on the surfaces of drops and bubbles.[25,26] The surfactant-like character of proteins is crucial to many current and developing technologies, particularly those related to the food, biomedical, and pharmaceutical industries. In addition, interfacial protein lay-

ers perform physiological functions in vivo.[27,28] Proteins at fluid interfaces typically change their conformations, i.e., denature, in a way that reduces their free energy by bringing to the surface the hydrophobic parts that are normally folded inside the structure, shielded from the surrounding water. This unfolding can make adsorption irreversible, and hence equilibrium between interfacial proteins and those in the bulk solution is lost. At sufficient concentration, interfacial protein layers can acquire pronounced viscoelastic behavior[24,29–31] that has been attributed either to the formation of a gel-like network through intermolecular bonding[30–36] or to kinetic arrest due to steric jamming.[37–40] In many cases this elasticity is key to protein layers' utility. For example, mechanically strong interfacial layers resist tangential stresses from flow in the adjoining liquids, preventing rupture and coalescence of droplets and bubbles. Further, the properties of protein layers can provide a unique perspective on issues of protein denaturation, protein-protein interactions, and the gel transition.

Due to the importance of the mechanical properties of protein layers, numerous experiments have sought to characterize their interfacial shear rheology.[28,30,32–34,34,35,37–49] These studies have had to contend with the significant technical difficulties inherent to interfacial rheology, as addressed in the previous section. Additionally, protein layers are fragile, molecularly thin, and spatially heterogeneous with properties that evolve with time. These features complicate traditional interfacial rheometry measurements and often make results difficult to interpret. Interfacial microrheology, introduced in Section 1.2.2, is ideally suited to address these difficul-

ties.

In Chapters 4 and 5 of my thesis, I describe my work applying microrheological techniques to two layer-forming protein systems, lysozyme and Staphylococcal nuclease (SNase). The studies included passive measurements, which tracked the Brownian motion of spherical colloids at the interface, and active measurements in which the rotational motion of magnetic nanowires at the interface was employed to infer layer rheology. The motivation for studying these specific systems and details about the experimental procedures are given in the respective chapters.

1.3.2 Bacterial Biofilms

At a fluid interface, bacteria form a biofilm—a film of bacteria and its products—and this film can alter the mechanical properties of the interface. Specifically, the film comprises adherent cells in a complex matrix of extracellular polymeric substances including polysaccharides and surfactants secreted by the bacteria.[50] These films thus resemble from a physical-sciences perspective a disordered colloidal suspension with added polymer. Composite materials of this type can be expected to possess mechanical properties characteristic of disordered and glassy complex fluids and soft solids. Indeed, research has shown how complex fluids, such as polymers mixed with colloids, can form soft glassy phases under a range of conditions.[51–54] These phases are distinguished by novel mechanical properties including thixotropic response to stress and anomalous low-frequency viscoelastic moduli.[51–54] In addition, these

disordered materials are typically out of equilibrium, and their mechanical behavior can evolve perpetually, a process known as aging.[51,54] Many of these properties are associated with metastable heterogeneous structure in these mixed systems and strong mechanical coupling between components. Theory exploring the dynamics and aging of soft glassy systems has emphasized their apparent universality.[55–58] Recent research has also identified characteristics shared by biofilms formed on solid substrates and such glassy soft solids.[59–62]

Bacterial biofilms can form at the interface between oil and water, and the bacteria that form such films typically consume the oil. Much research has been devoted strategies that increase the speed and ability of the bacteria to degrade pollutant hydrocarbons.[63,64] Additionally, the mechanical behavior of interfacial biofilms between oil and water is thought to directly influence petroleum extraction. Stiff films can limit the ability of oil droplets to pass through narrow pores and channels, competing with other effects of the bacteria, specifically reductions in interfacial tension and viscosity, that promote recovery. On the other hand, the formation of stiff interfacial films has also been advanced as a mechanism for the clogging of highly permeable regions of reservoirs that aids in enhanced recovery.[65] Despite this significance, few studies have reported on the mechanical properties of bacterial films at oil-water interfaces. The in-plane mechanical behavior of an interfacial film is characterized by its response to two modes of deformation: its shear modulus, which describes the response to area-conserving deformations, and its dilational modulus, which describes

the response to changes in area. Previous research on the mechanical behavior of bacterial films at an oil-water interface has focused exclusively on their response to dilational stress,[66,67] leaving key aspects related to their shear rheology unexplored.

Such information is crucial for understanding the films mechanical response both from a fundamental perspective and in the context of applications of hydrocarbon-consuming bacteria and their biofilms. For example, the resistance to tangential stresses provided by the shear modulus can dictate the stability of an interfacial layer to rupture.[68] In addition, analysis of shear rheology can give access to interaction forces in an interfacial layer, shedding light on the mechanisms dictating the strength and compliance of the films.[41] Chapter 6 describes experiments that address these important issues by investigating the linear shear rheology of model bacterial films at an oil-water interface.

Chapter 2

Experimental Methods

2.1 Experimental Challenges in Interfacial Particle Tracking

2.1.1 Colloidal Aggregation at the Interface

When microrheological probes aggregate, the colloidal aggregate does not retain the simple geometry of an individual colloid and therefore is of no further use in the experiment. It is straightforward to visually identify aggregated probes and disregard them in the analysis. But each aggregation event depletes the population of usable probes and limits the experiment's duration.

This problem is especially acute in interfacial experiments because, at the air–

water interface, microrheological probes have an enhanced tendency to aggregate. The lower spatial dimension of the interface increases the probability that probes will encounter each other. The van der Waals interaction between partially-immersed colloids is more complex than their interaction in bulk solution, which itself is complicated;[69] but, on a basic level, the strength of the attraction is intermediate with respect to strengths of the interactions in the two pure phases. Particles at the air–water interface interact more strongly than submerged particles due to the dry portion. As a point of reference, for polystrene spheres, there is seven-fold difference in the strength of van der Waals attraction between fully submerged and unsubmerged colloids.[70] Additionally, the stabilizing electrostatic repulsion between charge–stabilized colloids diminishes as it de-wets, which further magnifies the net attraction.[70,71] The attraction may also be increased by a depletion interaction driven by the adsorbed molecules under study (in this case, proteins or bacterial byproducts). Finally, while the capillary attraction of "floating" particles is the most obvious driver of aggregation at the interface, it is weak for the systems in this study, which are characterized by a low Bond number $\Delta\rho g a^2/\gamma$.

In this work, the charge–stabilized colloids used (see methods sections of respective chapters for details) did indeed aggregate throughout the experiment. However, the evolving mechanical properties of the interface under study often inhibited colloidal mobility as the interface stiffened and effectively arrested aggregation before the population of unaggregated probes could be completely depleted. Some control could

be exerted over the aggregation rate by varying the salt concentration of the bulk solution and by adjusting the concentration of dispersed colloids. At lower concentrations, the colloids are of course less likely to encounter each other, and aggregation proceeds more slowly.

2.1.2 Distinguishing Interfacial Particles

When colloidal probes are spread onto the interface, many can be pinned there, but some invariably enter the bulk solution. As they undergo random diffusion in the bulk, they may approach the interface, where they can easily be mistaken for particles that are at the interface. Thus, in interfacial particle-tracking experiments, it is important to critically examine individual particles, considering whether particles exhibiting an anomolous appearance or anomolous motion may not be attached to the interface. This has been an important, if mundane, challenge to address in this work. It has recently been emphasized in the literature by others,[1] and part of the motivation for developing flexible particle-tracking software (Chapter 3) that makes this detailed work easier.

2.1.3 Minimizing and Correcting for Convective Drift

When possible, the chamber containing the sample should be well sealed to minimize sample evaporation and convective flow during the experiment.[72] In interfacial microrheology experiments, convective flow is an especially large effect, as the interface can couple strongly to surrounding air currents. In the data analysis stage, the effect of such currents can be corrected for,[73] but it is best to minimize it in the experiment as much as possible. The experiment should be performed on a vibration-isolated table. Like convective drift, vibrations can be "removed" in the analysis stage, but not perfectly.

2.1.4 Choosing an Appropriate Particle Concentration

Obviously, the more particles that are in the fields of view and are tracked, the better the resulting statistics; however, there are additional considerations. As mentioned above, the particle concentration affects the rate of particle aggregation, but there are other considerations as well. The concentration must be appropriate for tracking individual particles. The average particle spacing must be larger than the average particle displacement from frame to frame, or else the paths of multiple particles will

intermingle, making it difficult to accurately reconstruct individual trajectories.[74] (In some circumstances, it is possible to overcome this limitation, as described in Section 3.5.)

Additionally, the presence of the colloidal probes themselves can alter the self-diffusivity of the probes through hydrodynamic interactions,[75] which are longer-range in 2D than in 3D ($\log(r)$ vs. $1/r$). Experimental measurements of the diffusivity of PMMA particles showed that diffusivity D decreased with area fraction n like

$$D = \alpha D_0(1 - \beta n) \tag{2.1}$$

where D_0 is the diffusivity for a single particle. For particles 1 μm in diameter, α is compatible with 1 (reported as $0.97 \pm 7\%$) and $\beta = 1.4 \pm 10\%$.[75] Thus, if spherical colloidal probes are dispersed with an area fraction of 3%, the resultant error in diffusivity is less than 5%, which is small compared to other experimental uncertainties in this work.

2.2 Experimental Apparatus

All interfacial microrheology experiments described in this thesis were performed in a cylindrical "cell" designed to create flat interface air–water or oil–water interface using only a small volume of sample. This cell (Figure 2.1) is a short cylinder: 4 mm high with a 1-cm inner diameter. A seam runs along the waist of the inner surface, 2

mm above the bottom surface, composed of aluminum below and Teflon above. When the cylinder is filled precisely up to this seam with an aqueous solution, the solution is pinned flat by the aluminum-Teflon boundary. There is no meniscus. A glass coverslip serves as a bottom to the cell, through which the interface can be imaged using an inverted microscope. (The interface can also be imaged from above using a standard microscope, as in Chapter 6.) This coverslip is held in place by a thin coat of vacuum grease, applied to the bottom surface of the cylinder. Alternatively, a grease-free seal can be made using a custom-molded PDMS sheath that seals the outer surface of the cell to the glass below.

Consumer-grade cameras are sufficient for some bright-field particle-tracking applications, delivering the same basic capabilities as scientific cameras—frame rate, resolution—at a fraction of the cost. (In fluorescent particle-tracking experiments, where sensitivity is paramount, special cooling and readout electronics are more important.) In a previous study and in preliminary experiments leading to this work, our lab used a "point-and-shoot" consumer camera (Nikon COOLPIX 4300). The sensor was physically small, which led to greater noise, and the video data was compressed in a way that can distort motion. For the study described in Chapter 4, to increase the signal-to-noise ratio and improve the fidelity of the video data, this was replaced by a digital SLR-style consumer camera (Nikon D3100) with a larger sensor and the capability of exporting uncompressed video. Data from these consumer-grade cameras was supplemented with data from a scientific camera capable of high

Figure 2.1: The experiments in this thesis were performed in the cylindrical Teflon and aluminum cylinder at left. The Teflon–aluminum seam on the inner surface pins the air–water or oil–water interface flat. A glass coverslip forms the bottom, attached and sealed using a thin coat of vacuum grease. A quarter is shown for scale.

frame rates (Photron Fastcam 512) and, for the experiments described in Chapter 5, a high-resolution scientific camera (IOIndustries Flare 4M). The studies described in Chapters 6 and 7 were performed using hardware described in detail in their respective sections on experimental methods.

2.3 Ferromagnetic Nickel Nanowires

2.3.1 Overview of Fabrication and Characteristics

Ferromagnetic nickel nanowires were fabricated for use in active microrheology experiments. The wires can be made 5–35 μm long (10% length polydispersity[76,77]) with a diameter of 350 ± 40 nm.[76,77] Because their diameters are comparable to the characteristic size of a magnetic domain in bulk nickel and their aspect ratio is high, the wire's magnetic domains are aligned with the long axis. Their remnant magnetization is 70% of the saturation of bulk nickel[78] with a magnetic moment per unit length of $3.0 \times 10^{-14} \pm 0.6\,\mathrm{A \cdot m^2/\mu m}$. Thus, they couple strongly to externally applied magnetic fields, and they act as strong, robust probes of soft–matter systems.

The wires were fabricated by electrochemical deposition inside the pores of a nanoporous template: a ceramic filter, obtained commercially and repurposed for this technique. The detailed protocol has been described both in published literature[79] and a thesis.[80]

The dominant source of the uncertainty in the figure for μ/L cited above is the

uncertainty in the wire diameter. The length can be estimated visually in brightfield experiments, but the diameter cannot. The variation in magnetization under experimentally applied fields is under 10%.[76,77] For more detailed characterization of the wire's magnetic properties, see the referenced literature.

2.3.2 Hydrophobic Functionalization

The nickel nanowires are functionalized to create a more hydrophobic surface. When they are dispersed across the air–water interface, plain nickel wires would sink, but hydrophobially functionalized wires are pinned at the interface and can remain stably at the interface for many hours. The nanowires are functionalized in a mixture of 0.01 ml *n*-octadecyltrimethoxysilane (OTMS), 0.01 ml ammonium hydroxide, and 10 ml ethanol. The wires are soaked this mixture for 12 hours. Then, after at least three rises in pure ethanol, the wires are dispersed in isopropyl alcohol (being a cleaner solvent than ethanol) for storage and use. The air–water contact angle is $79 \pm 1^\circ$ at an OTMS-functionalized surface, as measured using a goniometer (Rame-Hart, P/N 100)[12] to photograph a water droplet on a plate of functionalized nickel. Typically, protocols like this one use centrifugation to recover the colloids between rinses. Because the wires are ferromagnetic, they can conveniently be separated from the solution by merely holding a magnet against the wall of the container for a few seconds and then pouring off the liquid. Alternative schemes for hydrophobic functionalization are available in the literature.[81,82]

2.4 Tracking Nanowire Orientation

The basic approach in the experiments employing the nanowires involves tracking their rotational motion in response to time-dependent external magnetic fields. The raw data of our active microrheology experiment is hence a series of video microscopy images of a rotating nanowire. The orientation of the wire must be extracted from the images. Although the orientation is plain to any human observer, an automated solution is required due to the sheer volume of data (10^5 images) and the necessity of precise and consistent judgements of an angular trajectory through time. The analysis is deceptively difficult to automate. We have developed a family of approaches, each with certain advantages. The important metrics are precision, robustness, and performance (speed).

A standard algorithm for identifying line segments in an image is the Hough Transform. Unfortunately, this is completely ineffective on our data. Although the wires are rods with a high aspect ratio, diffraction effects cause them to appear more like fuzzy ellipses than straight lines.

The simplest effective technique is to fit an ellipse to the wire's silhouette. A threshold defines regions inside and outside the wire, and a least-squares best fit obtains the ellipse that most accurately encloses that region. The orientation of the ellipse's long axis is the orientation of the wire. This is typically accurate within 1° and it is robust—it virtually always captures orientation within 10°—but it is not precise enough to track the wire's rotation smoothly.

A more precise technique is to fit a Gaussian to each individual row or column of pixels in the image, where each Gaussian's center identifies the position of the wire along that line. The linear regression of the Gaussian centers gives the centerline of the wire. This technique is precise but quite slow. Worse, it is brittle, prone to completely missing the wire orientation in noisy or otherwise non-ideal conditions.

The most effective technique is to find the "inertial axes" of the image (where brightness = mass). For an image with intensities I_i at pixels i located at (x_i, y_i), we compute its covariance matrix u.

$$\begin{pmatrix} \overline{x} \\ \overline{y} \end{pmatrix} = \begin{pmatrix} \sum_i I_i x_i / \sum_i I_i \\ \sum_i I_i y_i / \sum_i I_i \end{pmatrix} \tag{2.2}$$

$$u = \begin{pmatrix} \sum_i I_i x_i^2 / \sum_i I_i - \overline{x}^2 & \sum_i I_i x_i y_i / \sum_i I_i - \overline{x}\,\overline{y} \\ \sum_i I_i x_i y_i / \sum_i I_i - \overline{x}\,\overline{y} & \sum_i I_i y_i^2 / \sum_i I_i - \overline{y}^2 \end{pmatrix} \tag{2.3}$$

We can obtain the orientation of the wire, defined in terms of the angle of the wire axis with respect to the x-axis (i.e., the orientation of rows of pixels) from u by

$$\theta = \frac{1}{2} \tan^{-1} \left(\frac{2u_{11}}{u_{20} - u_{02}} \right). \tag{2.4}$$

The technique is much faster than fitting Gaussians, and its precision is comparable: both are precise to 0.1°. We have also found it to be more robust, though not quite as robust as the ellipse-fitting method.

All of the methods above require standard image preparation techniques. The region of interest is isolated from the surrounding image (the wire is the largest connected region of bright pixels). The image is gently blurred with a Gaussian kernel of width about 1 pixels to suppress the jagged effect of camera noise, and distant background pixels are clipped to black, but immediate neighborhood of the wire is retained.

Chapter 3

Software Development: A Modern Particle-Tracking Toolkit

A large portion of my thesis effort has been devoted to the development of particle tracking and data analysis software, dubbed "trackpy," used for my own soft matter research and the work of others in our group. It is also being adopted by other soft matter researchers at Harvard, Princeton, Oxford, U. Chicago, U. Penn, and more. Relying on the growing open-source scientific software community, I have leveraged free, widely-used code for core functionality. By contributing my own particle tracking and data analysis code back to the community, I have increased the impact of the work and encouraged others to share their own improvements to my code, from which all users benefit.

Trackpy integrates with a fast-growing tool from this community: a standardized,

browser-based notebook of multilingual code with figures, explanatory text and equations, and links and references. As recently highlighted in *Nature*,[83] these notebooks are making data analysis easier to record, understand, and reproduce. A growing number of authors are publishing these notebooks alongside papers, providing the detail that is essential for others to reproduce the work in a reasonable time scale.

Several researchers have merged their independent efforts into this code. I personally am responsible for implementing feature-finding, motion analysis tools (various statistics and plots), uncertainty estimation, streaming capability (i.e., processing unlimited data sets), and the bulk of the tests and documentation. Thomas A. Caswell wrote the original trajectory-linking code, and Nathan C. Keim contributed the prediction framework, major performance improvements, and improved trajectory linking.

3.1 Introduction

Particle tracking is an extremely powerful technique used across many disciplines of science. It has matured over the past three decades into a broadly accessible technique. Early applications were in cellular biophysics[84,85] and fundamental colloid science.[74] More recently, it has been used to directly image atomic rearrangements in silica glass;[86] to image stress and strain in drying colloidal films;[87] to image pleats in crystals on curved surfaces.[88] This broad variety of applications calls for a flexible

toolkit that can be adapted for use with a range of data analysis strategies. Making the methods used in various pockets of the literature usable in a single framework increases the reusability of those methods, makes them easier for researchers to discover, and fights the creeping fragmentation of science.

3.2 Review of the Crocker–Grier Particle Tracking Algorithm

Trackpy implements the tracking algorithm of Crocker and Grier.[74] Theirs and similar algorithms[85] have been widely used in the fields of colloid science, microrheology, biophysics, and biometrical engineering. The particle-tracking algorithm implemented by Crocker and Grier is performed in two steps: locating the particles in each frame and identifying the particles through time, linking coordinates into trajectories.

Particle coordinates are identified in four steps: 1) preparing the image using common image-processing techniques; 2) finding local maxima of brightness that may correspond to particles; 3) honing in on each candidate particle's exact center with subpixel precision; and 4) discerning which of the candidates are true particles based on their morphology and measured brightness.

The software first prepares the images by applying a spatial bandpass filter, which uses a Fourier transform of the image to suppress features with small-scale variation (e.g., camera noise) and large-scale variation (e.g., uneven lighting). This effectively

erases any objects in the background that are much smaller or much larger than the size of the particles. Next, the software identifies all local maxima in the processed image. These do not necessarily correspond to the particles' centers, but they provide an initial estimate of where particles may be found. If two or more local maxima are separated by a distance smaller than the particle diameter, they are assumed to belong to the same particle, and the software only retains the brightest one. Then, the software finds the intensity-weighted centroid (analogous to a center of mass) of each spot, which is refined through iterative steps, using the whole region of the particle to resolve its center to a precision much better than a pixel. (Subpixel resolution is discussed at length in Section 3.4.) Finally, the software characterizes the neighborhood surrounding each spot by its total brightness, size, and eccentricity (deviation from circular shape). Using these attributes, blobs that correspond to actual particles can be distinguished — and the rest discarded — with minimal user input. For example, true colloidal spheres tend to appear bright and circular. Figure 3.1 shows 1-μm colloidal spheres at the air–water interface identified by trackpy. Most aggregated particles or out-of-focus particles, which are probably below the interface, are correctly ignored based on these characteristics of their appearance.

At this point, the algorithm has identified the locations of particles in each frame. Next, the locations must be linked together across frames into particle trajectories. The algorithm robustly handles the complications of real trajectories: particles may leave the field of view, new particles may enter, and particles can even be tracked

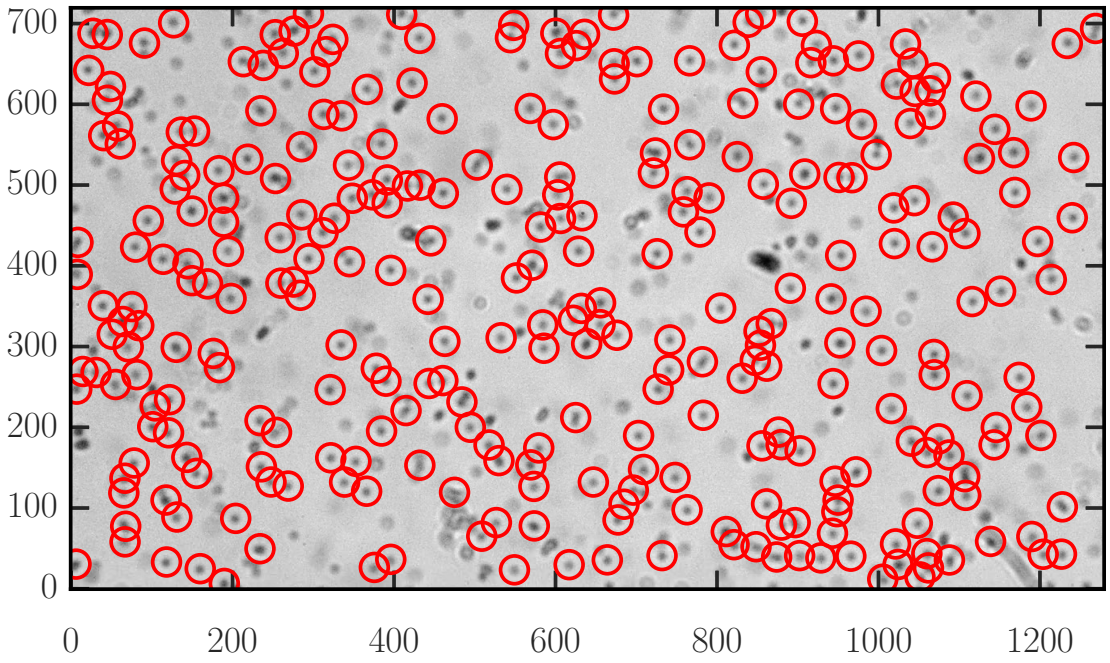

Figure 3.1: 1-μm colloidal spheres at the air–water interface identified by trackpy with a red circle. (The size of circle is arbitrary—it is only a marker.) Most aggregated particles or out-of-focus particles, which are probably below the interface, are correctly ignored based on characteristics of their appearance. The axes are labeled in pixels.

if they temporarily vanish and reappear nearby within some specified window of time. If particles are well separated and move a small fraction of their separation between frames, the task of linking them is simple and unambiguous. If there are many particles in the field of view and they are moving quickly, the Crocker–Grier linking algorithm assigns particles in a way that minimizes the total length of the links. This is grounded in the statistics of random walks; a Brownian particle is most likely to be found near where it was last seen. The algorithm is rigorously correct for non-interacting Brownian particles,[74] and it is employed effectively in a variety of tracking applications.

As the number of particles in view grows, resolving ambiguous networks is difficult. To simplify the problem, the algorithm requires the user to specify the maximum displacement allowed from one frame to the next. A good choice can simply be obtained by watching the particles and guessing the upper range of their movement between frames. Then, after trajectory linking is complete, the choice can be validated by verifying that the distribution of observed particle displacements decays short of this cutoff value, that it is not clipped.

One the appropriate parameters for feature size, appearance, and maximum displacement have been decided, a standard personal computer can typically process at least one video frame per second, though this depends on the number of particles (and therefore the number of calculations needed for a single frame) in view.

3.3 Trackpy: An Enhanced Implementation of Crocker–Grier

Many others have reimplemented the Crocker–Grier algorithm in various languages. (See table in Appendix A.) Our Python implementation is distinguished by succinct and flexible usage, modular design, scalability to data sets of unlimited size, a thorough testing framework ensuring code stability and accuracy, and thorough documentation.

To summarize some key features:

- Wherever possible, existing tools from widely-used Python modules are employed. Therefore, core functionality such as common image processing routines are supported and tested by a community of scientists much larger than the particle-tracking community.

- Alongside trackpy, we developed a utility for reading sequential images called PIMS (Python Image Sequence). PIMS handles video data from many formats with one consistent interface, abstracting away the I/O details. It is designed to process videos of unlimited size, pulling data into memory only as it is needed.

- Results from trackpy are returned as DataFrames, high-performance spreadsheet-like objects that enable powerful and convenient data grouping and reduction operations for "medium data," analogous to the capabilities of rela-

tional database systems such as Structure Query Language (SQL).

- To verify correctness and project stability, a suite of more than 180 tests reproduces basic results (Section 3.6).

- Both feature-finding and trajectory-linking can be performed on arbitrarily long videos using a fixed, modest amount of memory. (Results can be read and saved to disk throughout.)

- A prediction framework helps track particles in fluid flows, or other scenarios where velocity is correlated between time steps (Section 3.5).

- Feature-finding and trajectory-linking works on images with any number of dimensions, making possible some creative applications.

- Uncertainty is estimated following a method described in a detailed study by Savin and Doyle[72] (Section 3.4).

- High-performance components—numba acceleration and FFTW ("Fastest Fourier Transform in the West")—are used only if available. Since these can be tricky to install on some machines, the code will automatically fall back on slower pure Python implementations.

- Over fifty pages of collaboratively-written documentation with tutorials and examples is provided in Appendix A. The documentation is also, of course, available online.[89]

3.4 Subpixel precision and accuracy

Understanding the precision and accuracy of particle location is critical for conducting reliable particle tracking experiments. In fact, failure to recognize and account for imprecision and inaccuracy in tracking data can lead to qualitative misinterpretation[90,91] as random errors in particle position can become large systematic errors in derived quantities.

Tracking resolution is different than microscope resolution. As classically defined, microscope resolution is the minimum distance between two distinguishable points. The resolution of a traditional light microscope is approximately 250 nm, half the wavelength of visible light.[92] However, this limit does not apply to locating the center of one isolated point. Using an appropriate algorithm, it is possible to locate the center of an isolated particle or point source to better than the diffraction-limited resolution.[90,93] In fact, researchers can routinely track particles with a lateral spatial precision of tens of nanometers or less using a standard light microscope.[73]

How is it possible to locate a particle's center to better than pixel resolution? If a particle is only visible as one bright pixel, then we can only say that the particle is located somewhere in that pixel. But, if the particle's image spans multiple pixels—ideally, more than three pixels across—we can find its position with subpixel accuracy by taking the average position of these pixels, weighted by brightness. Figure 3.2 shows how this is realized by trackpy, comparing the measured positions to actual positions on simulated images where the ground truth is known. On real data, where

the ground truth is not known, subpixel accuracy can be checked by looking at the distribution of the decimal parts of the particle positions—that is, position modulo 1 pixel. If the algorithm is not achieving good sub pixel precision, the distribution will often be distorted, typically biased toward pixel edges. Usually this means that the area being used to compute the centroid is too small.[73] As demonstrated in Figure 3.2, enlarging that area can improve precision.

3.4.1 Static Error

Uncertainty in particle location is variously referred to as static error, localization error, or random error.[72,74,94] Tracking precision is subject to both fundamental and experimental limitations. The fundamental limitation is photon noise: a particle emits photons stochastically, and consequently, there is statistical uncertainty in locating the particle from its image. The size of this uncertainty is inversely proportional to the square root of the number of detected photons.[95] Experimental limitations related to detector and specimen properties can also degrade precision. Detector noise, including dark current (thermally-induced electrons in the detector) and readout noise (errors in reading the number of photoelectrons built up in a pixel), can interfere with particle localization.[92,96] Image processing can remove some, but not all, of this background.[90]

Simulated images in Figure 3.3 illustrate noisy images and the resultant error in particle location, as realized by trackpy. In simulated images like these, the ground truth is known. In real images, the uncertainty in particle location can be estimated.

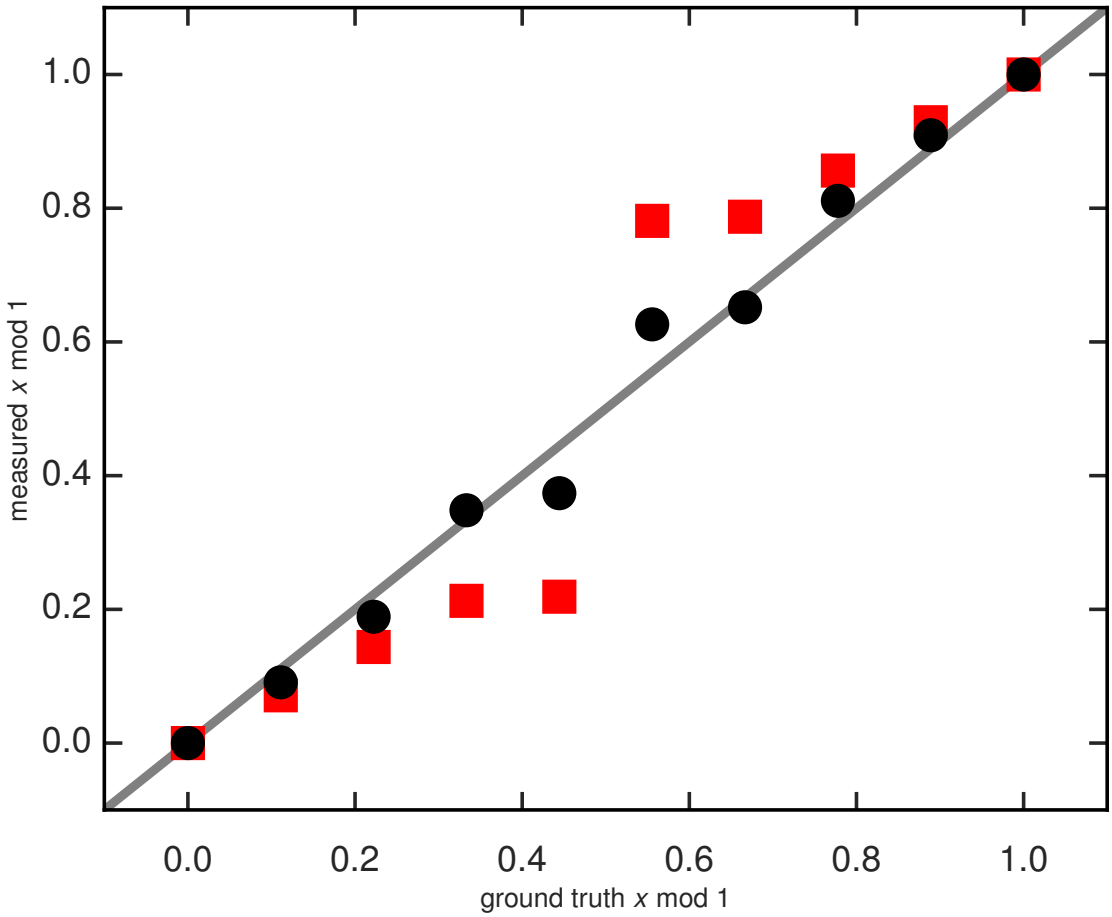

Figure 3.2: The decimal part of the x coordinate reveals sub pixel accuracy. Here the measured x coordinate is plotted against the ground truth. When the mask does not cover the edges of the feature, sub pixel accuracy is poor (red squares). In particular, the location is biased toward pixel edges. With a larger mask, accuracy is good to about a tenth of a pixel (black circles).

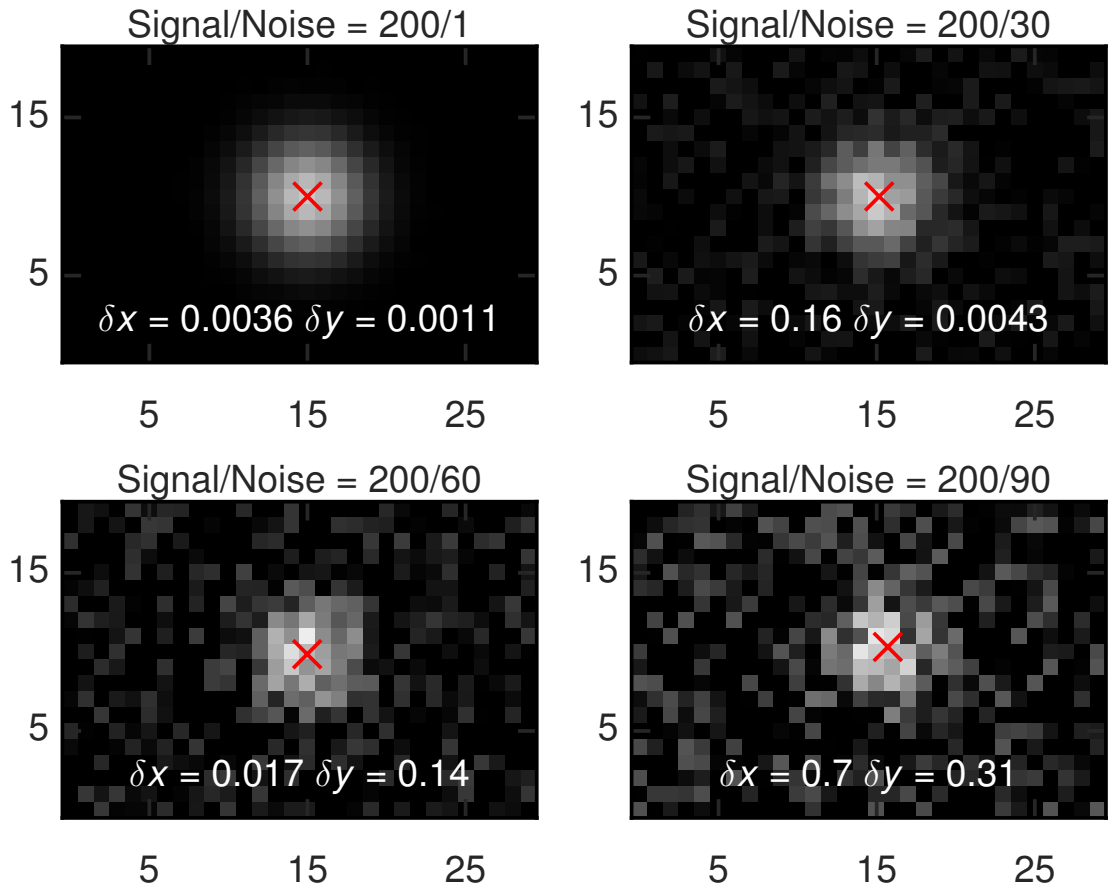

Figure 3.3: Images depict a Gaussian blob with increasing levels of simulated random noise. The red X indicates the measured centroid. Overlaid text gives the error between that measured particle position and the ground truth for each particular example.

A relation was worked out in a detailed study of particle tracking errors by Savin and Doyle.[72] For a hat-like spot, the uncertainty in location is

$$\epsilon = \frac{N}{S}\frac{l_n}{2\pi^{1/2}}\frac{w^2}{a^2} \tag{3.1}$$

where N/S is noise-to-signal; l_n=1 pixel, the length scale of noise correlation; and w and a are, respectively, the apparent size and the size of the neighborhood used to compute the centroid. Trackpy performs this computation for every particle and returns an estimate of ϵ with the location of every feature it finds. By implementing error analysis as a built-in feature, trackpy encourages researchers to consider this important detail of particle tracking data analysis.

For Brownian motion in a viscous liquid, static error adds a constant offset to the MSD, as derived previously,[94]

$$\langle \Delta r^2 \rangle_{\text{measured}} = \langle \Delta r^2 \rangle_{\text{true}} + 2\epsilon^2. \tag{3.2}$$

A perfectly immobilized particle will have $\langle \Delta r^2 \rangle_{\text{true}} = 0$ for all lag times, but because of static error, the actual measured MSD will be a non-zero constant, $\langle \Delta r^2 \rangle = 2\epsilon^2$.[73,94] However, in most particle tracking experiments, the true underlying MSD is not known *a priori*, so it may not be immediately evident how much of the measured MSD is an artifact of noise.

In addition to the random error associated with camera noise and pixelation,

particle location is subject to systematic errors, wherein particles can be biased toward certain locations, such as pixel centers. Several experimental details in both hardware and software are implicated in these errors.[73] Of course, if the particles typically step much more than a pixel between frames, optimizing subpixel resolution is less important. In this work, they are of greatest importance in characterizing layers exhibiting a solid-like response, when both Brownian fluctuations in position are typically smaller than 1 pixel and convective flow is much slower than 1 pixel per frame.

3.4.2 Motion Blur

Additional error is introduced by the finite camera exposure time. When a particle moves substantially during the exposure, the recorded image represents the time integral of the particle's location (Figure 3.4). Since particles in random walks tend to revisit previously explored regions, motion during the exposure gives a smoothed trajectory with an MSD that is systematically lower than the true MSD.[73,97] This effect has been called motion blur and dynamic error.[72] In addition, particle motion increases static error, because motion blur reduces location precision by roughly two-fold under typical experimental conditions, as compared to stationary particles.[96]

Like static error, dynamic error can alter the measured MSD, and can thus introduce inaccuracies when using the MSD to calculate diffusion coefficients and viscoelastic moduli. Static error alone adds a constant offset to the MSD, which flattens

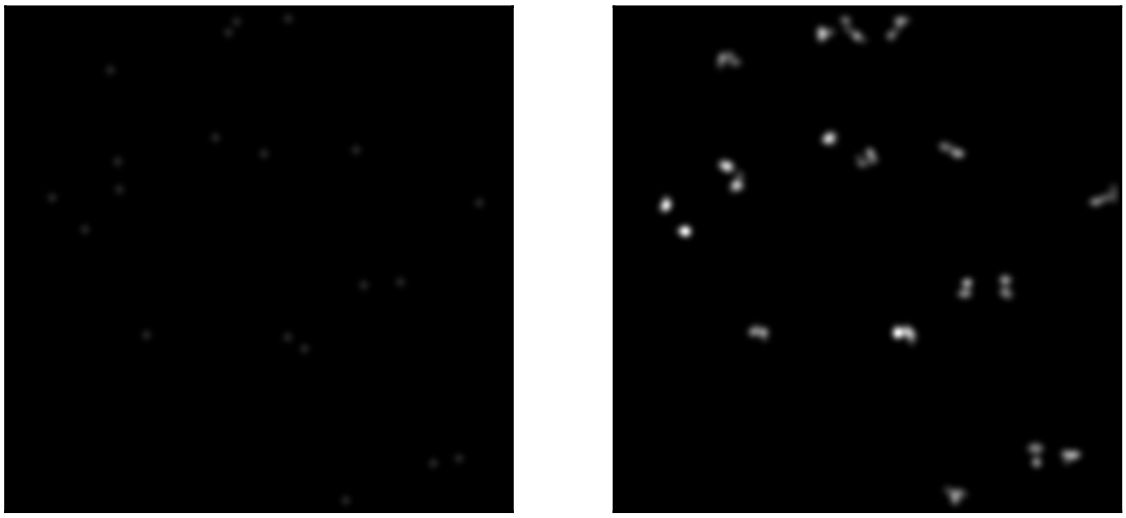

Figure 3.4: In these simulated images of diffusing Gaussian blobs, the image on the right was exposed for ten times as long as the image on the left. By collecting more light, it imaged brighter particles, but their precise location is not well defined. The optimal exposure is between these two extremes, as described in the text.

the MSD at short time scales on a log-log plot, and makes diffusive motion appear sub-diffusive.[94] Dynamic error, by itself, decreases the MSD at short time scales, which makes diffusive motion appear super-diffusive. Thus, static and dynamic error distort the MSD in opposite directions, so depending on which type of error is larger, one effect may dominate, or occasionally, the two effects may largely cancel each other.[72] Both sources of error are more pronounced at short time scales, when the true MSD is smaller.

3.4.3 Experimental Best Practices to Minimize Error

Prior to collecting data, it is critical to consider how to minimize static and dynamic error, as they are difficult to completely correct after the experiment. To boost signal-to-noise ratio and reduce static error, researchers should choose a microscope objective with large numerical aperture and a sensitive camera with low noise. The only way to reduce dynamic error is to use an exposure time that is small compared to the frame interval.[72,73] Unfortunately, shorter exposure time also increases static error. Therefore, for given experimental conditions, one should choose the shortest possible exposure time that still gives high-contrast particles (low signal-to-noise). As a point of reference,.[73]for Brownian motion, an exposure time no longer than one quarter the frame interval will cause dynamic error of less than 10% at the shortest time scale, and smaller dynamic error at longer time scales.

After conducting an experiment, dynamic error is especially difficult to correct, because it distorts the trajectory and MSD systematically in a way that varies with lag time and depends on the underlying type of motion, which is often unknown.[72] Static error is simpler to quantify and correct after the fact because static error adds a constant offset to MSD regardless of the nature of particle motion. Static error can be estimated by tracking particles fixed to a microscope slide under signal-to-noise conditions similar to those of the experiment, and then subtracted from the ensemble

MSD. However, this simple approach may not precisely mimic the background noise in the experiment, nor the effect that motion blur has on static error. An alternative method has recently been proposed for measuring localization precision of moving particles, though this technique requires a custom microscope configuration.[96] Tracking particles in water or other fluids of known viscosity and comparing their MSD to theory may also help reveal types and magnitudes of error.

3.5 Prediction Framework

The Crocker–Grier particle tracking algorithm, at its simplest level, takes each particle in a given image and tries to find it in the subsequent image. This requires knowing where to look for it. The algorithm was developed to track particles undergoing Brownian diffusion, in which a particle's velocity is uncorrelated from one frame to the next. Therefore, a particle is statistically most likely to be found at or near is last known location. The particle in a given image closest to a particle in the previous image is likely to be the same particle.

Let us formalize this argument as a *prediction*. Consider a function

$$P(t_1, t_0, \vec{x}(t_0)) \tag{3.3}$$

that takes the particle at position $\vec{x}(t_0)$ at time t_0 and predicts its most likely future position $\vec{x}(t_1)$ at time t_1. The optimal predictor for Brownian motion is

$$P(t_1, t_0, \vec{x}(t_0)) = \vec{x}(t_0) \tag{3.4}$$

which, of course, is also the simplest to implement.

The better our prediction about where to look in the next frame, the more likely we will find the one and only particle we seek. In practice, the algorithm looks for the particle in a circular region of radius `search_range`, centered on $P(t_1, t_0, \vec{x}(t_0))$. So, a particle is successfully tracked only if its true position at t_1 is sufficiently close to the predicted one. This favors a generous `search_range`. However, if `search_range` is too large, then for each particle in the previous frame there can be many possible matches in the current frame, and so matching one frame to the next requires the computer to evaluate an overwhelming set of possibilities, seeking the one that minimizes the total displacements of all particles. Tracking may become extremely slow, the problem effectively intractable. So for the Brownian P above, `search_range` must be bigger than the largest particle displacement between frames, but smaller than the typical spacing between particles.[74] If such a value does not exist, the Crocker–Grier algorithm is not effective.

However, if particle motion is not strictly Brownian, its velocity probably *is* correlated in time. We may be able to improve P. This is the justification for trackpy's prediction feature.

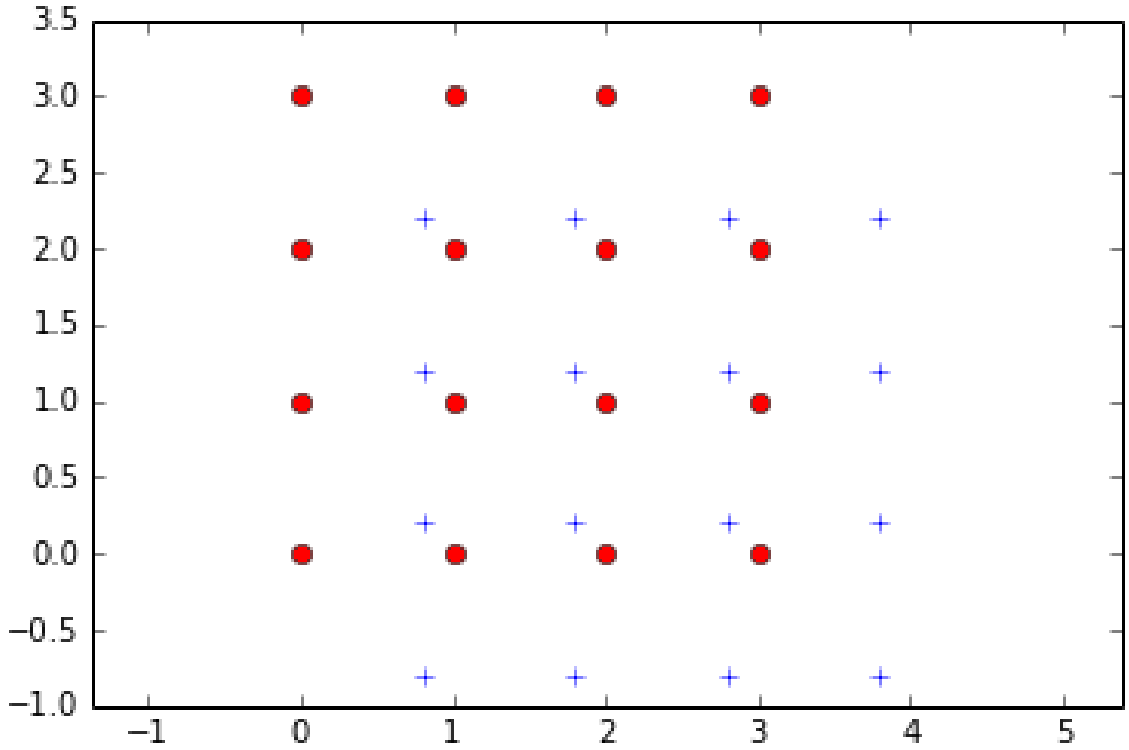

Figure 3.5: An ensemble of particles moving under constant velocity. The red circles represent their positions at some time t, the blue crosses at some later time t'.

3.5.1 Prescribed predictors

Consider a toy example: a regular array of particles, translating with constant velocity v. Figure 3.5 shows the particles' positions in two consecutive frames. Using the Brownian predictor, Eq. (3.4), trackpy links the particles as shown in Figure 3.6.

This is obviously not correct. Let us provide a P which reflects this constant

$$P(t_1, t_0, \vec{x}(t_0)) = \vec{x}(t_0) + v(t_1 - t_0) \tag{3.5}$$

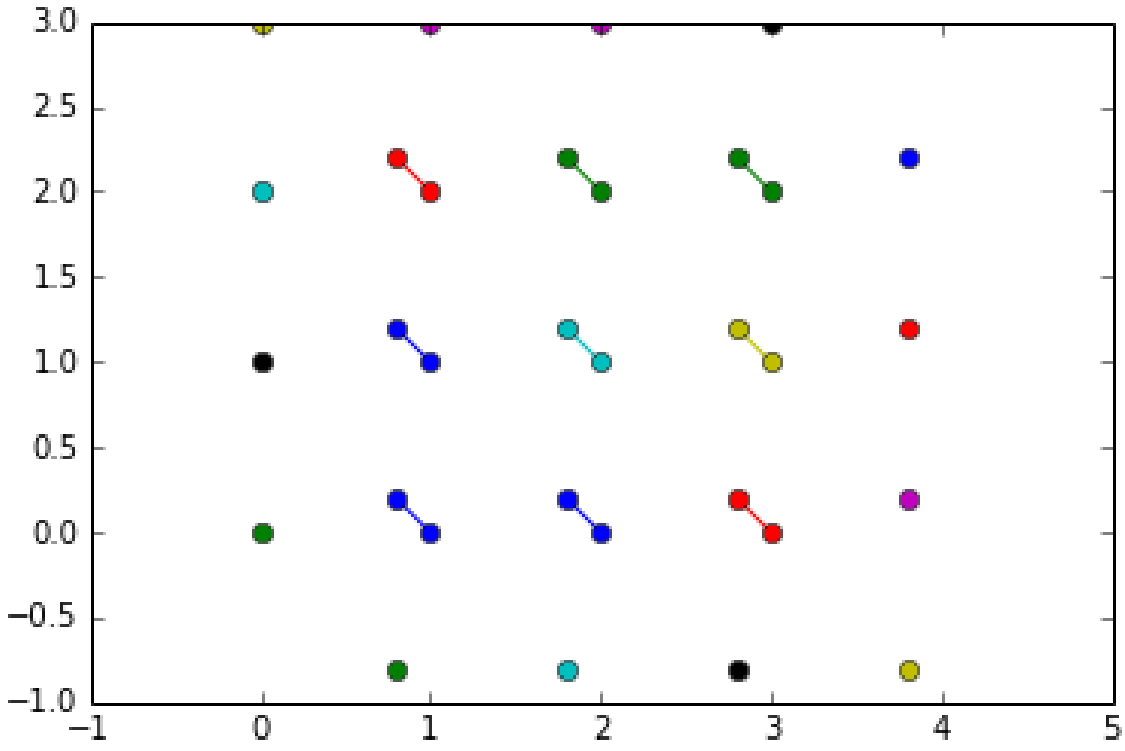

Figure 3.6: An ensemble of particles moving under constant velocity are identified through time using a simple Brownian prediction, Eq. (3.4). Features that have been identified as belonging to the same trajectory are connected by a line and colored alike. In this case, the identification is not correct.

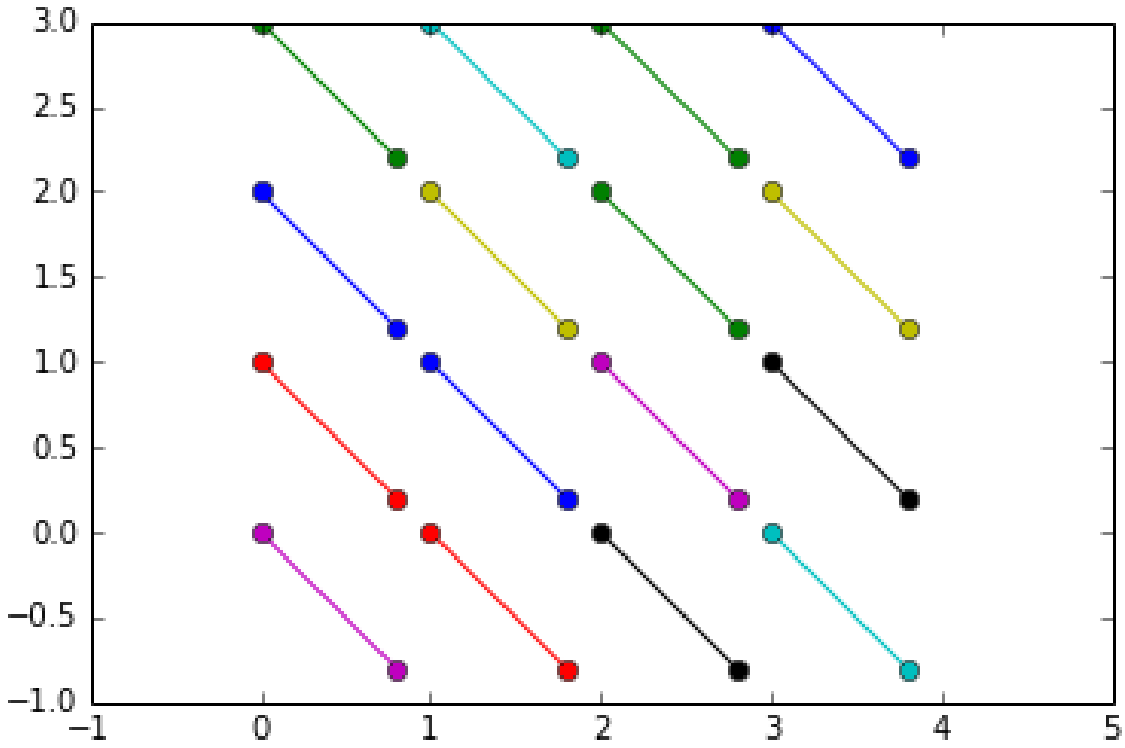

Figure 3.7: An ensemble of particles moving under constant velocity are identified through time using a constant-velocity predictor, Eq. (3.5). As before, features that have been identified as belonging to the same trajectory are connected by a line and colored alike.

The result is accurate (Figure 3.7). To be clear, the predictor does not need to specify exactly where the particle will be; it only must bias the search enough that the correct identification will be made.

3.5.2 Dynamic predictors

In typical experimental conditions, the particles' velocities are not known ahead of time. It would be much better for the predictor to "learn" about the velocities, and allow different particles to have different velocities that can change over time. To

accomplish this, P will depend on more than x_0, t_0, and t_1; it will also depend on the particles' most recent velocities.

$$P(t_1, t_0, \vec{x}(t_0)) = \vec{x}(t_0) + \frac{\vec{x}(t_0) - \vec{x}(t_{-1})}{t_0 - t_{-1}}(t_1 - t_0) \tag{3.6}$$

There are a few caveats. If a new particle is in frame t_i but wasn't in t_{i-1}, its velocity is unknown, but it is estimated using the velocity of the nearest existing particle. Of course, in the first frame, all velocities are unknown because there is no previous frame. Fortunately, even though particles may be in motion from the start, an initial guess of $v_0 = 0$ often gives acceptable results. In many cases, at least some of the particles are moving slowly enough that they can be tracked and their velocity can be obtained. Then, because particles with unknown velocity borrow the nearest known velocity, this may give the algorithm a foothold to track more particles in later frames. If that is not sufficient, a more accurate initial guess can be specified. This guess can be a constant velocity, a velocity profile, or N-dimensional velocity field.

As a demonstration, consider a three-frame sequence that starts with small displacements and accelerates. With a simple Brownian predictor, tracking fails at the third frame (Figure 3.8). With the adaptive predictor, Eq. (3.6), tracking is accurate (Figure 3.9).

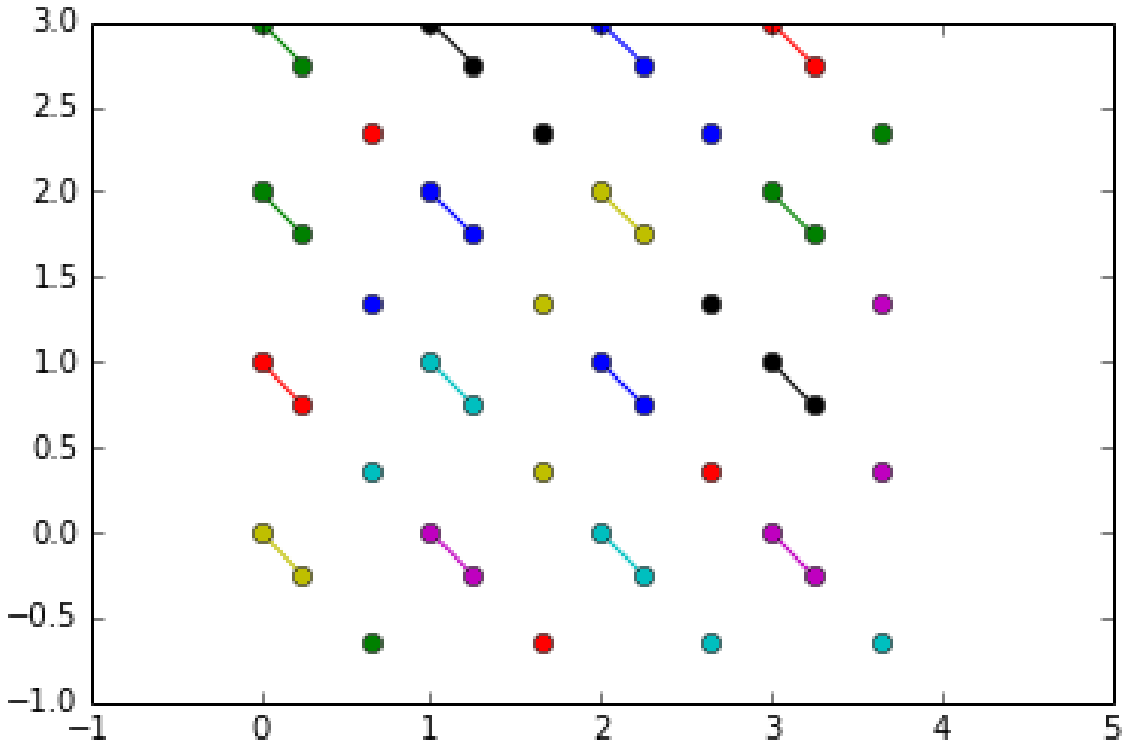

Figure 3.8: An ensemble of accelerating particles are identified through time using a simple Brownian prediction, Eq. (3.4). As before, features that have been identified as belonging to the same trajectory are connected by a line and colored alike. The identification is incorrect.

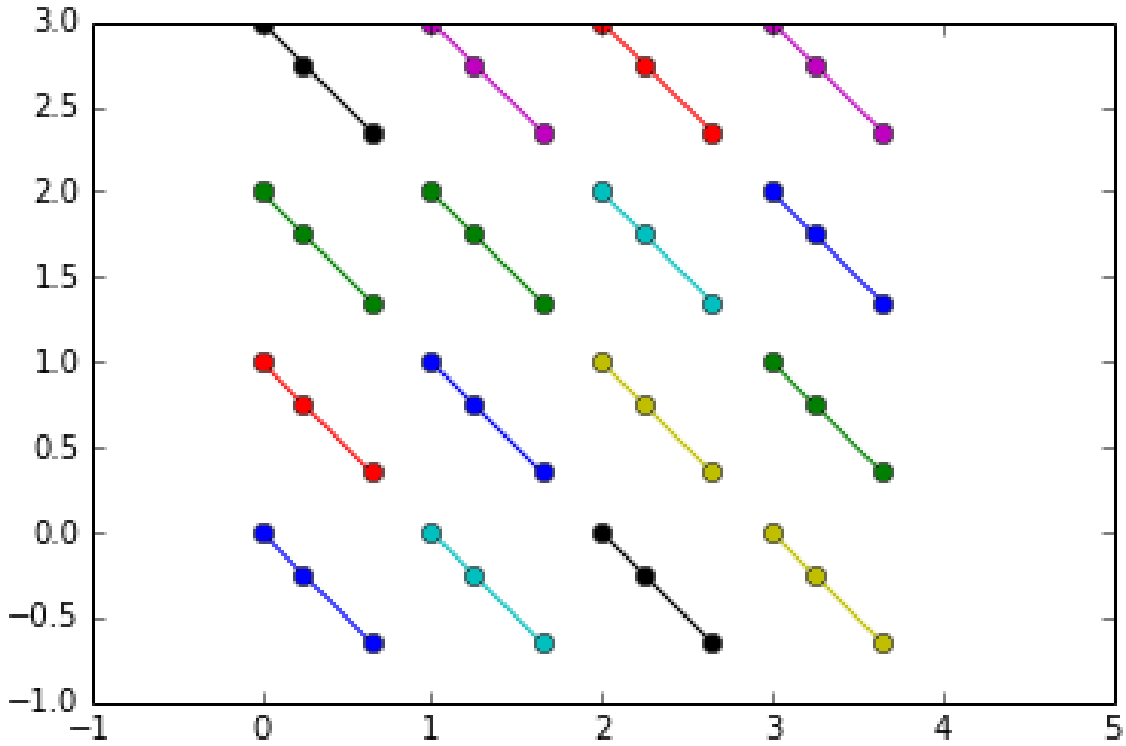

Figure 3.9: An ensemble of accelerating particles are identified through time using an adaptive prediction, Eq. (3.6). As before, features that have been identified as belonging to the same trajectory are connected by a line and colored alike.

3.5.2.1 Channel flow prediction

There are two special cases implemented by trackpy. The first is channel flow, in which velocities are relatively uniform in one direction. For example, if the channel is in the x (i.e. $\hat{i}$) direction, particle velocities are very well approximated as

$$\vec{v} = \hat{i} v_x(y) \tag{3.7}$$

where the velocity profile $v_x(y)$ is a smoothly-varying function defined across the channel. The required inputs are the direction of flow and size of the bins used to define the channel profile. The initial velocities can be specified or arrived at adaptively.

Figure 3.10 shows an example. The simple Brownian prediction fails for the top row of particles at the center of the channel. With a Channel Flow prediction, the tracking is accurate (Figure 3.11).

3.5.2.2 Drift prediction

The second special case implemented by trackpy is drift prediction. In interfacial microrheology measurements, it is common to observe convective flows driven by air currents or heat from the illuminating lamp. During data analysis, this motion can often be subtracted by adopting a reference frame set by the average velocity of the ensemble of particles. Likewise, tracking accuracy and performance is improved by

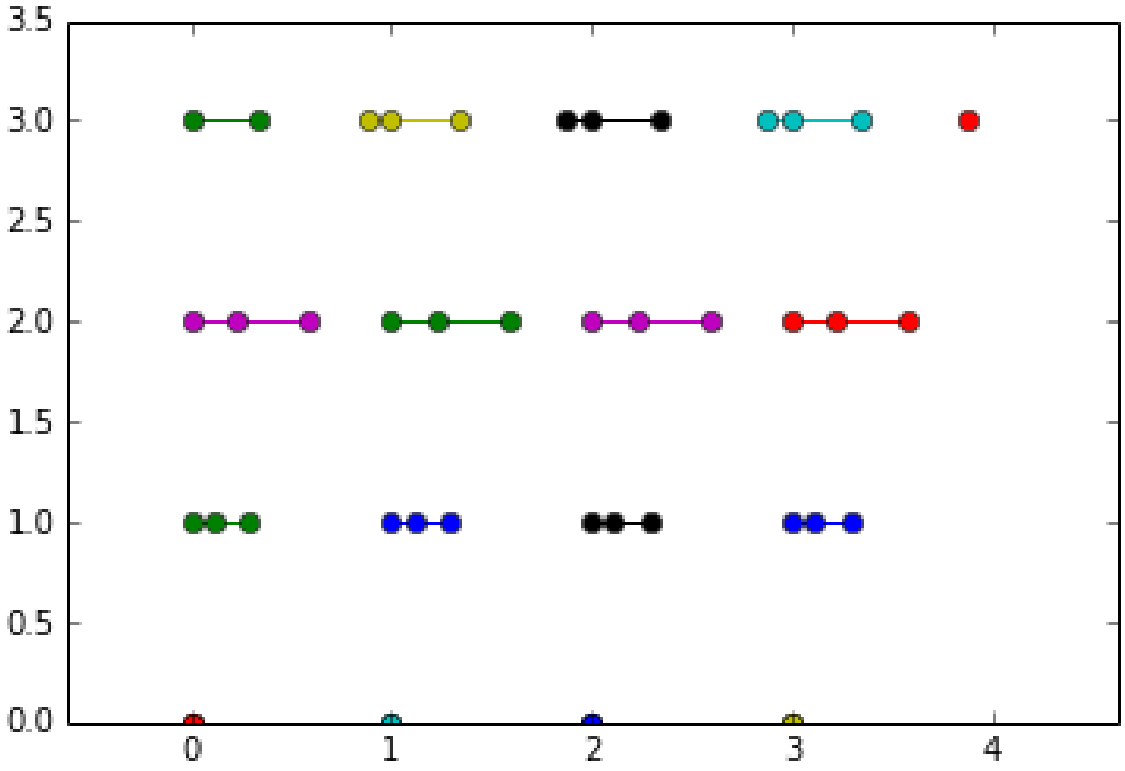

Figure 3.10: An ensemble of particle moving in simulated channel flow are identified through time using a simple Brownian prediction, Eq. (3.4). As before, features that have been identified as belonging to the same trajectory are connected by a line and colored alike. The identification is incorrect.

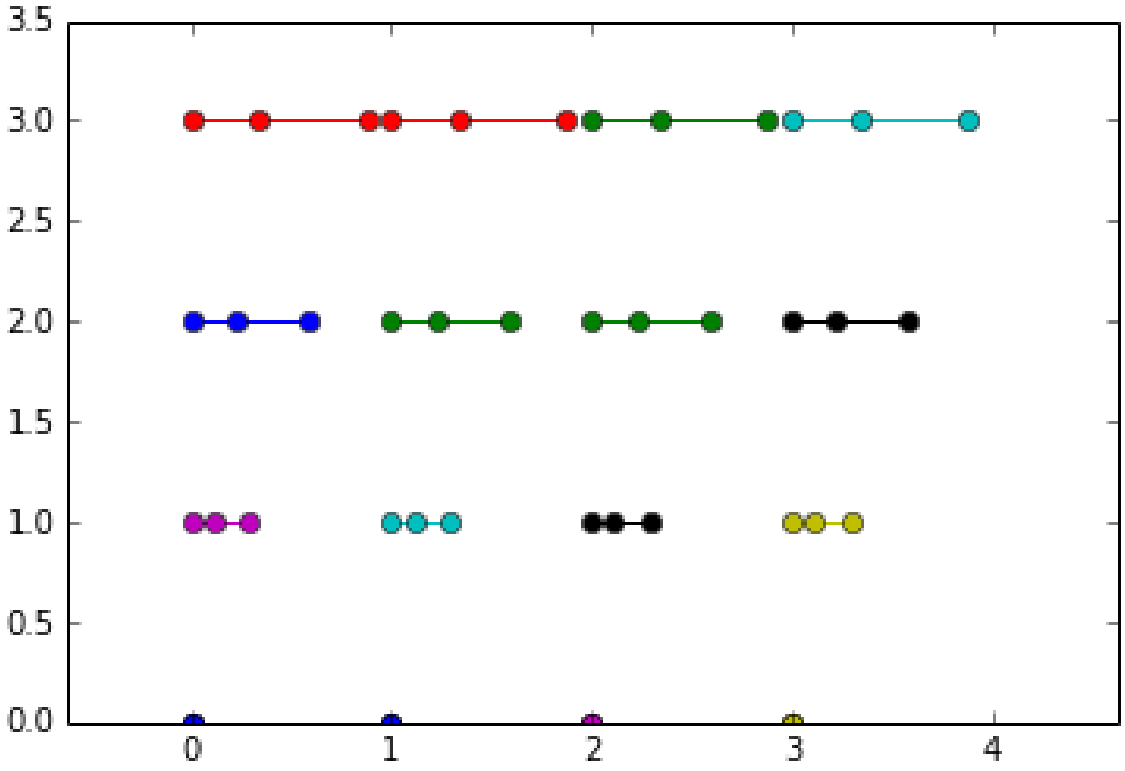

Figure 3.11: An ensemble of particle moving in simulated channel flow are identified through time using a Channel Flow predictor. As before, features that have been identified as belonging to the same trajectory are connected by a line and colored alike.

forming a prediction based on the average velocity of the ensemble.

3.6 Testing & Reproducibility

Trackpy is packaged with more than 180 automated tests: snippets of code that exercise a specific capability of trackpy by running toy examples and comparing the output to known correct results. For example, to test feature location, an automated test draws a simple image with several dots and checks that trackpy can locate the dots with a given precision.

Testing benefits a research code in more than one way. Most obviously, tests verify correctness and check special cases. Just as important, tests protect reproducibility. By codifying key results as tests, authors can be sure that these results cannot be broken inadvertently in the future. This empowers users who do not have familiarity with the whole codebase to make contributions and changes with confidence that they will not have unintended consequences. When revisions are submitted to trackpy, a web service automatically executes all the tests, and it alerts the user if any tests fail under the proposed change. Finally, the test suite complements the documentation. Technical users and potential contributors can browse it as a comprehensive demonstration of the ways in which the authors imagined the code would be used.

Trackpy has an unusual level of testing for a code from an academic lab. But the time invested has been worthwhile: it ensures that any research that depends

on the code is grounded in a rigorous, scientific approach to software development. This guarantee earns the confidence of other researchers who decide to use, cite, or contribute to the codebase. It thereby increases the code's longevity and the impact of the development effort.

As trackpy is improved and changed, old research code may cease to reproduce exactly the same results. Testing help ensure that any such "breaking changes" are made deliberately and can be documented. To avoid breaking old code altogether, researchers can make note of which specific version of trackpy was used for a given project and roll back to that version when revisiting the research. Several new projects such as Docker, Dexy, and hashdist address this need: they recreate complete computing environments, making it possible reproduce research using the specific original versions of all the relevant software. These tools are especially powerful in simulation research, where the entire research project can reproduced on a computer. But, they are also useful in experimental science, covering every step after data collection up to the production of the published figure.

3.7 Conclusion

3.7.1 "A Modern Approach"

Trackpy is distinguished among niche academic codes by its careful adherence to the best practices of the open source software community.[98] The most important are

code review and open discussion before each revision, automated testing, complete API documentation. Also, code comprehensibility and modularity are key design considerations. Code that merely works is not necessarily easy to test, maintain, extend, or reuse.

Code for academic use is typically developed for a single research project, often by a single researcher, at least at first. Trackpy has benefitted from its co-development by three different researchers working in separate groups at separate institutions on projects with vastly different priorities. The core functionality of trackpy was useful to all, and the healthy tension in the project drove the development of extensible, reusable code. In addition to the core developers, collaborators and other researchers used trackpy actively during its development. Their use of the cutting-edge code demanded stability and thorough documentation. As the project matured, a wider community of users discovered it and found it useful.

3.7.2 Measuring Success

The scientific software community has not settled on a single metric for the success of academic software. In the three years since the first lines of code were written, trackpy has supported published research from several academic research groups; trackpy has been downloaded thousands of times through the Python Package Index, though it is impossible to know if the recipients were genuine users; trackpy has been adopted by users from about ten top academic research institutions known to the

authors. Most importantly, trackpy has benefitted from code contributions offered by those users, comprising both software experts and relative novices. Particle tracking is a general problem in a number of fields, and thanks to the pioneering efforts of John Crocker, David Grier, and Eric Weeks, it has a strong tradition of open source code supporting first-rate research.

3.7.3 Future Directions

Trackpy can increase its impact and extend its applicability by incorporating algorithms and strategies from outside the colloids literature and the software lineage of Crocker and Grier. Researchers in the biological and biophysics communities also use these tools, but they have developed additional methods to solve more complicated image analysis problems. For example, in biological contexts, features must be located amidst a complex, busy environment where they are more difficult to distinguish and the methods discussed above can be insufficient to extract them. Tracking and the notion of a trajectory can be subtler, as features might split or merge with each other.

Separately, the scientific Python community continues to grow and develop ever more powerful tools for exploring, processing, and presenting data. Trackpy will build on this ongoing progress, providing tools specific to the needs of particle tracking.

Chapter 4

Linear and Nonlinear Microrheology of Lysozyme Layers Forming at the Air–Water Interface

4.1 Introduction

When an aqueous protein solution forms an interface with air or an oil, the protein molecules can discover the interface through diffusion and adsorb.[99] The adsorption process is commonly believed to include conformational changes to the protein that lift hydrophobic substructures out of the aqueous surroundings. As the interface ages,

it becomes increasingly crowded with adsorbed protein, and its rheology changes dramatically.[31] The mechanical properties of interfacial protein layers are an important aspect of their biological function, as in films that form on lachrymal secretions[100] and saliva,[28] and in their role in biomedical and food processing technologies.[101] In particular, the mechanical behavior of interfacial protein layers can enhance the stability of droplets and bubbles in emulsions and foams.[25,26] Protein layers are fragile, molecularly thin, and spatially heterogeneous films whose properties evolve with time. These features complicate traditional interfacial rheometry measurements and often make results difficult to interpret. Recently, microrheology techniques have shown promise as an alternative method to characterize the evolving mechanical behavior of protein layers.

As discussed in Chapter 2, the basic approach of microrheology, which is most often employed to study bulk materials, involves tracking the motion of colloids embedded in the material to probe its mechanical properties. Passive microrheology connects Brownian fluctuations of colloids to a material's linear shear response. Active microrheology infers the drag on colloids driven by an external forcing and relates that drag to mechanical response through a linear or nonlinear model relating stress and strain. Applying microrheology to an interfacial system like a protein layer presents particular challenges. The theory supporting microrheology assumes Stokes drag, which is subtle in two dimensions.[19] Moreover, colloidal probes at an interface experience drag forces from both the interfacial layer and from the underlying sub-

phase. Since no exact closed-form solution for the drag on a membrane-bound object exists, one must rely on the analytical and numerical approximations described in Section 1.2.2.

Nevertheless, despite these challenges, microrheology has found increasing application in the study of films at fluid-fluid interfaces including not only protein layers[11,12,102–104] but also polymer layers,[23,105,106] lipid monolayers,[107–111] and particle-laden interfaces.[112,113] This work has included studies of both the linear shear rheology and nonlinear mechanical response of interfacial films. Recently, the interfacial microrheology of layers of the protein β-lactoglobulin at air-water and oil-water interfaces was investigated in a study that illustrated the promise of the technique.[12,102] These experiments included both active and passive microrheology measurements that tracked the transition from viscous to elastic mechanical behavior as the layers form. In both β-lactoglobulin adsorbing to the air-water and to an oil-water interface, the microrheology revealed a viscoelastic transition consistent with gel formation. However, features of the transition, such as the rate of layer formation and degree of spatial heterogeneity, varied strongly between the two cases.[12,102]

Although the viscoelastic transition in protein layers is often ascribed to network formation through intermolecular association,[30–33,101,114] and indeed the evidence from microrheology for gelation in β-lactoglobulin layers supports this scenario, other mechanisms for the onset of elasticity in protein layers, particularly involving glass transitions, have been proposed.[37–40] Therefore, in an effort to understand

better those aspects of the viscoelastic transition in protein layers that are universal and those that are system specific, we have conducted a microrheology study of layer formation at the air interface of lysozyme solutions. As described in Section 4.2 below, layers formed by lysozyme at the air-water interface are good candidates for microrheology investigations. Our study included passive measurements, which tracked the Brownian motion of spherical colloids at the interface, and active measurements in which the rotational motion of magnetic nanowires at the interface was employed to infer layer rheology. The experimental methods are described in Section 4.3. As described in Section 4.4, the passive measurements provide information about the linear frequency-dependent shear modulus of the layers, while the active measurements probe properties of the layer's nonlinear stress response. Together the measurements track the interfacial rheology as it evolves through a viscoelastic transition with increasing layer age. We discuss in Section 4.5 two possible frameworks for understanding this mechanical evolution: gelation and the formation of a soft glass phase. Finally, Section 4.6 offers some conclusions from the study.

4.2 Background

Lysozyme is a single-chain globular protein comprised of 129 amino acids with molecular dimensions $3.0 \times 3.0 \times 4.5$ nm^3 and molecular weight 14,300 g/mol. The molecule is considered a "hard" protein that is rigid against conformational fluctua-

tions, due in part to the presence of four internal disulphide bridges. Correspondingly, lysozyme is stable against denaturation over an unusually large range of bulk solution conditions. However, it readily adsorbs at the air-water interface, and interfacial rheometry measurements on mature interfacial layers reveal that they can acquire pronounced elasticity.[33,115] The structural properties of adsorbed lysozyme layers have been studied in detail by neutron and x-ray reflectivity.[116–118] In addition, surface-sensitive spectroscopies have interrogated the conformational state of the absorbed molecules.[119,120] Interpretation of the reflectivity measurements has led to debate about the structure of adsorbed lysozyme. While neutron reflectivity results indicate that the lysozyme retains its globular structure with no significant denaturation, time-resolved x-ray reflectivity results indicate that the molecules initially adsorb in a flat, unfolded structure. Evidence for conformational changes is further provided by Fourier transform infrared spectroscopy, which indicates adsorbed lysozyme contains antiparallel β-sheets that are absent in the native structure.[120] However, no direct evidence exists for the breaking of the internal disulphide bridges upon adsorption. In absorbed layers of other protein species, such as β-lactoglobulin, the formation of intermolecular disulphide bridges is seen as an important feature of layer formation. By characterizing the viscoelastic transition in interfacial lysozyme layers, we seek to correlate properties of the viscoelastic behavior with possible structural models to provide further insight into the layer formation.

As described in the next section, we focus our study on lysozyme solutions with

a fixed bulk concentration of 0.05 mg/ml, for which the reflectivity indicates dense monolayers form at the interface.[116,117] Specifically, this concentration is near the upper limit at which the thickness of mature layers, approximately 3.0 nm, is the same as more dilute layers. At somewhat higher concentrations, the layer thickness increases, indicating a reorientation of the molecules at the interface, presumably due to crowding. At far higher concentrations, lysozyme can form multi-layers at the air-water interface. However, those concentrations are two orders of magnitude greater than in the present study.[116] Hence, in this study we consider monolayers of protein.

4.3 Experimental Methods

4.3.1 Sample Preparation

Lyophilized powder of chicken-egg lysozyme (Sigma Aldrich, purity of 98%) was mixed gently[121] into 10 mM sodium phosphate buffer, pH 7.4, at room temperature to obtain solutions with 0.05 mg/ml protein. The solutions were employed within minutes of preparation. For the measurements, samples were contained in a 1-cm inner-diameter cylinder with an inner surface whose bottom half was aluminum and top half was Teflon, so that when solution filled the cell to the appropriate level, the aluminum–Teflon seam pinned the air–water interface, creating a flat surface with no meniscus. To begin, we filled the cylinder nearly to the seam with 0.5 ml of the protein solution. The age of the sample t_a was measured from the moment the cell

was filled with solution, creating a fresh interface with the air. A spreading solution containing either spherical or nanowire colloids (discussed below) was prepared in advance and sonicated to disperse any colloidal aggregates. In addition to the colloids, the spreading solution contained equal parts buffer solution and isopropanol (IPA). To introduce the colloids to the interface, we touched a 10-μL droplet of the spreading solution to the surface. The solution wet the interface, depositing colloids uniformly over the surface. Evaporation of the IPA typically caused convective flows at the interface that persisted for about one minute. All measurements were performed only after these flows ceased. After each experiment, the sample cell was cleaned thoroughly by scrubbing and sonicating in Alconox soap solution, acetone, and IPA, and then rinsed repeatedly in deionized water.

We note the presence of the IPA in the spreading solution could potentially influence layer formation at the interface. Measurements of the sample mass over time indicated that some of the IPA evaporated within seconds while the rest mixed into the bulk, where if uniformly distributed it constituted at most 1% of the solution. While lysozyme is stable in such dilute IPA solutions at room temperature, the near-surface IPA concentration was likely larger at times shortly after application of the spreading solution, and the protein can denature at IPA concentrations above 20%.[122] Further, even at concentrations below which the alcohol does not denature the lysozyme, its interactions with the protein could affect the protein's hydrophilicity, which would impact its adsorption properties. To understand the possible effects of the IPA, we

performed additional experiments using pure buffer as the spreading solution and found that the IPA did not significantly affect the interface's subsequent rheological properties. Because we achieved better surface coverage of colloids by including IPA in the spreading solution, all results discussed here were obtained with this sample preparation.

4.3.2 Passive (Brownian) Microrheology

For the passive microrheology measurements, we employed charge-stabilized polystyrene spheres (Interfacial Dynamics Corp.) with radius 0.5 μm. We observed the colloids at the interface using an inverted bright-field microscope with a 40X objective (WD 2.7-3.7 mm, NA 0.6). A video camera (Nikon D3100) recorded a 300×170-μm field of view at a rate of 30 frames per second, which set the shortest time over which probe motion could be characterized. (The exposure time was approximately 0.033 s, the inverse of the frame rate.) Video was captured continuously, so that, in principle, probe trajectories could be followed for arbitrarily long durations. However, for analysis, the videos were divided into segments whose duration was restricted by the evolving dynamics at the interface during layer formation.

We extracted probe trajectories from the video using a custom Python implementation[89] of the widely-used Crocker–Grier multiple-particle-tracking algorithm.[74] We accounted for static and dynamic errors in the particle tracking, which can qualitatively distort microrheology measurements if left uncorrected.[72] Typically between

30 and 200 probes were in view at any time, constituting up to 0.3% surface coverage. As the experiment proceeded, some probes encountered each other and aggregated, reducing the population of usable probes. Also, we corrected for drift of the probes at the interface, which was more severe than in a typical bulk microrheology measurement, by subtracting the average velocity of the ensemble from that of each particle.

In general, particle mobility in an interfacial film is affected by drag from both the film and from the adjacent bulk fluid phases. The bulk contribution is most important when the interfacial viscosity is small, and theories have been developed to separate the contributions.[5,22,107,123–125] When the interfacial viscosity is large or the layer is viscoelastic, the subphase contribution is less important, and, as described below, the measurements on lysozyme layers were in this regime. In this case, under appropriate conditions, one can obtain the frequency-dependent interfacial shear modulus $G^*(\omega)$ from the Brownian motion of the probes through a two-dimensional version of a generalized Stokes-Einstein relation,[23,105]

$$G^*(\omega) = \frac{k_B T}{\pi i \omega \mathcal{F}_u\{\langle \Delta r^2(t) \rangle\}} \tag{4.1}$$

where $\langle \Delta r^2(t) \rangle$ is the particles' ensemble-average mean-squared displacement and $\mathcal{F}_u\{\langle \Delta r^2(t) \rangle\}$ is its unilateral Fourier transform.

4.3.3 Active Microrheology

4.3.3.1 Magnetic Nanowire Probes.

For the active microrheology measurements, we employed ferromagnetic nickel wires, whose fabrication has been described elsewhere.[126] The wires, which had radius $R_w = 0.175$ μm and lengths L from 5 to 30 μm, possessed a large magnetic moment ($\mu/\mathrm{L} = 3 \times 10^{-14} \mathrm{A \cdot m^2}/\mu\mathrm{m}$) parallel to their axis. The wires were hydrophobically functionalized with n-octadecyltrimethoxysilane (OTMS) and spread onto the interface as described above. The functionalized wires make a contact angle at the air–protein solution interface of $\theta_c = 79^\circ \pm 1^\circ$, as determined previously,[12] implying the wires were approximately half-submerged.

4.3.3.2 Microscopy with *in situ* Magnetic Fields.

Custom-built "magnetic tweezers" mounted on an inverted microscope (Nikon TE2000), were employed to apply time-dependent magnetic torques to an isolated wire at the interface.[11] The tweezers, consisting of two sets of four solenoids with ferromagnetic cores positioned symmetrically above and below the microscope focal plane, could produce fields in any direction within the focal plane. A feedback mechanism in the electronics controlling the tweezers created rise times below 2 ms for a step change in the field. A high-speed camera (Photron Fastcam), recording a 70 μm $\times$ 70 μm view at frame rates up to 1000 fps, captured the wire's motion. The

wire's orientation in each video frame was determined by analyzing the gray-scale image and treating the brightness of each pixel as an effective mass to calculate the principal "inertial axis". With this procedure, we could resolve the orientation with an estimated precision of $\pm 0.1^\circ$, a tenfold improvement over our previous method.[12]

4.3.3.3 Measurement Procedures and Analysis.

Measurements of layer response to applied magnetic torques on wires were performed in the time domain using step changes in magnetic-field direction of 90°. Prior to the change in field direction, the field was oriented parallel to the wire, and hence to the wire's magnetic moment. Following the change in field direction, the wires experienced a magnetic torque,

$$\Gamma_{\mathrm{mag}} = \mu B \sin\theta \tag{4.2}$$

where θ is the angle between the wire axis and the field, causing the wires to rotate in the plane of the interface. Each measurement was repeated at several field values to test for linearity. In most cases, fields between 30 and 50 Gauss were selected since they caused the wires to rotate with angular velocities that were well matched to the video frame rate. At some later ages, when the layer imposed larger resistance to the wire rotation, field values up to 100 Gauss were employed. In the low-Reynolds-number conditions of the measurement, the magnetic torque was balanced by the

hydrodynamic drag and/or any elastic stresses from the interfacial layer and subphase. In the case of a simple viscous drag,

$$\mu B \sin\theta = \zeta_r \dot{\theta} \tag{4.3}$$

where ζ_r is the drag coefficient. The solution to Eq. (4.3) gives the resulting time dependence between the field and wire axis,[127]

$$\theta(t) = 2\tan^{-1}\left[\exp\left(-\frac{\mu B}{\zeta_r}(t - t_0)\right)\right] \tag{4.4}$$

where t_0 is an experimental parameter that accounts for uncertainty in the time that the wire begins rotating in response to the field change and can differ from zero by an amount up to the time between video frames. For such a viscous interface, the relative contributions to the rotational drag from the interface and subphase are parameterized by the Saffman length, $l_0 = \eta_s/\eta$, the ratio of the interfacial viscosity η_s to the subphase viscosity η. When the wire's length $L < l_0/10$, the interface dominates the drag, and one finds[5]

$$\zeta_r = 1.48 L^2 \eta_s \tag{4.5}$$

As described below, in the active microrheology measurements on lysozyme layers, we observed that in some cases the rotational motion of the wires was consistent with

simple viscous drag, Eq. (4.4). However, in other cases, particularly at large layer age, we observed deviations from Eq. (4.4) that we identify as a consequence of a nonlinear response by the layer to the stress imposed by the rotating wire. Specifically, we find in these cases that the layer's response is well described as that of a non-Newtonian, power-law fluid. A power-law fluid is characterized by the stress-strain relation

$$\sigma = K\dot{\gamma}^n \tag{4.6}$$

where σ is the stress, $\dot{\gamma}$ is the strain rate, K is known as the consistency, and the exponent n is known as the flow index. When $n = 1$, Eq. (4.6) reverts to the stress-strain relation of a viscous liquid, while $n < 1$ and $n > 1$ correspond to shear-thinning and shear-thickening behavior, respectively. More generally, power-law fluids are a special case of Herschel-Bulkley fluids, which are characterized by a power-law stress-strain relationship above a yield stress, σ_0,

$$\sigma = \sigma_0 + K\dot{\gamma}^n \tag{4.7}$$

Such non-Newtonian response is observed in a wide range of soft disordered materials including paints, plastics, polymeric solutions, and food products.[128]

Adopting a power-law fluid response like Eq. (4.6) to describe the wire motion

under the influence of a magnetic torque leads to

$$\mu B \sin\theta = (\zeta_{\mathrm{pl}}\dot{\theta})^n. \tag{4.8}$$

where the nonlinear drag coefficient ζ_{pl} has dimensions $(\mathrm{N}\cdot\mathrm{m})^{1/n}\cdot\mathrm{s}$. An analytical solution to Eq. (4.8) for $\theta(t)$ is not available; however, the inverse function $t(\theta)$ is:

$$t(\theta) = \left[\frac{\zeta_{\mathrm{pl}}}{(\mu B)^{1/n}}\frac{n}{1-n}\right]\times \sin^{1-1/n}\theta\ {}_2\mathrm{F}_1\left(\frac{1}{2},\frac{n-1}{2n},\frac{3n-1}{2n};\sin^2\theta\right)\Bigg|_{\pi/2}^{\theta} - t_0 \tag{4.9}$$

where ${}_2\mathrm{F}_1$ is the ordinary hypergeometric function and t_0 is the same small experimental parameter introduced in Eq. (4.4). As described below, we employ this form with $n < 1$ to analyze the wire rotation in the lysozyme layers. However, we emphasize that Eq. (4.8) should only approximate the torque relation in a power-law fluid. A more precise relation would need to account fully for the flow generated in the layer around the wire, and specifically for its spatially varying shear gradients, and would not lend itself to straightforward comparison with experimental results. Nevertheless, as shown below, Eqs. (4.8) and (4.9) accurately capture the rotational motion of wires in lysozyme layers, indicating a nonlinear response characteristic of a power-law fluid.

4.4 Results

4.4.1 Linear Rheology

The rheology at an air interface with the lysozyme solutions evolves quickly following the formation of the interface, with viscoelastic behavior emerging within minutes in the passive measurements, consistent with reflectivity studies that indicate lysozyme adsorbs rapidly at the air-water interface.[118] Figure 4.1 shows examples of the ensemble-averaged mean-squared displacement $\langle \Delta r^2(t) \rangle$ of the colloidal probes at several ages t_a since creation of the interface. For reference, the mean-squared displacement of colloids at the air interface of pure buffer containing no protein is also shown. In the absence of adsorbing protein, $\langle \Delta r^2(t) \rangle$ varies linearly with lag time indicating simple viscous drag with a viscosity consistent with water. At the interface of the protein solution, the mobility of the probes evolves rapidly at early layer ages; therefore, $\langle \Delta r^2(t) \rangle$ at each age is determined based on video segments of limited duration (less than one minute). For this reason, the maximum lag time t is restricted to $t \leq 1$ s to assure adequate statistics. Within the resulting limited dynamic range, $\langle \Delta r^2(t) \rangle$ is well described as a power law, $\langle \Delta r^2(t) \rangle \sim t^{\alpha}$. As shown in Fig. 4.2, the power-law exponent α steadily decreases with increasing age, signifying increasingly subdiffusive particle motion. Following analysis based on the generalized Stokes-Einstein relation, Eq. (4.1), power-law behavior in the mean-squared displacements of the colloidal probes, $\langle \Delta r^2(t) \rangle \sim t^{\alpha}$ with $\alpha < 1$, implies the lysozyme layer's

linear shear modulus, $G^*(\omega) = G'(\omega) + iG''(\omega)$, has power-law frequency dependence, $G'(\omega) \sim G''(\omega) \sim \omega^{\alpha}$.[15] The significance of this power-law frequency dependence and its evolution with layer age is discussed in Section 4.5 below.

4.4.2 Nonlinear Rheology

As in the passive microrheology, the active nanowire microrheology reveals a pronounced evolution in the mechanical behavior of the lysozyme layers with increasing layer age. Close inspection of the results in the active measurements and comparison with those from the passive measurements, however, show that they probe a different aspect of the layer response, specifically its nonlinear rheology. For example, Figs. 4.3(a) and 4.3(b) display the angle θ between an 11-μm-long wire and an applied magnetic field as a function of time following a 90° step change in the direction of the field at layer ages $t_{\mathrm{a}} = 2700$ s and 8200 s, respectively. At early ages, such as $t_{\mathrm{a}} = 2700$ s (Fig. 4.3(a)), the wire rotates rapidly in response to the magnetic torque so that the angle between the wire axis and the magnetic field relaxes fully to zero in a short time, and the response at these ages is consistent with the wire experiencing simple viscous drag. The dashed line through the data in Fig. 4.3(a) shows the result of a fit using the form for viscous drag, Eq. (4.4), which agrees closely with the data. Such agreement is observed at all layer ages up to $t_a \approx 3000$ seconds. The interfacial viscosity extracted from the fit using Eq. (4.5) is 21 nPa·m·s, which implies $L\eta/\eta_s \approx 2$, near the lower limit of interfacial viscosity where Eq. (4.5) is a valid approximation

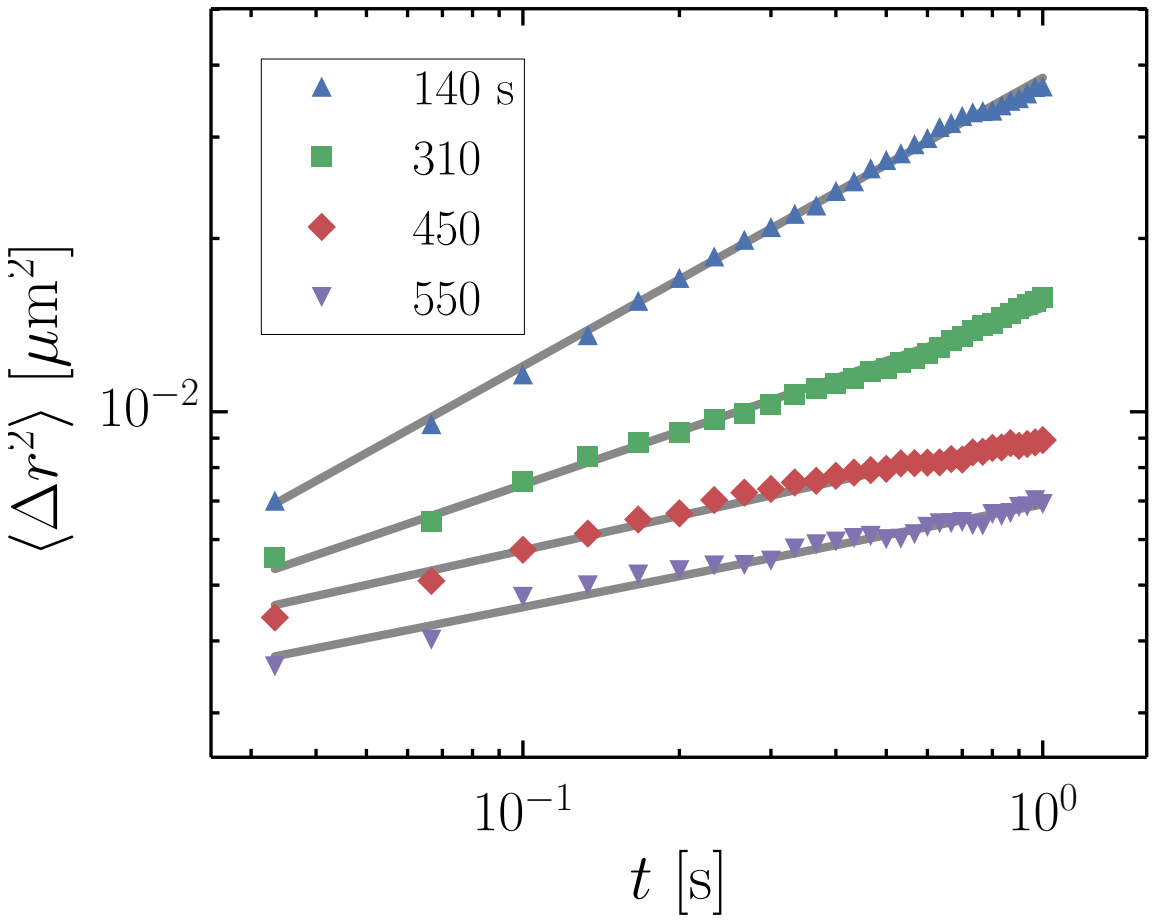

Figure 4.1: Ensemble-average mean-squared displacements of 0.5-μm radius colloids at the air interface of a lysozyme solution (0.05 mg/ml, pH 7.4) at ages $t_a = 140$ (squares), 310 (diamonds), 450 (triangles), and 550 (solid circles) seconds since formation of the interface. Also shown is the mean-squared displacement of the probes at the air-buffer interface in the absence of protein. The solid lines are the results of power-law fits.

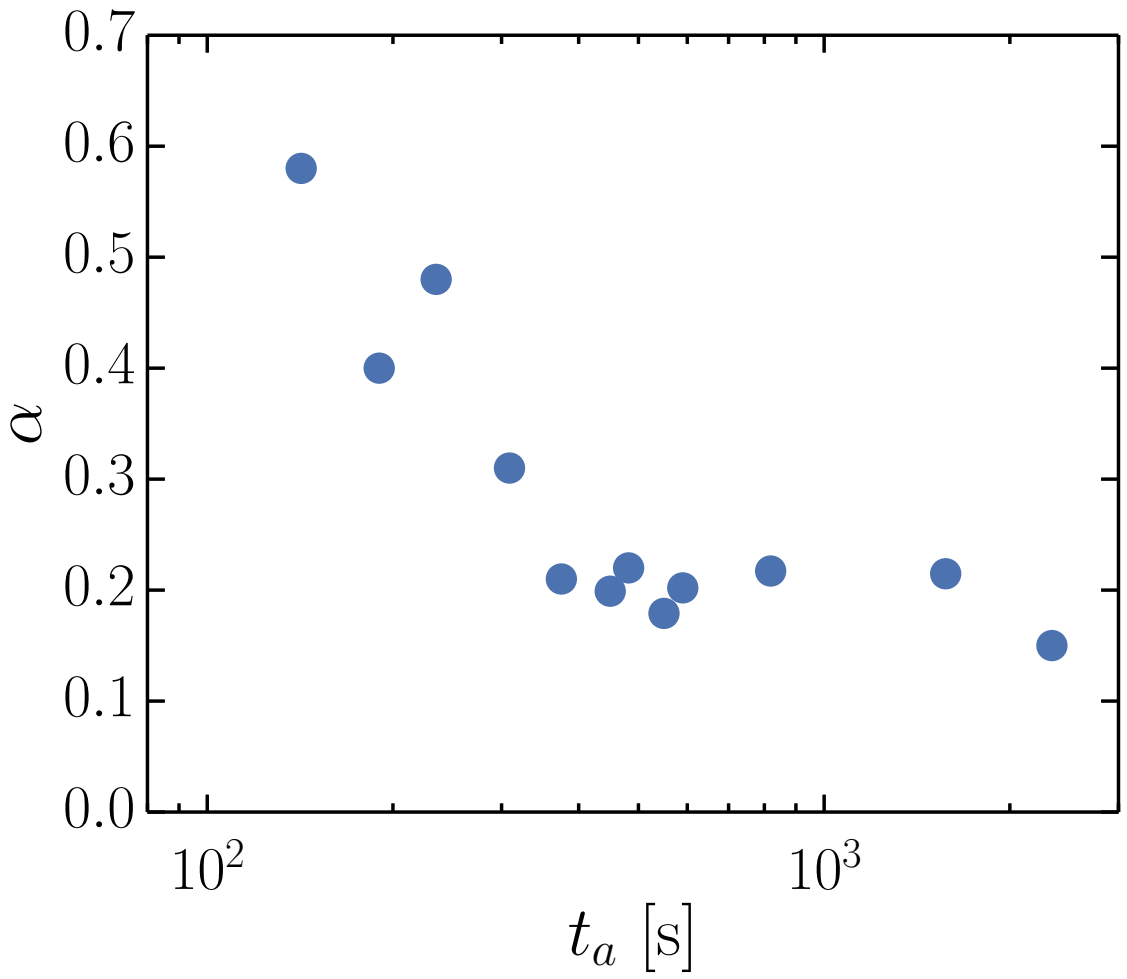

Figure 4.2: Power-law exponent characterizing the ensemble average mean-squared displacements, $\langle \Delta r^2(t) \rangle \propto t^\alpha$, of colloids at the air interface of a lysozyme solution as a function of the age since formation of the interface.

for the drag coefficient.

Notably, this value of interfacial viscosity, 21 nPa·m·s, is the same order as that measured previously on β-lactoglobulin layers at early ages.[12] However, as described in Section 4.4.1 above, during this span of early ages where the active measurements appear consistent with a viscous layer, the passive measurements show increasingly viscoelastic behavior. This apparent discrepancy results from the active measurements accessing a nonlinear rheological response from the layers. Hence, one should not interpret this result as the linear, zero-shear-rate viscosity of the lysozyme layers. The nonlinear nature of the response is shown clearly in analysis of the nanowire rotation at later ages when the shape of $\theta(t)$ becomes no longer consistent with simple viscous drag. This change is illustrated by the dashed line in Fig. 4.3(b), which shows the result of a fit using Eq. (4.4) to the data at $t_a = 8200$ s and which reveals pronounced deviations of $\theta(t)$ from the viscous lineshape. Such systematic deviations are apparent in the angular response of the wire at all ages greater than 3000 s. The solid line through the data in Fig. 4.3(b) depicts the result of a fit using the power-law-fluid form, Eq. (4.9), to the data with $n \approx 0.6$. As the fit illustrates, good agreement between the data and Eq. (4.9) is found for all ages. That is, for $t_\mathrm{a} < 3000$ s, best fits with Eq. (4.9) give $n \approx 1$ and are indistinguishable from fits with Eq. (4.4), while at later ages $n < 1$, implying shear-thinning behavior. We note that for shear-thinning power-law fluids, the apparent zero-shear-rate viscosity $\eta_{app} \equiv \sigma/\dot{\gamma} \sim \sigma^{1-1/n}$ diverges in the limit of small shear stress, consistent with the nearly elastic response observed

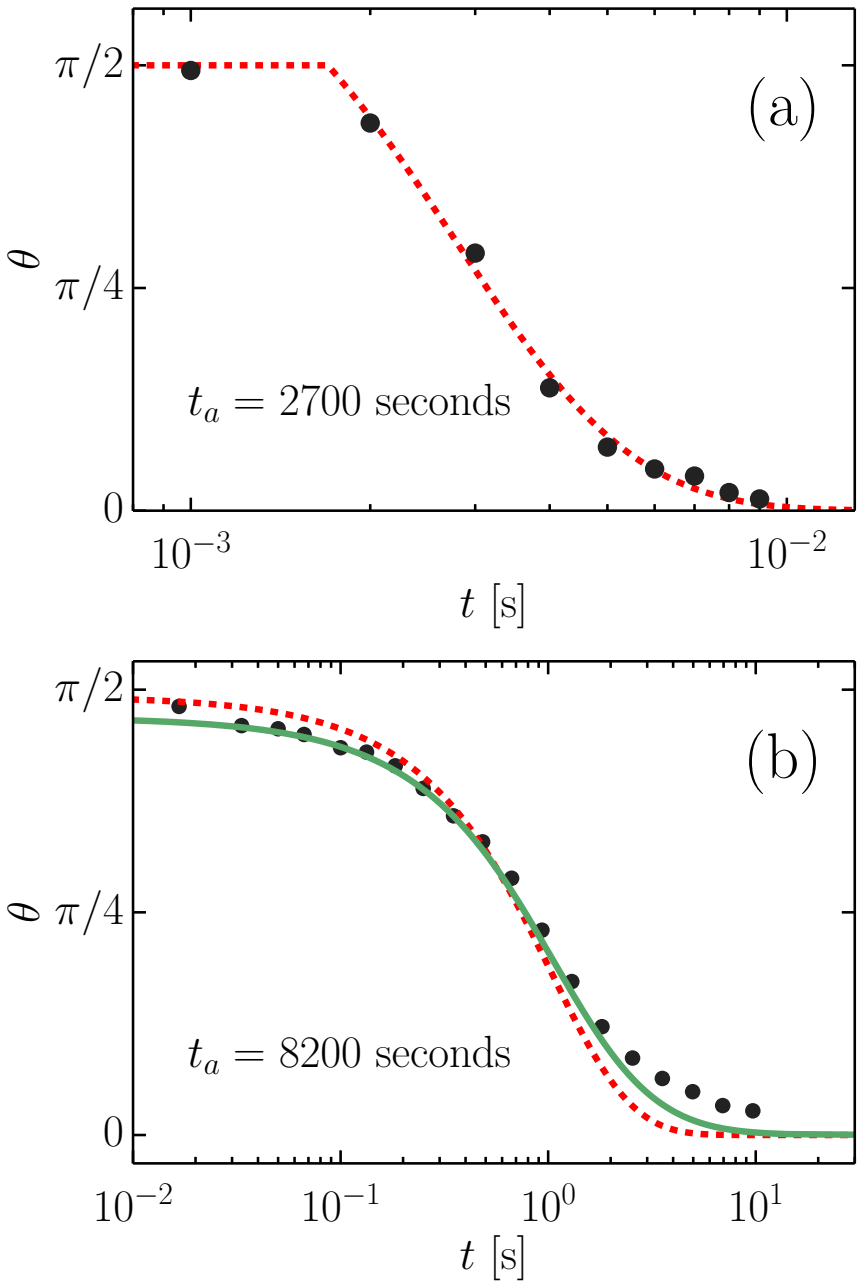

Figure 4.3: Angle between the axis of a 11-μm-long Ni nanowire and external magnetic field as a function of time following a step change in the field direction of 90° at interface ages (a) t_a = 2700 s (B = 30 G) and (b) t_a = 8200 s (B = 60 G). The dashed lines in (a) and (b) are the results of fits to the data using a form based on simple viscous drag (Eq. (4.4)), and the solid line in (b) is the result of a fit using a form based on drag from a power-law fluid (Eq. (4.9)).

in the passive microrheology at ages greater than 3000 s.

While Eq. (4.9) describes accurately the angular rotation of the wire through the protein layer, the nonlinear nature of the hypergeometric function makes obtaining stable values for n and ζ_{pl} through fits using Eq. (4.9) problematic. However, an alternative approach to modeling the power-law-fluid response is obtained by rearranging the torque balance relation, Eq. (4.8), to get

$$\ln(\dot{\theta}) = \frac{1}{n}\ln(\sin\theta) + \ln\left(\frac{(\mu B)^{1/n}}{\zeta_{\mathrm{pl}}}\right) \tag{4.10}$$

Thus, the power-law-fluid model predicts that the logarithm of the time derivative of $\theta(t)$ varies linearly with the logarithm of $\sin(\theta)$ and that the inverse of the flow index $1/n$ is the proportionality constant. As a test of this prediction, Fig. 4.4 shows results for the wire rotation at a series of layer ages plotted in this way, where the values of $\ln(\dot{\theta})$ are obtained from $\theta(t)$ through the Savitzky-Golay smoothing algorithm.[129] As the figure indicates, the data follow a linear relationship as expected from Eq. (4.10). Further, we find that linear fits with Eq. (4.10) provide a more reliable method of obtaining n than do direct fits to $\theta(t)$ using Eq. (4.9). For instance, the change from $n \approx 1$ at early ages to shear-thinning behavior at late ages is seen clearly in the change in slope of the data in Fig. 4.4. Figure 4.5 displays the values of n extracted from fits using Eq. (4.10) as a function of layer age. The flow index appears to undergo an abrupt decrease around $t_{\mathrm{a}} = 3000$ s from $n \approx 1$ to $n \approx 0.7$.

(The data could also be interpreted as a steady decrease in n, but one should not expect that n extrapolates at early times to values greater than one, which would imply shear-thickening behavior.) The values of n obtained for the lysozyme layers at late ages are typical of shear-thinning materials that behave as power-law fluids, where in most cases $0.3 < n < 1$ is observed.[130,131]

While the success of Eqs. (4.9) and (4.10) provides strong evidence that the layer response in the active microrheology experiments reflects the nonlinear rheology, this nonlinear behavior is more directly demonstrated in the dependence of the wire rotation rate on the magnetic-field strength B. Since the torque on the wire is proportional to B, a viscous-like linear response from the layer should lead to a rotation rate that is similarly proportional to B. Figure 4.6(a) shows results for the rotation angle from a set of measurements at $t_a = 8200$ s at various field strengths with time scaled by B. In contrast to the expectations of linear response, the curves at different B fail to collapse. Better scaling is achieved assuming the nonlinear relation between rotation rate and B implied by the power-law-fluid form of Eq. (4.8), as shown in Fig. 4.6(b).

A common property of the rheology of shear-thinning, thixotropic materials is a recovery period following application of a nonlinear stress during which the shear-altered structure relaxes back to its quiescent state. We searched for such effects in the active microrheology on the lysozyme layers by varying the waiting time between wire rotations and by varying the sequence of magnetic field values. We found no discernible transient behavior for waiting times as small as 2 seconds, the minimum

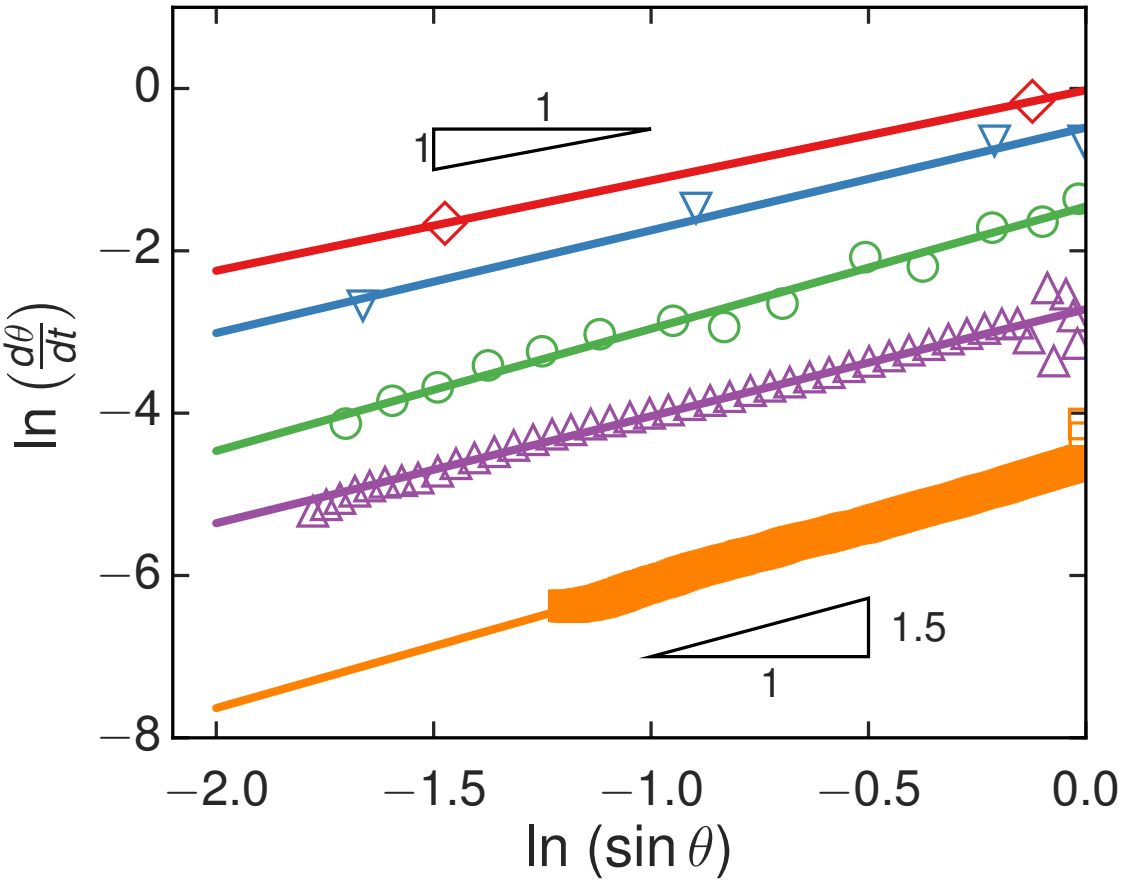

Figure 4.4: Logarithm of the nanowire rotation rate as a function of the logarithm of $\sin(\theta)$, where θ is the angle between the wire axis and external magnetic field, at interface ages $t_a = 1320$ seconds (red circles), 2700 seconds (blue triangles), 3600 seconds (green squares), 5100 seconds (purple diamonds), and 6600 seconds (orange inverted triangles). The solid lines are the results of linear fits. The slope increases with layer age from near one at early ages to above 1.5 at late ages.

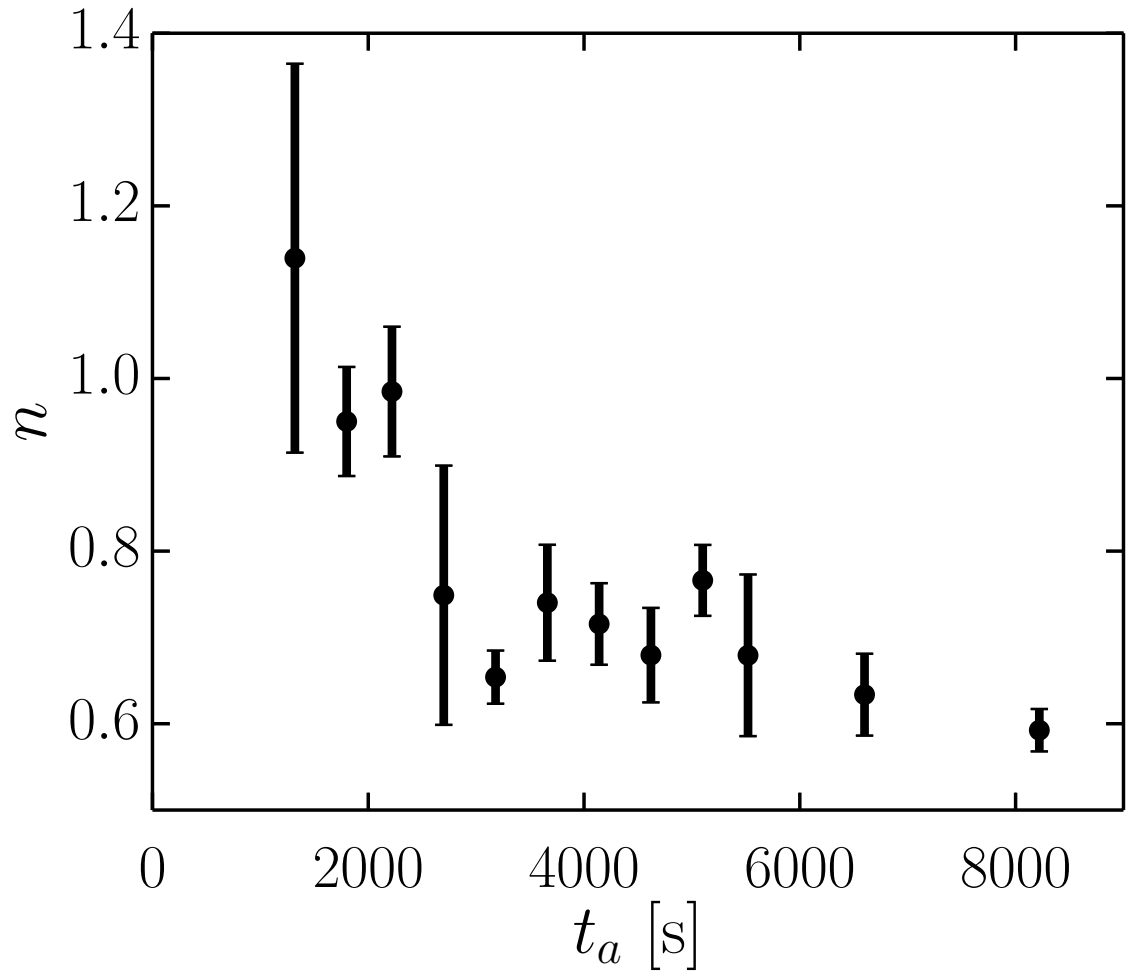

Figure 4.5: Flow index n as a function of layer age. At each age, n is determined from measurements at several magnetic-field values. The error bars incorporate both statistical variation in n and measurement uncertainty.

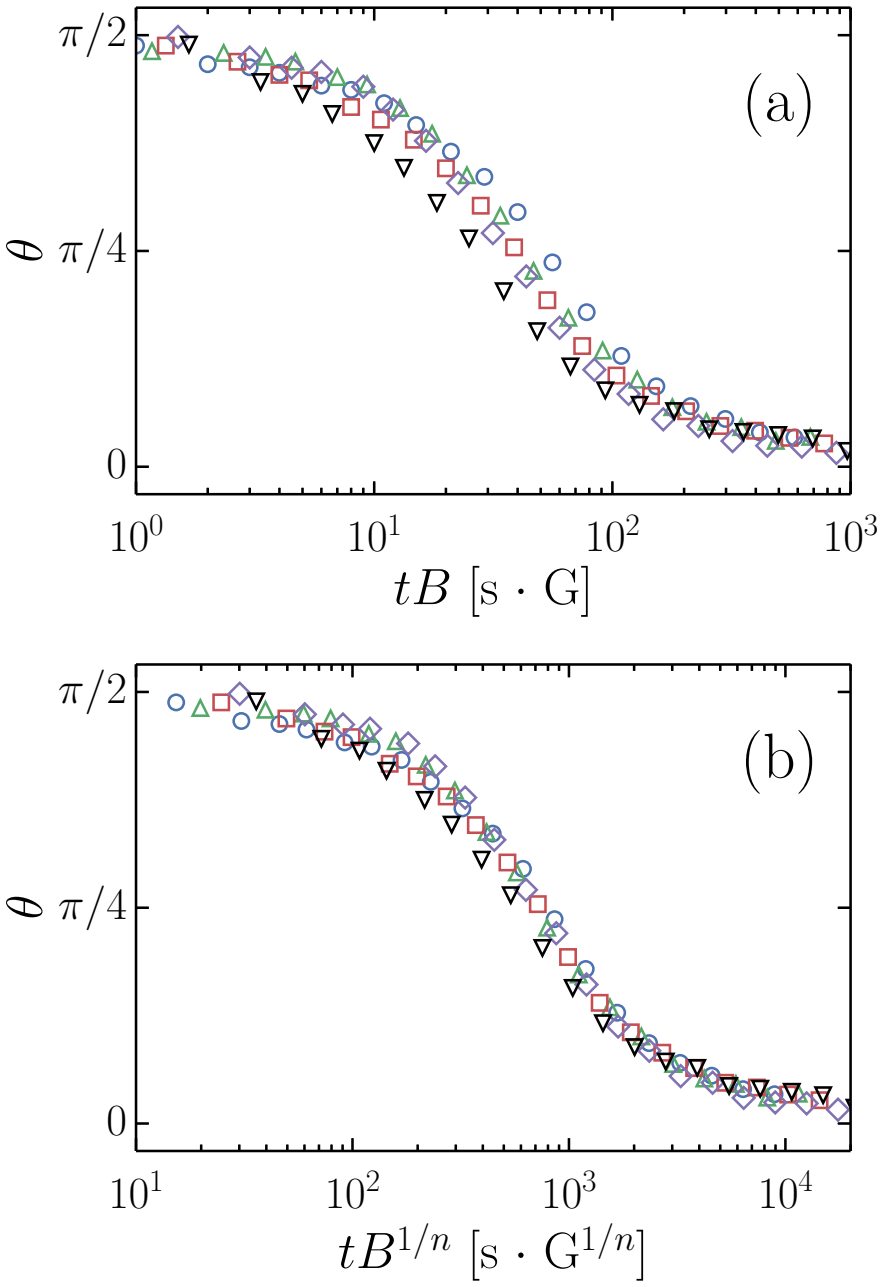

Figure 4.6: Angle between wire and magnetic field as a function of time scaled by magnetic field strength B for field strengths of 60 (circle), 70 (triangle), 80 (square), 90 (diamond), and 100 G (inverted triangle). In (a) time is scaled linearly with field strength; in (b) time is scaled by $B^{1/n}$ with $n = 0.6$, the value obtained from fits to $\theta(t)$. The interface age is $t_a = 8200$ seconds.

we could access experimentally.

Another key feature of the protein-layer response in the active microrheology is the steady evolution of the timescale of the response as the layer ages. This evolution is characterized by the dependence of the power-law drag coefficient ζ_{pl} on layer age, as shown in Fig. 4.7. Because the dimensionality of ζ_{pl} depends in n, for consistency Fig. 4.7 shows values obtained by fitting $\theta(t)$ at different ages using Eq. (4.9) with the flow index fixed at $n = 0.70$, its average at ages $t_a > 3000$ s. As Fig. 4.7 indicates, ζ_{pl} grows approximately exponentially, implying a dramatic slowing of the layer response with increasing age. This trend is insensitive to the precise value of n used to obtain ζ_{pl}. This quasi-exponential increase in the drag is very similar to the behavior seen in earlier studies employing nanowires in active microrheology of protein layers formed from β-lactoglobulin and albumin.[12,103] In those earlier studies, the angular motion was analyzed using a form equivalent to Eq. (4.4), thus assuming a simple viscous response. However, even in those cases, evidence suggested the nanowire microrheology was accessing nonlinear properties of the layer rheology.[12] Here, the nonlinear nature of the response is seen clearly in the values of the flow index n at late ages and in the nonlinear scaling in Fig. 4.6(b). We note that we repeated the active microrheology measurements on lysozyme layers several times and found that, while an evolution to shear thinning like that depicted in Fig. 4.5 was reproducible, the precise values of n at late ages varied between trials, and we observed instances of layer formation in which the response remained essentially viscous-like ($n \approx 1$),

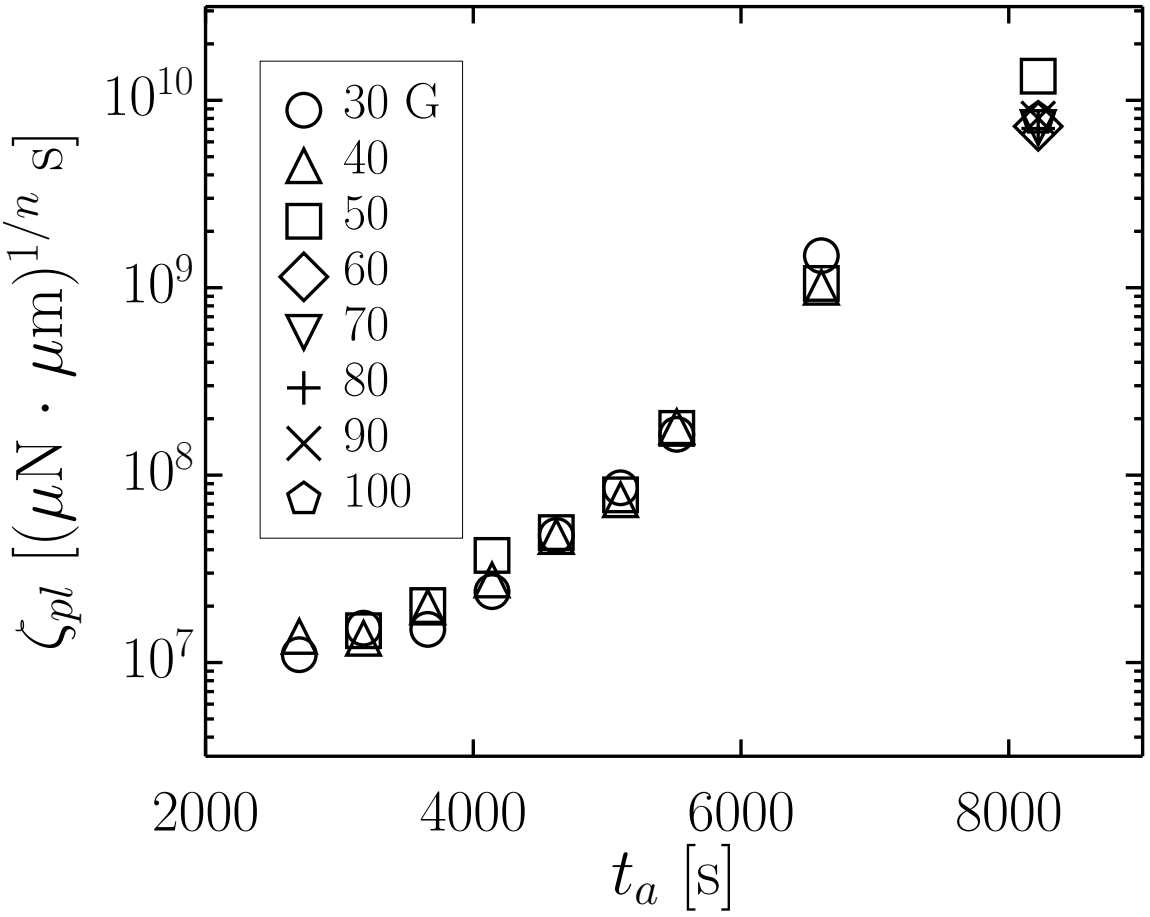

Figure 4.7: Power-law drag coefficient ζ_{pl} as a function of interface age. Values are obtained at a range of field strengths as indicated in the legend and are determined from fits using Eq. (4.9) with the flow index fixed at $n = 0.70$, the average value at ages $t_a > 3000$ s.

with a viscosity that rose dramatically with age much like ζ_{pl} in Fig. 4.7. While we do not have a firm explanation for this variation in n between trials, we believe these observations support the conclusion that the response shown by the lysozyme layers and those reported previously for β-lactoglobulin and albumin share the same basic features of nonlinear behavior characteristic of power-law fluids.

4.5 Discussion

4.5.1 Nature of the Viscoelastic Transition

The linear and nonlinear rheology of lysozyme layers revealed by the passive and active microrheology, respectively, provide a coherent picture of the layers' viscoelastic transition. In this section, we discuss two frameworks in which to interpret this transition: the formation of a soft glass phase and critical behavior associated with gelation. These two frameworks, while not entirely mutually exclusive, imply different possible microscopic mechanisms driving the viscoelasticity. As discussed in Section 4.2 above, reflectivity and spectroscopy studies of lysozyme layers have led to a debate about the degree that lysozyme unfolds upon adsorption. Since the intermolecular interactions at the interface will depend on conformation, understanding the microscopic origin of the viscoelastic behavior of the layers can potentially contribute to this debate. As discussed below, both frameworks are successful in accounting for some but not all aspects of the observed evolution in shear rheology.

4.5.1.1 Soft Glassy Rheology Model

Weak power-law frequency dependence of $G^*(\omega)$, like that implied by the power-law growth in $\langle \Delta r^2(t) \rangle$, is characteristic of the rheology of a broad range of disordered complex fluids including concentrated microgel solutions,[132] foams,[133] paint,[134] intracellular matrix,[135] compressed emulsions,[14] clay suspensions,[136] and liquid-crystal

nanocomposites.[54] In most cases, the power-law exponent typically lies in the range $\alpha \approx 0.1$ to 0.3. The soft glassy rheology model,[55] which explains this response as a general consequence of structural disorder and metastability, provides a unifying theoretical framework for this behavior. Cicuta *et al.* have identified layers of β-lactoglobulin spread on the air-water interface as such soft glassy materials.[39] Significantly, no specific interparticle associations are required to form soft glassy phases, and purely repulsive interactions within a crowded interface would be sufficient. Thus, the picture of lysozyme layers as soft glasses is consistent with the protein retaining its native conformation upon adsorption. In the model, α serves as an effective noise temperature, with systems approaching a glass transition as $\alpha \to 0$. Thus, within this picture the steady decrease in α with layer age seen in Fig. 4.2 points to increasingly glassy dynamics characterizing the structural response of the lysozyme layers. Notably, the soft glassy rhoelogy model also predicts power-law fluid behavior in the nonlinear rheology of these materials. Further, according to the model the flow index decreases on approaching the glass transition. Thus, the linear and nonlinear responses of the lysozyme layers qualitatively fit well together as those of a soft glassy material that approaches a glass phase with increasing age. More quantitatively, however, the soft glassy rheology model predicts a specific relation between the linear rheology and power-law fluid response, $n = \alpha$. The lysozyme layers violate this relation. This violation suggests that, while the model captures many essential features of the observed mechanical response of the layers, the relationship between

structural relaxation and flow in the disordered layers is perhaps more complicated than is assumed in the model.

4.5.1.2 Critical Behavior of Gelation

Materials exhibiting critical stress relaxation on approaching a gel point similarly display weak power-law frequency dependence of $G^*(\omega)$.[137] Technically, power-law behavior over an arbitrarily extended range occurs only at the critical point, and at low frequencies (large lag times) the rheology crosses over from viscous-like to elastic as the gel formation progresses.[137,138] Nevertheless, over a limited dynamic range like that in the passive microrheology measurements, this behavior can appear as a quasi-power law in the mean-squared displacement, $\langle \Delta r^2(t) \rangle \sim t^\alpha$, with a power-law exponent that decreases steadily with age. Indeed, the age-dependent $\langle \Delta r^2(t) \rangle$ in Fig. 4.1 appear strikingly similar to those obtained in microrheology studies of bulk peptide and polymer solutions undergoing three-dimensional critical gelation.[17,138] Identifying the viscoelastic transition in the lysozyme layers with gel formation implies intermolecular bonding capable of creating a percolating network. The stability of native lysozyme against aggregation in bulk solution suggests that such bonding would require significant unfolding to proceed. However, anecdotal evidence indicating the adsorbed protein indeed associates to form a network comes from additional active microrheology experiments at the air interface of lysozyme solutions with very low bulk protein concentrations (below 0.01 mg/ml). At these low concentrations,

which are inadequate to provide full coverage of the interface through adsorption, we observed wires to rotate off-center, as if partially trapped in an "island" of protein that would form only through attractive interactions.

4.5.1.3 Possibility of a Yield Stress at Late Ages

An interesting question is whether the lysozyme layers at very late ages display a yield stress in the microrheology measurements. According to the soft glassy rheology model, the soft glass phase has elastic linear rheology, $\alpha = 0$, and a nonlinear response characteristic of a Herschel-Bulkley fluid as in Eq. (4.7). Similarly, a gel phase would display a yield stress. While a decrease in α with layer age like that in Fig. 4.2 was reproducible in the passive microrheology experiments, the final value of α varied from trial to trial, and in some cases the data at late ages was consistent with $\alpha \approx 0$. Similarly, we also observed some variability in the layer response in the active microrheology, both for different trials and for different wires within a single layer (which we attributed to heterogeneity in the layers), and in some cases wire motion in response to the magnetic torque became imperceptible at late layer ages. However, we were unable to distinguish this immobility as the onset of rigidity and or as an extremely large ζ_{pl}, and in no cases could we say for certain that the lysozyme layers acquired a yield stress. For example, evidence opposing the existence of any yield stress comes from the linear dependence of $\ln(\dot{\theta})$ on $\ln(\sin\theta)$ in Fig. 4.4. The presence of a yield stress would lead to upward curvature on such plots. Fitting to the data at

late age using a Hershel-Bulkley form gives a result consistent with zero yield stress and allows us to place an upper bound on the yield stress of $\sim 5\mu$N/m. In addition, wires in layers at late age rotated fully through $\pi/2$ (when they turned at all) and displayed no measurable recoil when the external field was removed, indicating no stored elastic deformation.

4.5.2 Comparison with Other Protein Layers

A noteworthy feature of the evolution in probe mobility in the passive measurements is the nearly immediate influence of the protein adsorption on the interfacial rheology, as revealed by the onset of subdiffusive behavior, $\alpha \approx 0.6$, less than 200 seconds after interface formation. This rapid impact of adsorption of lysozyme on the interface contrasts strongly with layer formation seen at the air-water interface of β-lactoglobulin solutions of similar concentration.[12] β-lactoglobulin layers forming at the air-water interface remain viscous for a protracted period during which the interfacial viscosity increases slowly and undergo a transition to elastic behavior only at ages of tens of minutes. This viscoelastic transition is further characterized by pronounced mesoscale heterogeneity in colloidal mobility, where some colloids become localized as if trapped in an elastic film while others continue to undergo diffusion as if in a viscous environment.[12] We observe no such pronounced heterogeneity in probe mobility at the interface of the lysozyme solutions. Rather, all probes undergo statistically similar evolution in mobility represented by the ensemble averages in Fig. 4.1. The rapid

evolution in $\langle \Delta r^2(t) \rangle$ seen in Fig. 4.1 is more similar to that observed at the oil-water interface of β-lactoglobulin solutions, where again the onset viscoelastic behavior occurs at a new interface within minutes and no pronounced mesoscale heterogeneity is observed.[102] These different experiments on β-lactoglobulin and lysozyme taken together hence indicate that the evolution in the rheology of interfacial protein layers is not universal, and that depending on specific conditions—such as protein species, hydrophobic phase (air or oil), and how the protein is introduce onto the interface—the viscoelastic transitions can proceed through different scenarios.

4.6 Conclusion

In summary, these microrheology experiments tracking the evolution of the air-water interface during lysozyme adsorption have elucidated the linear and nonlinear properties of the viscoelastic transition that the interfacial protein layer undergoes. As discussed above, interpreting the nature of this transition can contribute to our understanding of the dominant molecular-scale interactions involved in protein-layer formation. In our analysis of the viscoelasticity of the lysozyme layers, we considered two frameworks for interpretation: gelation and the formation to a soft glassy phase. Further microrheology studies that can distinguish more conclusively between these possibilities would be valuable. Indeed, a key challenge in the field of disordered soft materials is to correlate microstructural properties with the broad distribution

of slow relaxation times that give rise to their characteristic rheology. The quasi-two-dimensional geometry of the layers lends itself to experimental approaches that are unavailable in bulk systems. For example, experiments comparing imaging with surface pressure have provided insight into layer formation,[139] and correlating the results of such experiments with microrheology could provide important new information. However, another clear conclusion from the microrheology is the sensitivity of the viscoelastic properties of the layers to the specific conditions under which the proteins encounter and associate with the interface. Hence, any studies comparing rheology with surface structure, surface pressure, other properties would need to take particular care to achieve identical conditions for valid comparisons.

Chapter 5

Mechanical Evolution of Interfacial Layers of SNase: The Role of Protein Conformation in Layer Formation

5.1 Introduction

Previous work by our group on the microrheology of the protein β-lactoglobulin layers[12] supports a picture of layer formation through a gelation process, where proteins associate through intermolecular disulfide bonds. In Chapter 4, my work applied similar techniques to layers of lysozyme in an effort to understand better those aspects

of the viscoelastic transition in protein layers that are universal and those that are system specific. As discussed above, the lysozyme study supported a competing (though not completely mutually exclusive) picture of layer evolution in terms formation of a soft glass phase. One key difference between the β-lactoglobulin layers forming at the air–water interface and those of lysozyme was the prevalence of mesoscale heterogeneity during an extended stage of formation in the β-lactoglobulin. The sources of the differences in layer formation between these systems are difficult to identify. A key feature that generally may differ among different proteins, however, is the degree and type of conformational change that the proteins undergo on adsorbing and the stability of the protein against these changes. In this chapter we describe a study designed to isolate the role of protein conformation in the evolution of interfacial layers' mechanical response by exploiting a structural feature of the protein Staphylococcal nuclease (SNase). We studied layer formation by wild-type SNase—the protein as it is found in nature—which assumes a folded conformation for the solution conditions considered and an engineered variant sharing almost the same chemical composition but having a completely disordered, unfolded structure.

Changing one particular residue catastrophically destabilizes the folded structure of SNase. This sensitivity is due to a particular structural feature of SNase illustrated in the ribbon diagram in Figure 5.1. SNase exhibits a structural motif known as a beta barrel, a large beta-sheet that twists and coils to form a closed structure in which the first strand is hydrogen-bonded to the last. At one opening of this barrel, an α-

helix acts as a lid, keeping water from flooding the hydrophobic interior of the barrel. The helical structure of an α-helix relies on a rotational degree of freedom common to all amino acids save one, proline, whose cyclic side chain lends it a distinctive structural rigidity. When an amino acid in the center of the α-helix (at residue 62, which happens to be threonine) is replaced by proline, the arc of helix is kinked, effectively breaking the lid, exposing the hydrophobic interior of the beta barrel to water, and ruining the stability of the entire folded structure. Here, we describe comparative microrheology experiments on layers of wild-type and disordered SNase adsorbed to the air–water interface. From differences in the mechanical evolution of the layers formed by the two proteins, we speculate on the role of protein unfolding in the evolution of the mechanical response of the interface.

5.2 Experimental Methods

5.2.1 Protein Fabrication

The disordered SNase was fabricated by our collaborators in the lab of Prof. Bertrand Garcia-Moreno E. using the polymerase chain reaction (PCR). PCR is a well established technique in biology, briefly reviewed here for interested readers. To manufacture protein with a certain engineered mutation, a fragment of DNA expressing the desired mutation is synthesized by chemically joining base pairs. This is a primer. A plasmid (circular ring of DNA) is obtained which largely compliments

Figure 5.1: This ribbon diagram shows the secondary structure of SNase. The α-helix, positioned front and center from this perspective, acts a lid on the beta barrel (a beta sheet curved into a closed structure) beneath it. The interior of the beta barrel is hydrophobic, and the α-helix helps keep water out. Change one residue in the middle of the helix creates a kink, effectively breaking the lid and ruining the stability of the folded structure.

the fragment except at the site of the mutation. The primers and plasmids are combined in a soup of loose ribonucleotides and DNA polymerase, which marches along the chain and builds a DNA polymer along complemtary strands. The original primers are extended to full strands, and more full copies are made as the process proceeds. Finally, bacteria are made to imbibe the plasmids, and they manufacture mutated proteins in accordance with the mutated DNA. The product is purified and flash-frozen into droplet-sized beads for storage.

5.2.2 Sample Preparation

The frozen protein solution was thawed and diluted to 0.05 mg/ml in a 10 mM sodium phosphate buffer, pH 7.4. Then, following the protocol developed for the lysozyme study described in Chapter 4, a volume of 0.5 ml was placed into a sample cell, where an air–water interface was formed. Colloidal probes were spread across the interface, dispersed in a solution of equal parts water and isopropyl alcohol.

5.2.3 Active Microrheology

The experiments focused on active microrheology measurements employing ferromagnetic Nickel nanowires using procedures like those described in detail in the previous chapters, wherein the wires' orientations are tracked following a 90° step change in the direction of an applied magnetic field. A total of 12 trails were con-

ducted, 6 using wild-type SNase and 6 using the disordered variant. Measurements were performed as a function of age. Up to 15 separate wire rotations were performed at each age, using field strengths of 10–100 G, selected to match the stiffness of the layer so as to generate an observable wire rotation.

5.3 Results

5.3.1 Wild-Type SNase Layer Evolution

At early ages in the layer's evolution, the wild-type layers were always found to exert a simple viscous drag on the wire. The angle between the wire axis and the final field direction as a function of time was well described by Eq. (4.4),

$$\theta(t) = 2\tan^{-1}\left[\exp\left(-\frac{\mu B}{\zeta_r}(t-t_0)\right)\right].$$

where, as in Chapter 4, μ is the wire's magnetic moment, B is strength of the externally-applied magnetic field, ζ_r is a rotational drag coefficient, and t_0 is an experimental parameter that accounts for uncertainty in the time that the wire begins rotating in response to the field change. Figure 5.2(a) shows rotational trajectories $\theta(t)$ for a wire of length $L = 8.05$ μm in a wild-type layer at age $t_a = 13$ minutes under varied field strengths. Fitting Eq. (4.4) to each rotation gives a rate, $K = \mu B/\zeta_r$, which is plotted against field strength B in Figure 5.2(b). The rotational drag coef-

ficient ζ_r can be extracted from the slope of linear regression to $K(B)$. Then, using Eq. (4.5), $\zeta_r = 1.48L^2\eta_s$, we obtain the interfacial viscosity η_s. Thus, several wire rotations performed in succession at roughly the same age t_a are reduced to a single number characterizing the linear shear rheology of the layer at that age. Figure 5.3 shows how, in several identically-prepared trials of wild-type SNase, the viscosity increased exponentially with the age of the layer over a wide range of ages. The least-squared best fit of an exponential, $\eta_s = \eta_{s,0}\, e^{\Gamma t}$, to this data is also shown, and it gives $\Gamma = 1.41 \pm 0.05 \times 10^{-5}$ s^{-1} and $\eta_{s,0} = 0.10 \pm 0.2$ μPa·m·s. (The Boussinesq number for this interfacial viscosity are wire length is 12.) At ages later than those represented in this figure, the wire rotations changed qualitatively in a way that could no longer be explained in terms of simple viscous drag.

Figures 5.4 and 5.5 show two kinds of deviation from viscous response that were observed. Figure 5.4, shown with a best-fit viscous form, turns more quickly through the middle of its rotation than can be explained by viscous drag, which is suggestive of shear-thinning and qualitatively similar to the power-law fluid behavior shown previously in Figure 4.3(b). The second example, in Figure 5.5, shows what appears to be an elastic jump at the beginning of the rotation as the layer yields. More detailed analysis would be needed to see whether this indeed holds. Future work will apply the analysis of Chapter 4 to this data.

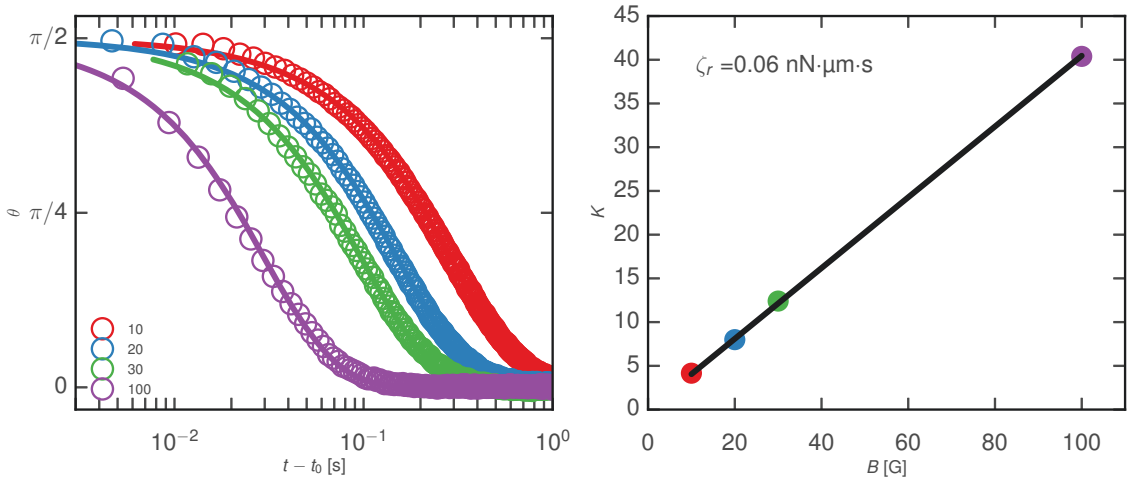

Figure 5.2: (a) Rotational trajectories $\theta(t)$ of a wire in a wild-type SNase layer at age $t_a = 13$ minutes under a 90° step change in magnetic field direction, under varied field strengths. Eq. 4.4 is fit to each rotation, giving a rate $K = \mu B/\zeta_r$, which is plotted against field strength B in (b). The slope of the linear regression to this data is used to compute ζ_r.

5.3.2 Disordered SNase Layer Evolution

In contrast to the wild-type layers whose microrheology showed strong trial-to-trial reproducibility, the wire rotations in layers of disordered SNase showed considerable trail-to-trail variation. Measurements in three of the six trials could be well-described by viscous drag at early ages, as in the wild-type trials. The others showed a more complex response from the beginning. The interfacial viscosities of those showing viscous behavior are plotted in Figure 5.6. The change in viscosity is much less pronounced and occurs more slowly than in wild-type layers. The magnitudes of the viscosity in the disordered layers also shows more variability among different trials. (To aid the comparison, note that Figures 5.3 and 5.6 are plotted on the same scale and that the fit to the data in Fig. 5.3 is shown alongside the data in Fig. 5.6.)

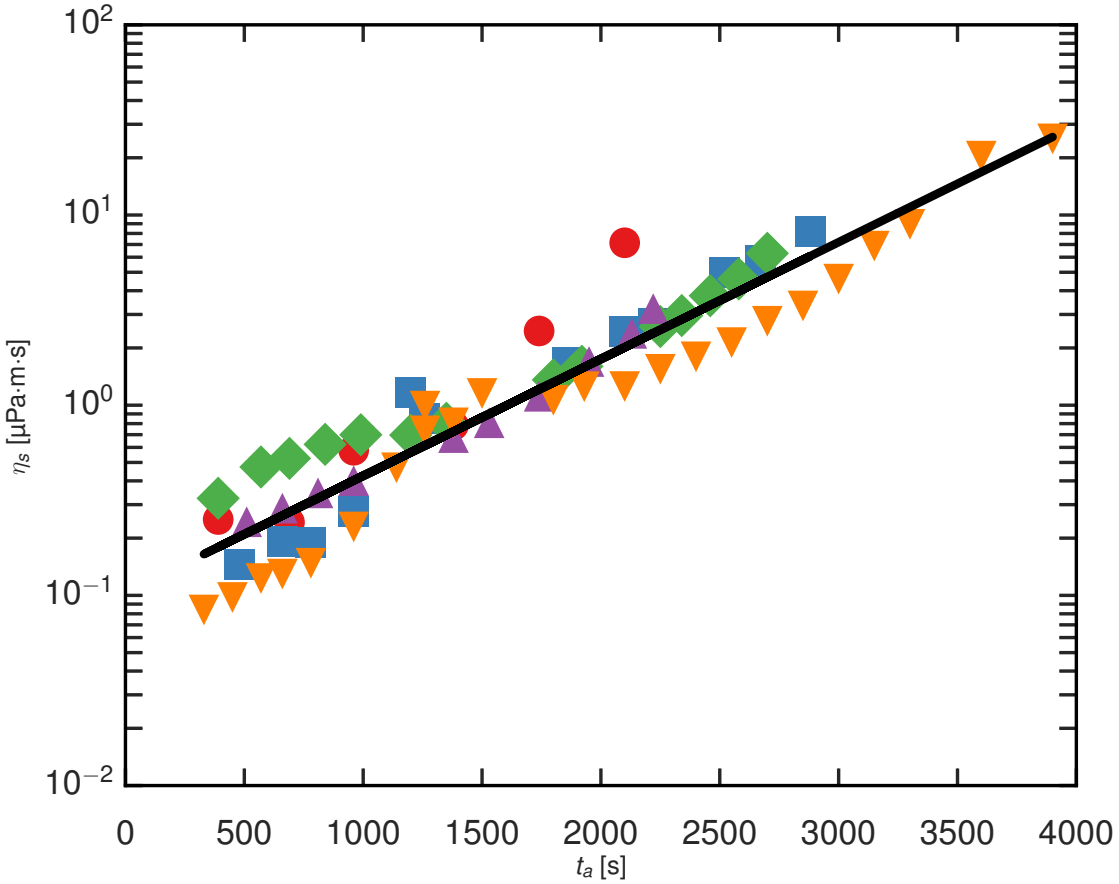

Figure 5.3: The interfacial viscosity of a wild-type SNase layer, computed from wire rotation curves like those in Figure 5.2, rose exponentially with layer age t_a. The black line shows an exponential best fit to the data, given in the text. Data from several identically-prepared trails are shown, differentiated by plot markers.

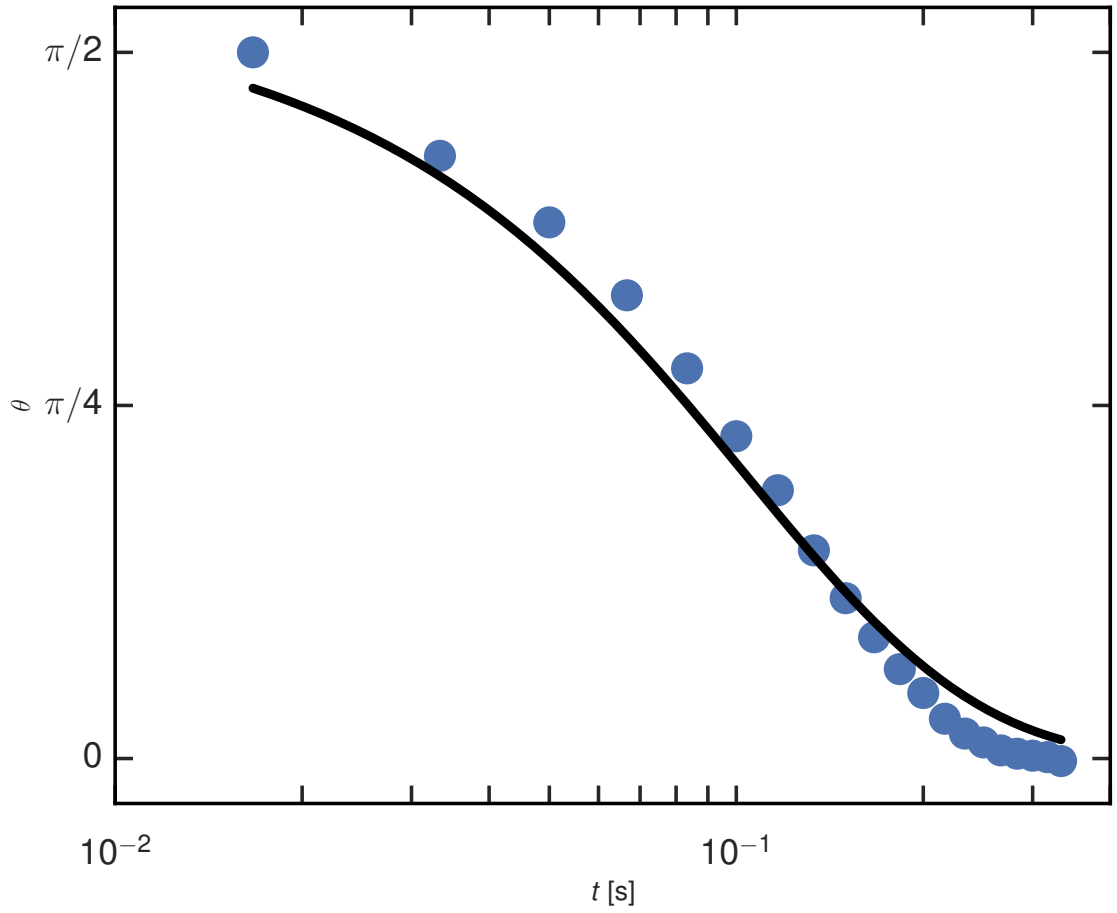

Figure 5.4: This rotation, performed under 100 G in a layer of disordered SNase aged 2 hours, cannot be well described by a viscous response. The wire turns more quickly during the middle of its rotation, which is suggestive of shear-thinning and is qualitatively similar to power-law fluid behavior, as described in the text.

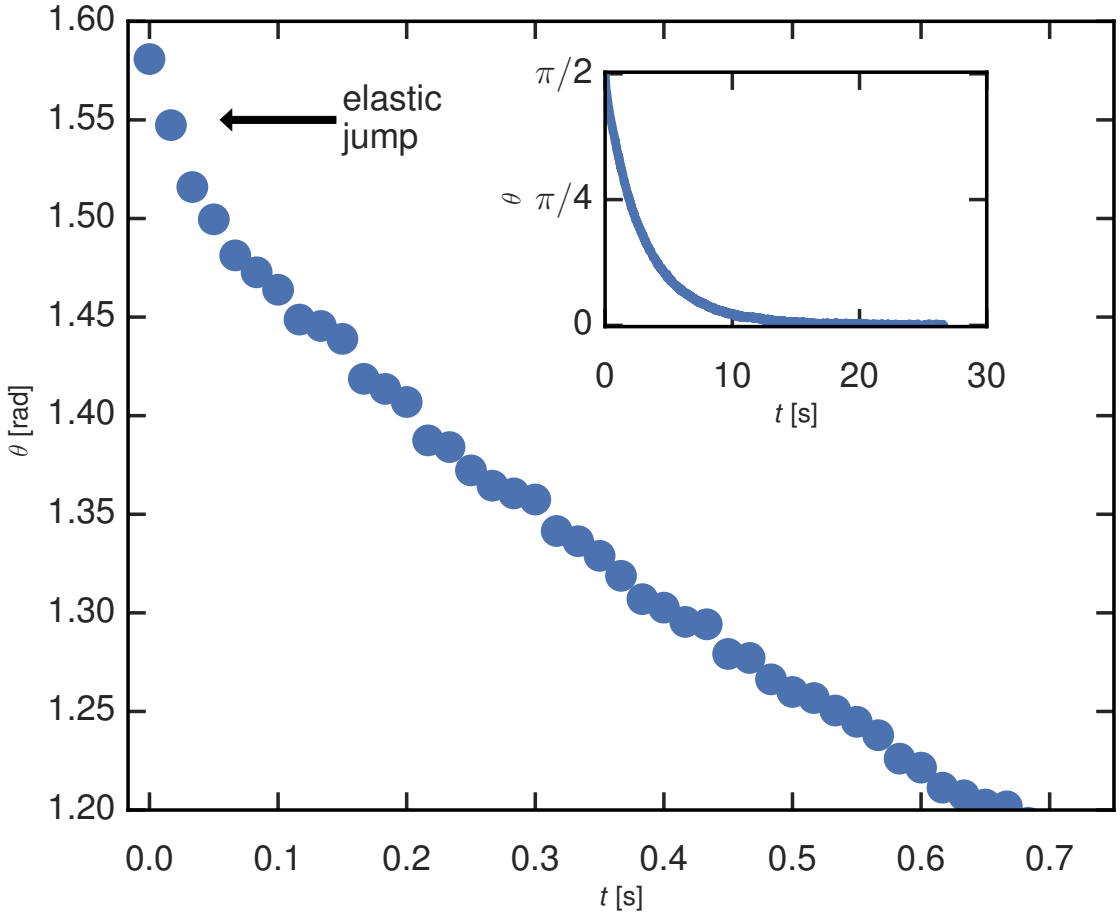

Figure 5.5: In this rotation, also performed under 100 G in a layer of disordered SNase aged 2 hours, the layer appears to yield quickly to the initial torque, evincing a mostly elastic response followed by a more liquid-like response as the wire completes a full 90° rotation. (It does not recoil.)

This apparent variability between trials of layer formation by disordered SNase may actually be a proxy for spatial variability in the layers. Straight, unaggregated wires are sufficiently sparse, and the evolution of the layer sufficiently fast, that it is not practical to observe more than one or two different wires in a given trial. Once a one or two usable wires are located in the layer, they must be carefully followed, and there is no time to locate an ensemble of wires and regions to compare before the layer has aged dramatically. Thus, we speculate that the layers generated by disordered SNase exhibit mesoscale (or larger) spatial heterogeneity that is not directly captured in the active microrheology measurements. Complementary passive microrheology measurements on ensembles of spheres could provide support for this picture.

5.4 Discussion & Conclusion

This comparative study of wild-type and disordered SNase has revealed how protein conformation in the bulk can play a dramatic role in the evolution of an interfacial layer's mechanical response during its formation. The weak age-dependence and strong variability observed in disordered films, which we associate with mesoscale spatial heterogeneity that sets in at very early ages, suggests a layer-formation process that is far from equilibrium. In contrast, the reproducible, steadily evolving, and apparently homogeneous layers formed by the wild type suggests a formation process in which the system has the opportunity to anneal. One possibility is that

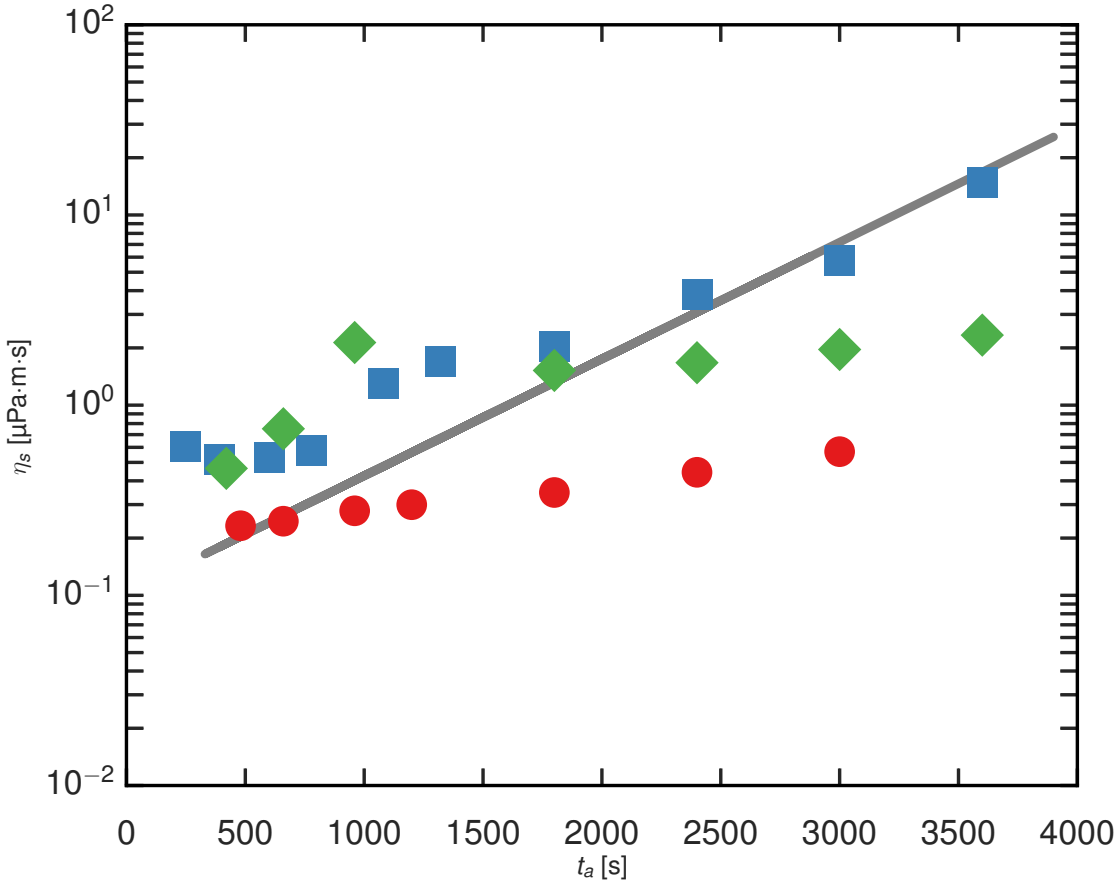

Figure 5.6: In some trials or regions of a disordered SNase layer, the layer exerted viscous drag on a rotating wire with a viscosity that rose slowly in a way that can plausibly be interpreted as a weak power-law dependence on layer age. Compare to the much more dramatic and robust exponential increase exhibited by wild-type SNase in Figure 5.3. The best-fit line from *that* figure is shown here in gray for comparison. Data from several identically-prepared trails are shown, differentiated by plot markers. As noted in the text, some trials or regions of disordered SNase layers never exhibited viscous behavior.

slow unfolding of the wild type at the interface introduces a rate-limiting step that allows the layer to acquire homogenous, dense coverage (leading to large viscosities) before non-viscous behavior, driven by protein association, sets in.

Chapter 6

Dynamical and Mechanical Evolution of Bacterial Biofilms at the Oil–Water Interface

6.1 Introduction

When bacteria cells in suspension encounter a bounding surface, they form biofilms comprising adherent cells in a complex matrix of extracellular polymeric substances including polysaccharides and surfactants secreted by the bacteria.[50] On solid surfaces, biofilms are ubiquitous and widely studied. It has been estimated that 99% of the world's population of bacteria are found in biofilms in various stages of growth.[140,141] Biofilms provide important biological functions for the bacteria within

them, including protection from antimicrobial agents secreted by competing species or deliberately added to prevent infections.[140,142] Because of this protective property, and the fact that they are notoriously difficult to remove, biofilms often have detrimental consequences. For example, biofilms on medical implants and equipment are often resistant to antibiotics and contribute to the spread of disease. Furthermore, owing to their mechanical toughness, biofilms can disrupt or impede the proper function of wide ranges of equipment, for example, by increasing the drag on ships, by decreasing the efflux from outlets from factories, and by fouling filters and bioreactors.[143] Biofilms can also be beneficial, for example, in the context of bioremediation, in which bacteria and the films they create remove toxins from their surroundings. For example, bacteria attach to, metabolize, aggregate and sediment undesirable substances, aiding wastewater treatment.[144] A variety of bacteria are known to biodegrade alkanes and are exploited in the cleaning of soils and sands contaminated by oil.[145] The microstructure of such biofilms resembles, from a physical perspective, a disordered colloidal suspension in a polymer or gel solution. The evolution, structure, and mechanics of biofilms on solid surfaces are relatively well studied, including studies of the rate of attachment and its dependence on flow environment,[146] the rheology[147] and microrheology of the films[59] and changes to cell physiology.[148] The study of biofilm structure and function continues to reveal important insights into issues ranging from the evolutionary advantages of cooperation,[149,150] to strategies for displacement of colonies by competing species which rely on invasion of motile

cells into biofilms which impart transient biofilm permeability.[151]

Bacteria also form biofilms at fluid interfaces; the stages of growth of these films and their mechanics are less studied. At air-aqueous interfaces, biofilms have been studied in terms of their rate of growth and their micromechanics, motivated in part by interest in cystic fibrosis lung infections and the behavior of airborne infectious agents.[152] These studies help reveal biofilm microstructure[6] and inform strategies to manipulate them. Biofilms at oil-water interfaces have also been studied, in part motivated by bioremediation of oil spills. Natural blooms of bacteria occur in the presence of spilled oil, and much has been done to increase the speed and ability of the bacteria to degrade pollutant hydrocarbons.[63,64]

The ability of bacteria to attach to oil-aqueous interfaces is well documented. One widely used assay, with acronym BATH/MATH for bacterial or microbial adhesion to hydrocarbons, relies on optical density measurements of aqueous phases to quantify depletion of microbes from suspension containing dispersed droplets of hydrocarbons, and to thereby infer the adsorption of microbes to oil/water interfaces.[145] More direct methods involve imaging oil-water interfaces and directly visualizing the microbes as they attach to the interface.[153]

The external surfaces of bacteria that biodegrade oils are highly complex, presenting surface structures such as pili, lipopolysaccharide O antigen or teichoic acid, and exopolysaccharides.[141] The wide range of surface chemistries and structures presented on the bacterial surfaces and their varying shapes strongly affect their ability to ad-

here to and subsequently degrade oil. Interfacial adhesion has been found to play an important role in bacterial bioremediation of sparingly soluble hydrocarbons.[63] Immediately after encountering a bounding surface, bacteria can remain motile. Bacteria at solid-fluid interfaces have been documented to behave differently than those at fluid-fluid interfaces, for example exhibiting counterclockwise circular motion at an air-water interface, and clockwise circular motion on glass surfaces.[154] In systems with surfactant-producing bacteria, there is contention regarding the influence of the secretions on the behavior of the biofilm; one study described an immobilization of the interface, where another suggested that the surfactants contributed to superdiffusion at the air-water interface.[155]

Here, we study the time evolution of bacterial biofilms at and near planar oil-water interfaces by tracking the mobility of passive colloidal tracers at the interface. This work was part of a wider study of these films in collaboration with the Stebe group at U. Penn that also included biofilms on pendant drops of oil suspended in bacterial suspensions. Here, I report only on the particle tracking part of the study, in which I played a lead role working with Liana Vaccari and Aayush Singh. I will also mention briefly the findings of the pendant-drop study for context.

The particle tracking and pendant drop experiments together reveal three stages of biofilm evolution. Initially, the preponderance of bacteria near the interface are highly motile, and we refer to this as an "active" layer. Over time, a biofilm of adherent bacteria trapped in the interface forms; in the absence of nutrient addition, these

bacteria are non-motile. At this stage, the biofilm is viscoelastic. Finally, the biofilm becomes an rigid "skin" that wrinkles upon compression. The particle-tracking experiments provide information about the first and seconds stages, whelk the resistance to bending in the rigid stage is best probed via the pendant-drop experiments. We address the film properties during the first two stages from a fundamental perspective in the context of active, soft-glassy systems.

6.2 Experimental Methods

6.2.1 Sample Preparation

Pseudomonas sp. ATCC 27259, strain P62 was chosen as a model organism. Bacteria were cultured in ATCC Medium:3 Nutrient Broth in 24 ppt Instant Ocean to simulate a middle-level marsh salinity. The cultures were grown on a table-top shaker at 150 rpm at room temperature for 24 h to mid-to-late exponential phase. In the biofilm characterization experiments, a bacteria suspension free of surface active proteins from the nutrient broth was prepared with a typical washing protocol[145] by centrifuging the culture for 5 minutes at 5000 x g, decanting the nutrient broth or supernatant and re-suspending the pellet in Instant Ocean three times. Control microrheology experiments on dilute nutrient broth absent of bacteria were performed to confirm to the observed evolution of the interface was due to bacteria and biofilm development and not to residual surface-active species of the nutrient broth.

6.2.2 Particle Tracking

The particle-tracking measurements are performed in a 1.0 cm ID cylindrical vessel with an inner surface whose bottom half is aluminium and top half is Teflon. When the cell is filled to the appropriate level, the aluminum-Teflon seam pins the oil-water interface, creating a flat surface with no meniscus. The base of the cylinder rests on an untreated glass coverslip, sealed by a PDMS gasket. To begin each experiment, the cylinder is filled nearly to the seam with 0.5 ml of Instant Ocean. A spreading solution containing charge-stabilized polystyrene spheres (Interfacial Dynamics Corp.) with radius R = 0.5 μm in a mixture of equal parts by volume water and isopropanol is prepared in advance and sonicated to disperse any colloidal aggregates. To introduce the colloids to the interface, a 10-μL droplet of the spreading solution is gently placed in contact with the Instant Ocean surface. The solution wets the surface, and the colloids, slightly denser than water but hydrophobic, disperse across the surface. Droplets of hexadecane are then promptly applied to the surface until it is completely covered. The age of the sample t_a is measured from this instant of interface formation. After each experiment, the cylindrical vessel is cleaned thoroughly by scrubbing and sonicating in Alconox soap solution, acetone, and isopropanol, and then rinsed repeatedly in deionized water. We observe the colloids at the interface using an upright bright-field microscope with a 50x objective. A camera (Zeiss AxioImager M1m) records a 200-μm by 150-μm field of view at 60 frames per second, which set the shortest lag time over which probe motion can be characterized. Probe

trajectories are extracted from the video using the custom Python implementation of the widely used Crocker-Grier multiple-particle-tracking algorithm[74] described in Chapter 3. Static and dynamic errors in the particle tracking are accounted for to avoid distortion in the measurements of particle trajectories.[72] Trajectories are extracted from video segments short enough in duration (typically 1-2 minutes) so that no apparent change in particle mobility due to the evolving interfacial properties can be discerned over the selected time span. Typically 30-200 probes are in view at a time, constituting at most 0.3% surface coverage.

6.3 Results

The interface between hexadecane and the seawater bacteria solution evolves with age, changing measurably over a timescale of minutes. As mentioned above, we observe three qualitatively distinct stages of the biofilm development during which it can be characterized as (i) active, (ii) viscoelastic, and finally (iii) rigid. The first two stages of development are investigated primarily through the particle-tracking experiments, while the third stage of biofilm rigidity is characterized using the pendant drop experiments.

6.3.1 Tracer Motion at an Active Interface

Immediately following the formation of a fresh interface between the oil and bacteria suspension, bacteria were sometimes observed to associate with the interface and remain motile once attached. Bacteria attach to the interface in both end-on and side-on orientations. Often, bacteria at the surface were accompanied by a population of especially mobile bacteria just beneath the interface. In these cases, the colloidal motion at the interface was strongly affected by hydrodynamic interactions with the swimming bacteria at the surface and by direct collisions with those at the surface. Typically, the concentration of swimming bacteria embodied a 10% area fraction of the interface—large enough to lead to collective motion such as swirling, which influenced the colloidal motion. A substantial literature has addressed the mobility of colloidal probes in the presence of motile bacteria and other microbial swimmers both in bulk (3D) and in quasi-two-dimensional contexts.[156–165] One motivation for studying the colloidal dynamics in suspensions of swimming microbes is their utility as model systems for investigating the nonequilibrium statistic mechanics of active complex fluids. In addition, the colloid motion provides insight into biomixing, the enhanced transport of nutrients and other material by active suspensions. Since biofilm formation relies on the transport of polysaccharides and other constituents to and within the interface, such biomixing could be an important feature of the film development. Hence, we have characterized the colloidal motion during this active phase in some detail.

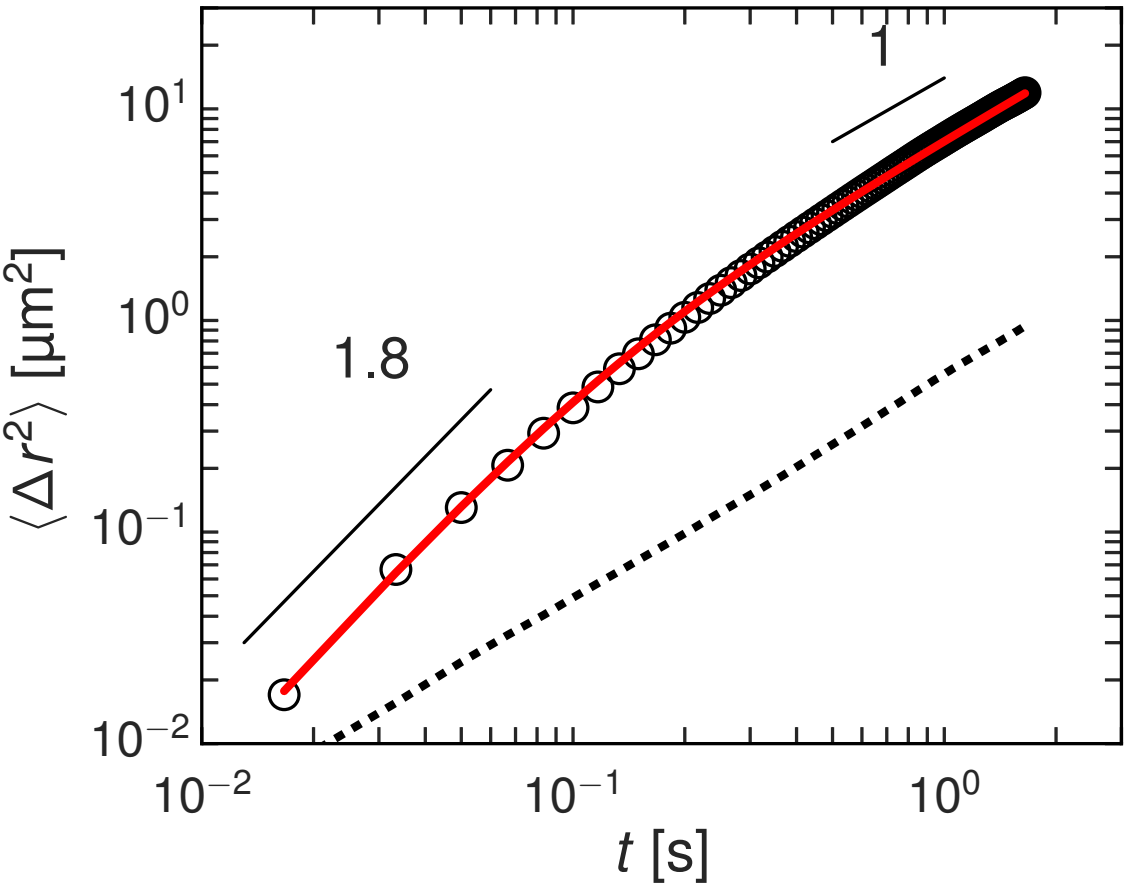

Figure 6.1: Ensemble-average mean-squared displacement of colloidal tracers during the initial, active stage of biofilm formation at an oil-water interface. For reference, the dashed line displays the mean-squared displacement of colloids at the oil-water interface in the absence of bacteria. The solid line displays the result of a fit using Eq. **??**.

Figure 6.1 shows the colloids' ensemble-average mean-squared displacement, $\langle \Delta r^2(t) \rangle = \langle (\vec{r}_i(t'+t) - \vec{r}(t') \rangle_{i,t'}$ where the average is over particles i and time t, during this active stage of biofilm formation. For reference, the mean-squared displacement of colloids at the oil interface of pure Instant Ocean containing no bacteria is also shown. In the absence of bacteria, $\langle \Delta r^2(t) \rangle$ varies linearly with lag time t indicating simple diffusion, $\langle \Delta r^2(t) \rangle = 4D_0 t$, with a diffusion coefficient, $D_0 = 0.12 \mu m^2/s$, consistent with the viscosities of water and hexadecane. The mean-squared displacement of the colloids at the active interface similarly varies linearly with t at large lag times, but with an enhanced effective diffusion coefficient. At smaller lag times, the mean-squared displacement grows more rapidly than linearly, indicating superdiffusive motion. Such superdiffusive motion is a common feature of colloidal motion in microbial suspensions and signals temporal correlations in the forcing of the colloids due to hydrodynamic interactions with the swimmers. A simple model for these correlations ascribes to them a single characteristic correlation time τ, so that the particle velocities have an exponentially decaying memory, $\langle \vec{v}(t') \cdot \vec{v}(t'+t) \rangle \sim \exp(-t/\tau)$.[156] Such velocity correlations lead directly to a mean-squared displacement of the form[165]

$$\langle \Delta r^2(t) \rangle = 4D \left[t + \tau(e^{-t/\tau} - 1) \right] \tag{6.1}$$

In the limit of short lag times, $t \ll \tau$, this form predicts ballistic motion, $\langle \Delta r^2(t) \rangle = \frac{2D}{\tau} t^2$; and at large lag times it reduces to diffusive motion, $\langle \Delta r^2(t) \rangle = 4Dt$, with effective diffusion coefficient D. The solid line in Fig.6.1 is the result of a fit using

this form, which describes data accurately and gives $D = 1.80.1\mu m^2/s$ and $\tau = 0.053 \pm 0.007$ s. The value of D in relation to the diffusivity in the absence of bacteria, $D/D_0 \approx 15$, indicates that biomixing strongly influences the interface during this early stage of biofilm formation. We note further that this factor likely underestimates the enhancement in tracer mobility due to the swimming bacteria since, as described below, even at these early interface ages the incipient biofilm imparts an interfacial viscosity that reduces thermal diffusivity.

The success of Eq. (6.1) in capturing the form of $\langle \Delta r^2(t) \rangle$ is consistent with several earlier studies of colloidal motion in active microbial suspensions and hence indicates that the velocities of tracers in such suspensions indeed have exponentially decaying memory. However, we can interrogate these correlations more directly by defining an instantaneous direction of motion for each particle,

$$\hat{n}(t) = \frac{\vec{r}_i(t) - \vec{r}_i(t+\delta t)}{|\vec{r}_i(t) - \vec{r}_i(t+\delta t)|} \tag{6.2}$$

where $\delta t = 1/60$ s is the time between successive video frames and i labels the particles, and by examining its time-time autocorrelation function,

$$\Phi_n(t) = \langle \hat{n}_i(t+t') \cdot \hat{n}_i(t) \rangle_{i,t'} \tag{6.3}$$

The significance of $\Phi_n(t)$ is that it quantifies the persistence in the direction of the colloids' trajectories. As shown in Fig. 6.2, $\Phi_n(t)$ is effectively zero at $t > 0.15$ s, set-

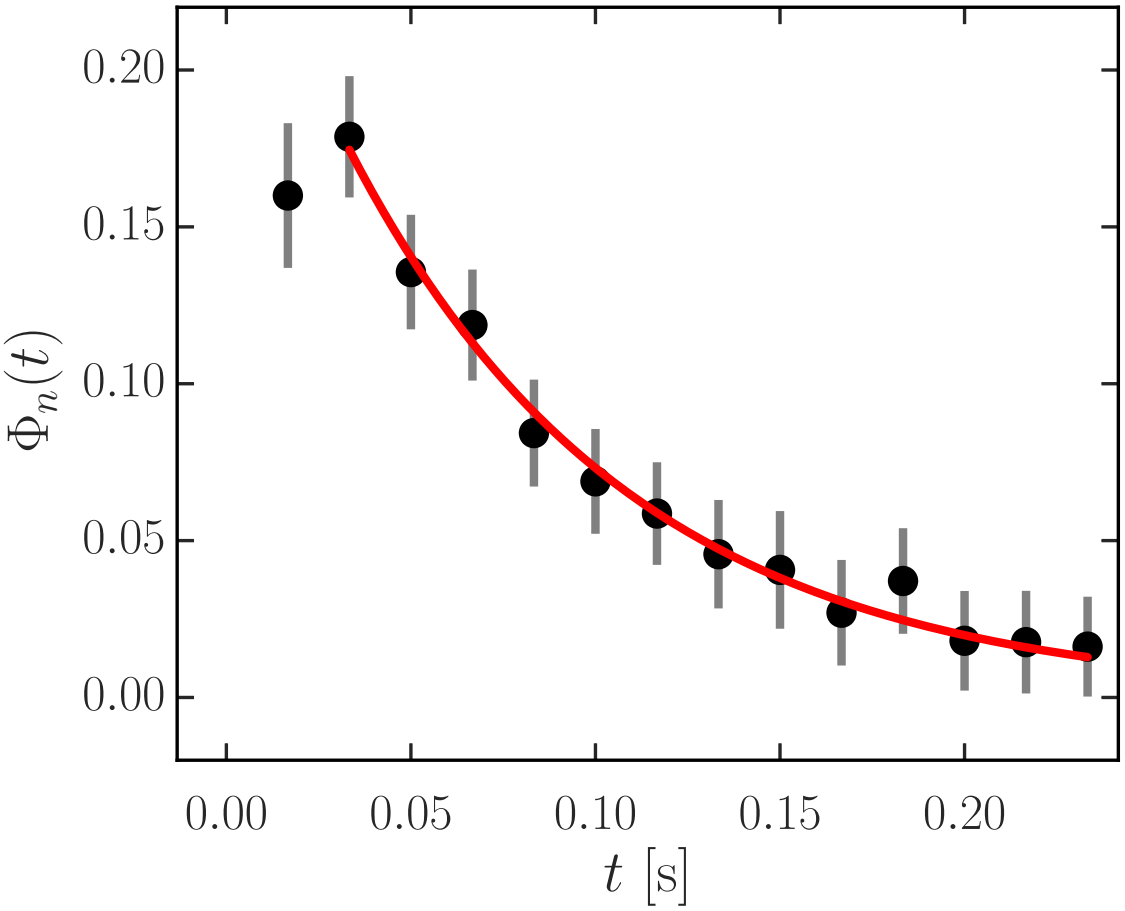

Figure 6.2: Time autocorrelation function of the direction of instantaneous tracer displacements during the active stage of biofilm formation. The line shows the result of an exponential fit to the data at large times ($t > 0.03$ s).

ting the typical time required for the colloids' direction of motion to randomize completely. Notably, $\Phi_n(t)$ does not decay monotonically but has a peak near $t = 0.03$s. We attribute this peak to a tendency for colloids to follow "U-shaped" trajectories on short time scales due to hydrodynamic interactions with bacteria swimming past in close proximity,[163] and hence to make negative contributions to $\Phi_n(t)$. At larger times, $\Phi_n(t)$ decays exponentially, as shown by the line in Fig. 6.2, which is an exponential fit to the data. The correlation time obtained from the fit is 0.075 ± 0.01 s, which is in reasonable agreement with the characteristic time τ for velocity correlations implied by fitting $\langle \Delta r^2(t) \rangle$ with Eq. (6.1). Thus, through $\Phi_n(t)$ we observe directly the nature of the correlated tracer dynamics in an active suspension inferred by the analysis of $\langle \Delta r^2(t) \rangle$.

While the colloids' Brownian dynamics at large lag times with diffusivity D suggest that the suspension of swimming bacteria act like a thermal bath with large effective temperature, several previous studies have emphasized that the statistical properties of the colloidal displacements differ from those expected for a system in thermal equilibrium.[160,163,165] These differences are apparent in the probability distribution function (PDF) for displacements at fixed lag time $P_t(\Delta x)$, where Δx is the displacement along one direction. Figure 6.3 shows $P_t(\Delta x)$ at $t = 0.0167$ s, 0.15 s, and 1.3 s, lag times spanning the superdiffusive and diffusive behavior in $\langle \Delta r^2(t) \rangle$. The PDFs of particles undergoing thermal diffusion in equilibrium would be Gaussian. In all cases, the PDFs in the active, incipient biofilm show clear deviations

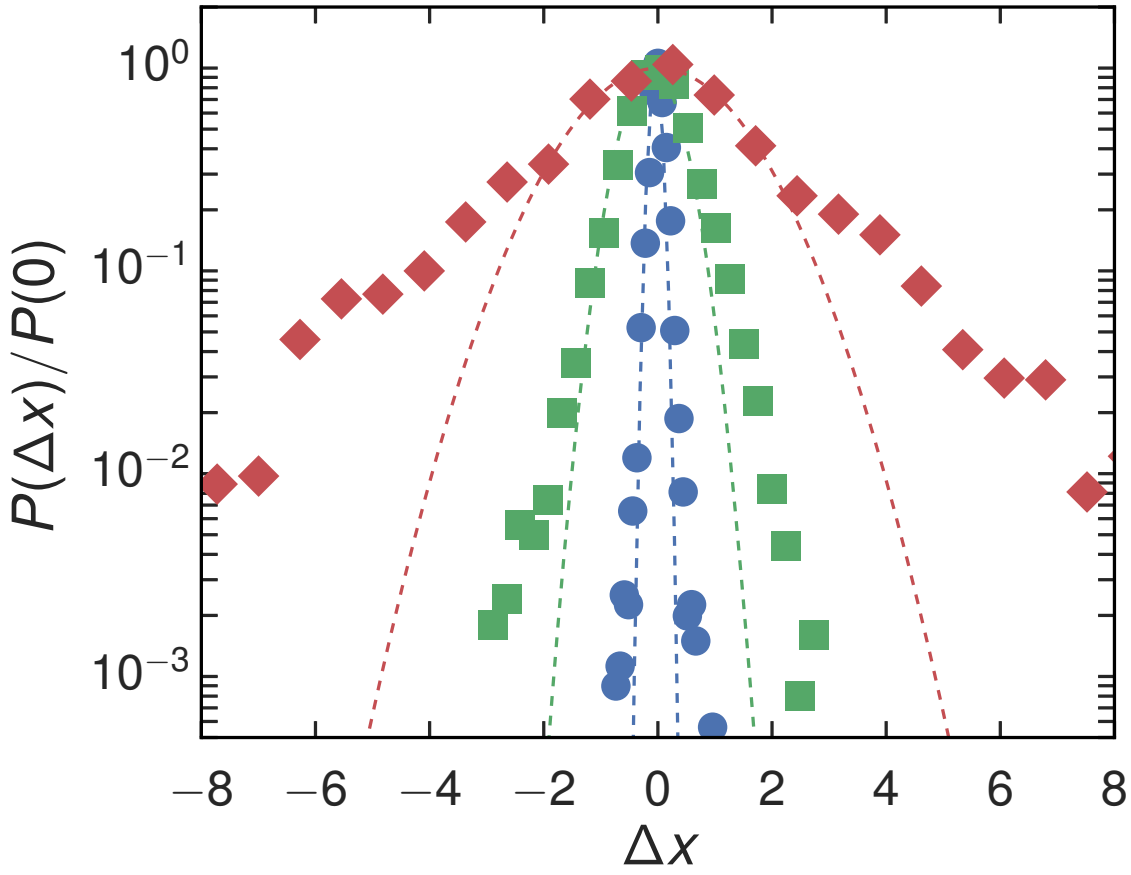

Figure 6.3: Normalized probability distribution functions for colloidal displacements at lag times of 0.016 s (blue), 0.15 s (green), and 1.3 s (red) during the active stage of biofilm formation. The solid lines display the results of fitting Gaussian lineshapes in the regions of the peaks of the distributions, highlighting the enhanced, non-Gaussian probability for large displacements.

from Gaussian forms, with tails at large $|\Delta x|$ that signal enhanced probability of large displacements. Qualitatively similar non-Gaussian PDFs have been observed previously among tracers in microbial suspensions and have been associated with advection-enhanced large displacements due to hydrodynamic encounters between the colloids and swimmers.[163,165] To compare the form and magnitude of the non-Gaussian contributions to $P_t(\Delta x)$ at different lag times more closely, we plot in Fig. 6.4 the normalized PDFs with displacement normalized by the root mean-squared displacement. Remarkably, the normalized PDFs collapse onto a single lineshape, indicating that the distribution function maintains a self-similar form with increasing lag time. Such self similarity is generally unexpected and implies particular attributes about the colloidal dynamics, including (i) that the fraction of colloids in the non-Gaussian population remains constant over the range of lag times probed, and (ii) that the Gaussian and non-Gaussian displacements grow as the same function of lag time, first superdiffusively at short lag times and then diffusively at longer lag times. Self-similar distributions with non-Gaussian tails were also observed among tracer displacements within bulk (3D) suspensions of the eukaryotic microorganism Chlamydomonas.[163] However, in that case, $\langle \Delta r^2(t) \rangle$ displayed diffusive behavior over the entire range of lag times probed. The collapse in Fig. 6.4 is particularly notable because the lag times span both the superdiffusive and diffusive regimes. In both the previous case of tracers among swimming Chlamydomonas and in our case of tracers in an incipient biofilm, the non-Gaussian contributions to the probability distribution

function follow a Laplace distribution, so that the total PDF can described as the sum of two parts,

$$P(\Delta x) = \frac{1-f}{\sqrt{2\pi\sigma^2}} \exp\left[-\frac{1}{2}\frac{\Delta x^2}{\sigma}\right] + \frac{f}{\xi}\exp\left[-\frac{|\Delta x|}{\xi}\right] \tag{6.4}$$

The solid line in Fig. 6.4 is the result of a fit to the data using this form.

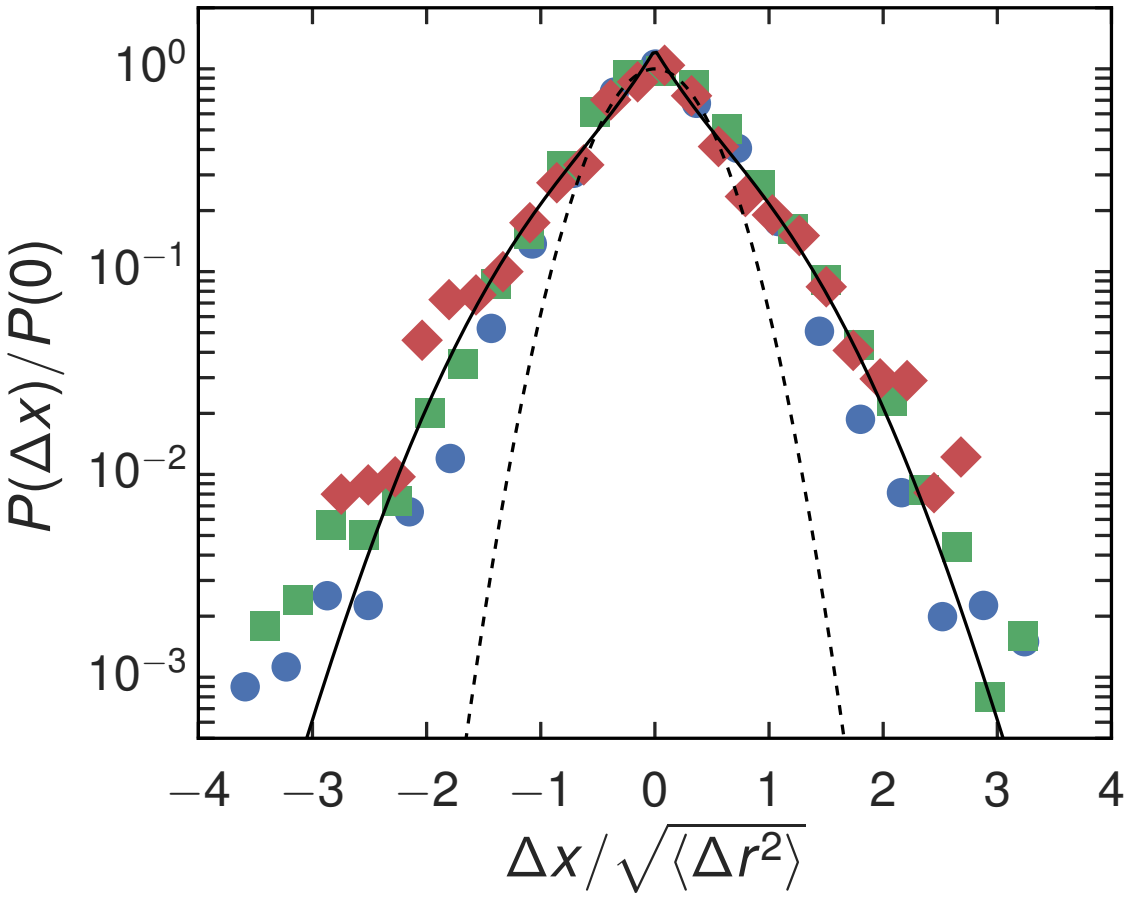

Figure 6.4: Normalized probability distribution functions from Figure 6.3 plotted against displacement normalized by the root mean squared displacement at each lag time, illustrating the collapse of the distributions onto a common lineshape. The dashed line displays the result of fitting a Gaussian lineshape in the regions of the peak. The solid line displays the result of a fit using the form given by Eq. 6.4

The strong similarity between the self-similar PDFs of tracer displacements in the incipient interfacial bacterial biofilm and those in bulk suspensions of Chlamydomonas is surprising since the tracer displacements in quasi-2D films of the Chlamydomonas suspensions display qualitatively different non-Gaussian distributions, and the authors of those studies attributed the difference to the differing fluid velocity fields generated by the force dipoles of the Chlamydomonas swimming in two and three dimensions.[165] Our case of colloids entrained at an oil interface of a suspension of swimming bacteria that are forming a biofilm has several features that distinguish it from these studies. First, the colloids, while in the incipient biofilm, were in contact with the aqueous subphase and hence were coupled hydrodynamically to bacteria both in the film and in the bulk, a situation that is in some sense a hybrid of the three-dimensional and quasi-two-dimensional systems considered previously. Second, as discussed below, biofilm formation substantially impacts the rheology of the interface even at the earliest ages, with possible qualitative consequences on the coupling between the swimming bacteria and the colloidal tracers in the film. Finally, Chlamydomonas is a "puller" while Pseudomonas sp. is a "pusher," and this distinction has consequences for the collective behavior and resulting hydrodynamics of suspensions. Given these distinctions, the strong correspondence between the PDFs in Fig. 6.4 and those from bulk Chlamydomonas suspensions suggests that such self-similar distributions with Gaussian and Laplacian components might emerge more generically in nonequilibrium active systems than previous thought.

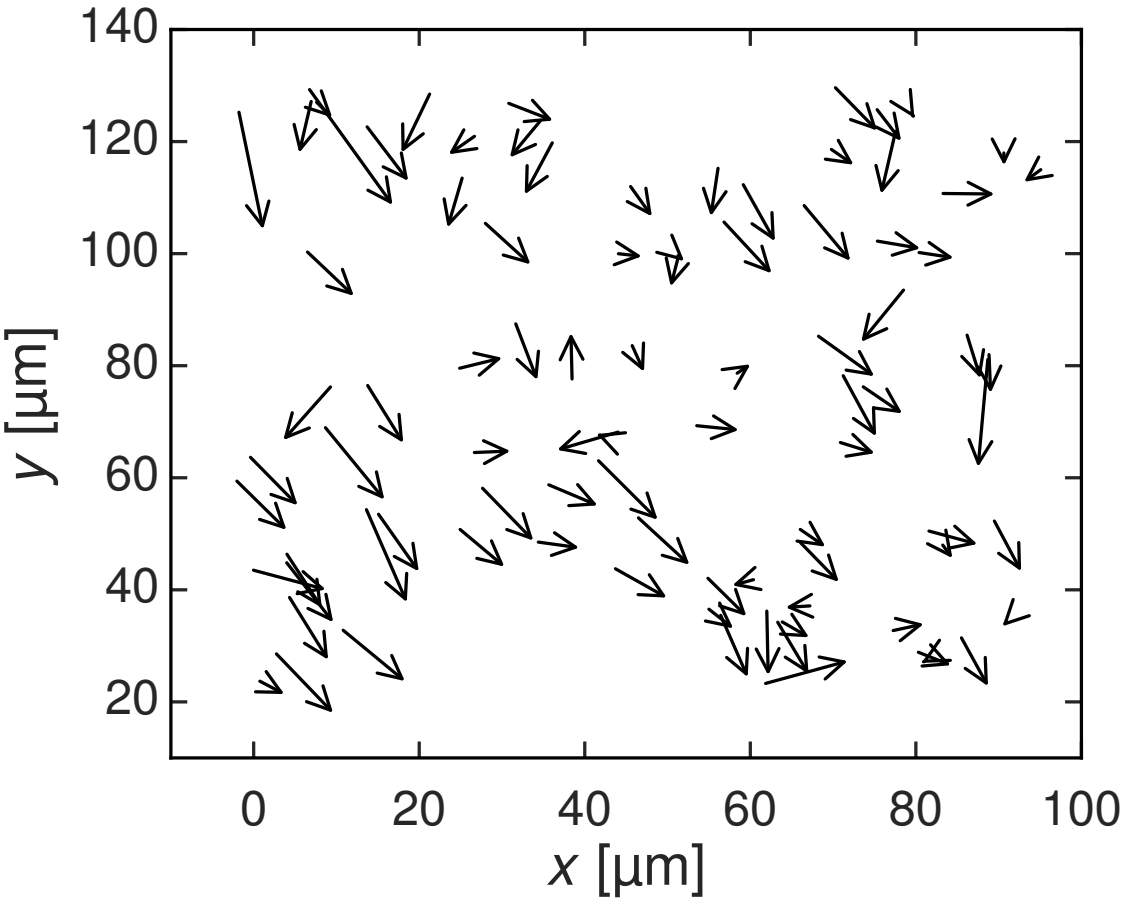

Figure 6.5: Map of a section of the interface during the active stage of biofilm formation showing the direction of motion of the colloidal tracers at an instant in time. Each colloid is represented by an arrowhead indicating its instantaneous motion $\vec{r}$.

Another feature of our study of the active stage was the density of colloidal probes at the interface, which was large enough that correlated motion among the colloids could be observed, thereby providing information about the spatial correlations of the non-Brownian kicks the swimming bacteria impose. As an illustration, Figure 6.5 depicts $\vec{r}$ for the colloids in the microscope field of view at one instant during the active stage. Alignment between the direction of motion of nearby colloids is clearly apparent. This coordinated motion is quantified in Fig. 6.6, which shows the normalized pair direction-direction correlation function,

$$C_n(r) = \langle \hat{n}_i \cdot \hat{n}_j \rangle_{i,j,t} \tag{6.5}$$

where the brackets represent an average over all pairs of particles i, j separated by distance r. The spatial correlations in tracer motion decay exponentially with separation, as depicted by the dashed line in Fig. 6.6, which is the result of an exponential fit to the data with correlation length of 4.7 ± 1.7 μm. Together, $G_n(t)$ and $C_n(r)$ give a quantitative picture of the short-time, spatiotemporal correlations in tracer motion that characterize the dynamical behavior of the interface during the initial, active stage of biofilm development.

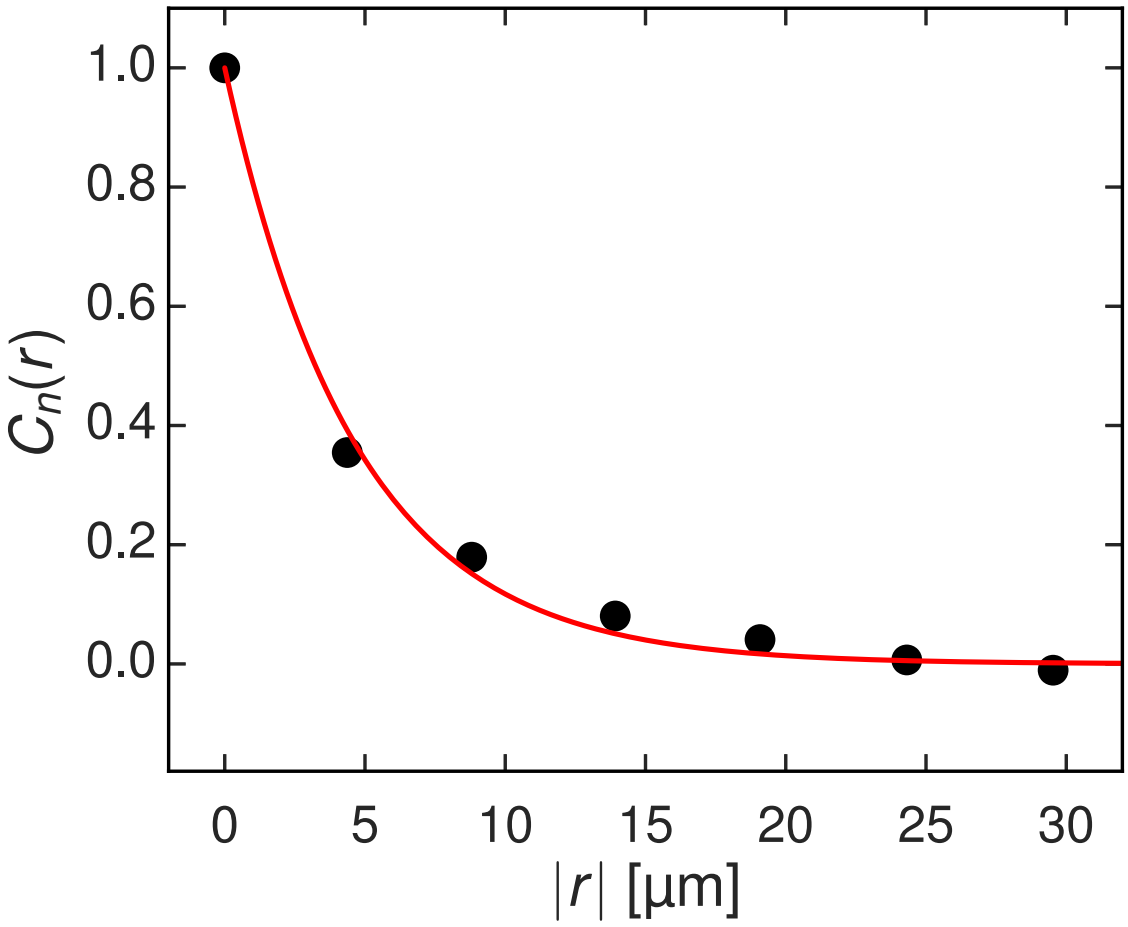

Figure 6.6: Normalized pair direction-direction correlation function as a function of the distance between colloids during the active stage of biofilm development.

6.3.2 Viscoelastic Transition

Typically, the initial active stage of the biofilm persisted for less than 5 minutes, after which no motile bacteria were observed either at the surface or in the near-surface bulk. We ascribe the limited duration of the bacteria motility to the lack of nutrient in the suspension. The end to the active stage was reflected in a qualitative change to the probe dynamics in which the probe mean-squared displacement changed from superdiffusive at short lag times to subdiffusive. Once the bacteria ceased to move visibly, we treated the interface as a passive system close to thermodynamic equilibrium and considered the probes to be undergoing thermally-driven Brownian trajectories from which the film rheology could be inferred.

As mentioned above, the active stage was not always observed. Significantly, the ensuing mechanical changes of the interface, as inferred from probe mobility, appeared qualitatively independent of whether it was preceded by an active stage. Furthermore, as discussed below, the evolution in film rheology persisted for many minutes after the end of the active stage, suggesting that the presence or absence of an active stage had limited impact on subsequent biofilm evolution. From these observations we conclude that the film formation was primarily the consequence of polysaccharides and surface-active moieties produced by the non-motile (resting) bacteria. However, we cannot discount the possibility of some subtle effects to biofilm formation due to biomixing by the swimming bacteria in those instances with an active stage.

Here, we present results for the viscoelastic evolution of the biofilm from an exper-

iment in which no protracted active stage was visible at the start of film formation. We focus on this data set because (i) the population of (non-motile) bacteria at the interface was limited, leaving a relatively unobstructed interface for the colloids and facilitating the analysis of their Brownian motion, and (ii) the colloidal motion was less likely to be affected by any residual activity than in a trial with a fully realized active stage. We emphasize again that the trends observed were qualitatively the same as those in trials in which the viscoelastic film development was preceded by an active stage.

Figure 6.7 shows the ensemble-averaged mean-squared displacement $\langle \Delta r^2(t) \rangle$ of the colloidal probes at several ages t_a of biofilm formation following creation of the interface. Because each mean-squared displacement is determined from 1 minute of video, the maximum lag time t is restricted to $t < 2$ s to assure adequate statistics. Again for reference, the mean-squared displacement of colloids diffusing at the oil interface of pure Instant Ocean containing no bacteria is also shown. At our earliest measurement of biofilm formation, the colloidal mean-squared displacement varies sublinearly with lag time, indicating a drag due to the development of a film with viscoelastic character.

Within the limited dynamic range of accessible lag times, $\langle \Delta r^2(t) \rangle$ is approximated as a power law, $\langle \Delta r^2(t) \rangle \sim t^n$, with $n < 1$. As shown in Fig. 6.8, the power-law exponent n decreases steadily with increasing age, signifying increasingly subdiffusive motion. While in principle the probe mobility is affected by both the interfacial

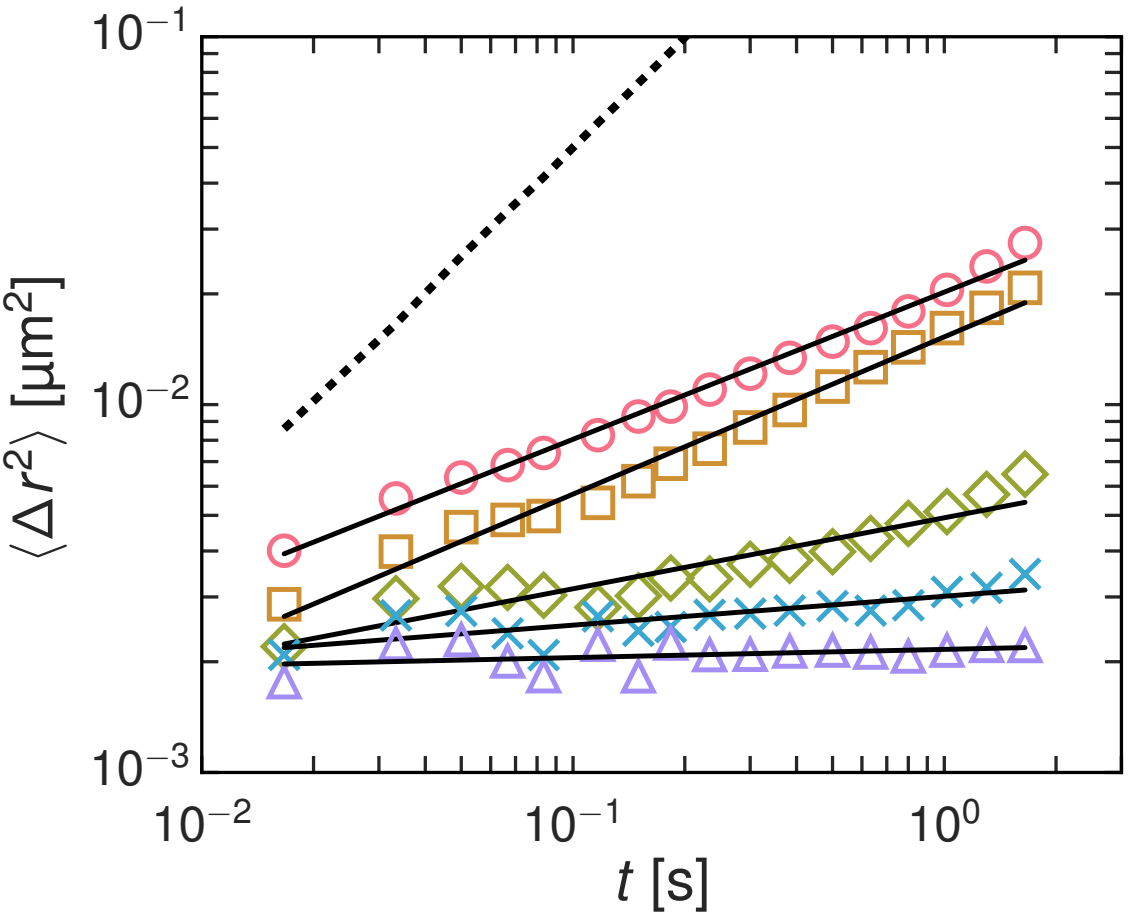

Figure 6.7: Ensemble-average mean squared displacement of colloids at several ages (red circles: 57 seconds, orange squares: 360, green diamonds: 1080, blue Xs: 10080, purple triangles: 88920) during biofilm formation at an oil-water interface for a trial with no active stage. For reference, the dashed line displays the mean squared displacement of colloids at the bare oil-water interface in the absence of bacteria. The solid lines display the result of power-law fits.

film and drag from the surrounding bulk oil and water, given the large difference between $\langle \Delta r^2(t) \rangle$ in the presence of the forming film and at the neat interface, we can safely infer that the bulk contributions to the drag are insignificant. In this case, under appropriate conditions one can obtain the frequency-dependent interfacial shear modulus, $G^*(\omega) = G'(\omega) + iG''(\omega)$, from the Brownian motion of the probes through a two-dimensional version of a generalized Stokes-Einstein relation,[23,105]

$$G^*(\omega) = \frac{k_B T}{\pi i \omega \mathcal{F}_u \{\langle \Delta r^2(t) \rangle\}} \tag{6.6}$$

where $\mathcal{F}_u \{\langle \Delta r^2(t) \rangle\}$ is the unilateral Fourier transform of the mean-squared displacement. Following Eq. (6.6, power-law behavior in the mean-squared displacements of the colloidal probes, $\langle \Delta r^2(t) \rangle \sim t^n$ with $n < 1$, implies the films shear modulus has power-law frequency dependence, $G'(\omega) \sim G''(\omega) \sim \omega^n$.[15]

As discussed in Chapter 4 in the context of the lysozyme layer, such weak power-law frequency dependence of $G^*(\omega)$ is characteristic of the rheology of a broad range of disordered complex fluids including concentrated microgel solutions,[132] foams,[133] paint,[134] intracellular matrix,[135] compressed emulsions,[14] clay suspensions,[136] and liquid-crystal nanocomposites[54] and is indicative of a broad spectrum of relaxation times. In most cases, the power-law exponent typically lies in the range $n \approx 0.1$ to 0.3. The soft glassy rheology model[55] explains this response as a general consequence of structural disorder and metastability, and provides a unifying theoretical framework for this behavior. In this model, n serves as an effective noise temperature, with

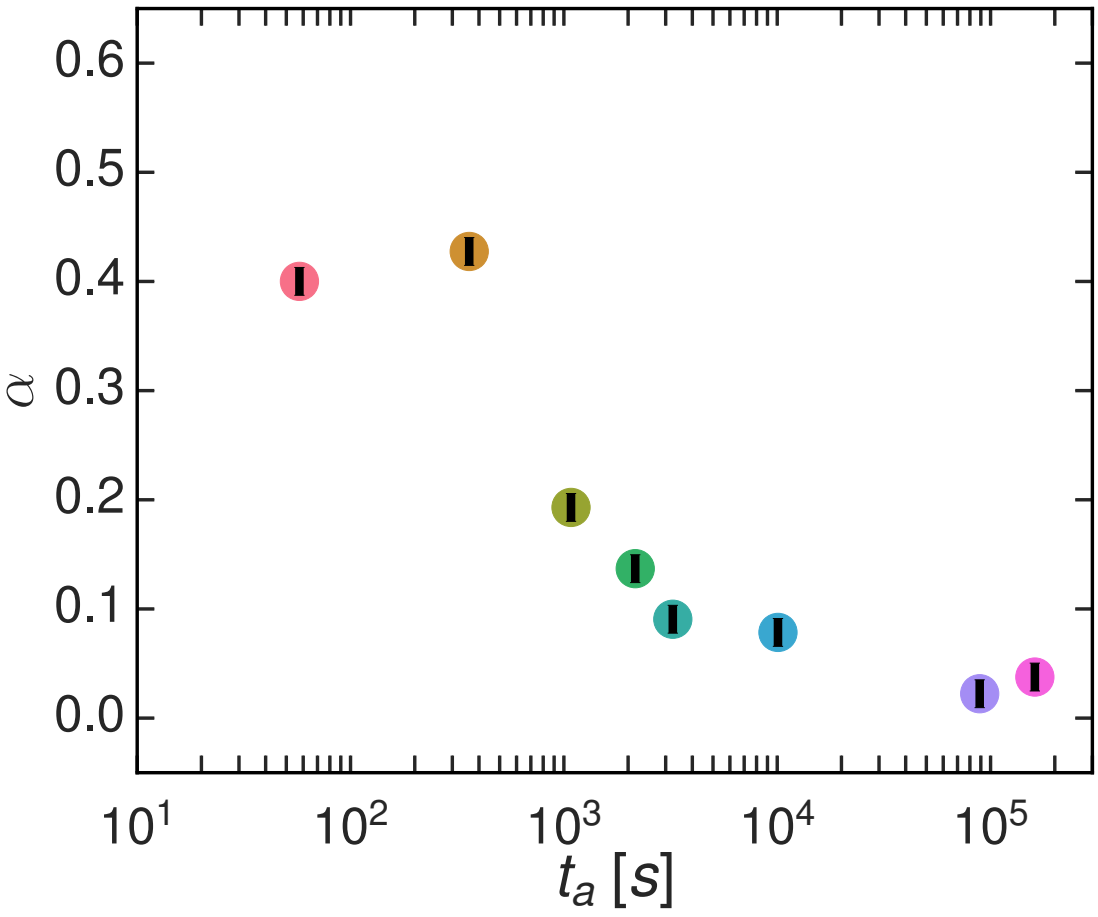

Figure 6.8: Power-law exponent characterizing the ensemble average mean-squared displacements, $\langle \Delta r^2(t) \rangle \sim t^{\alpha}$, of colloids the oil-bacteria solution interface as a function of the age since formation of the interface.

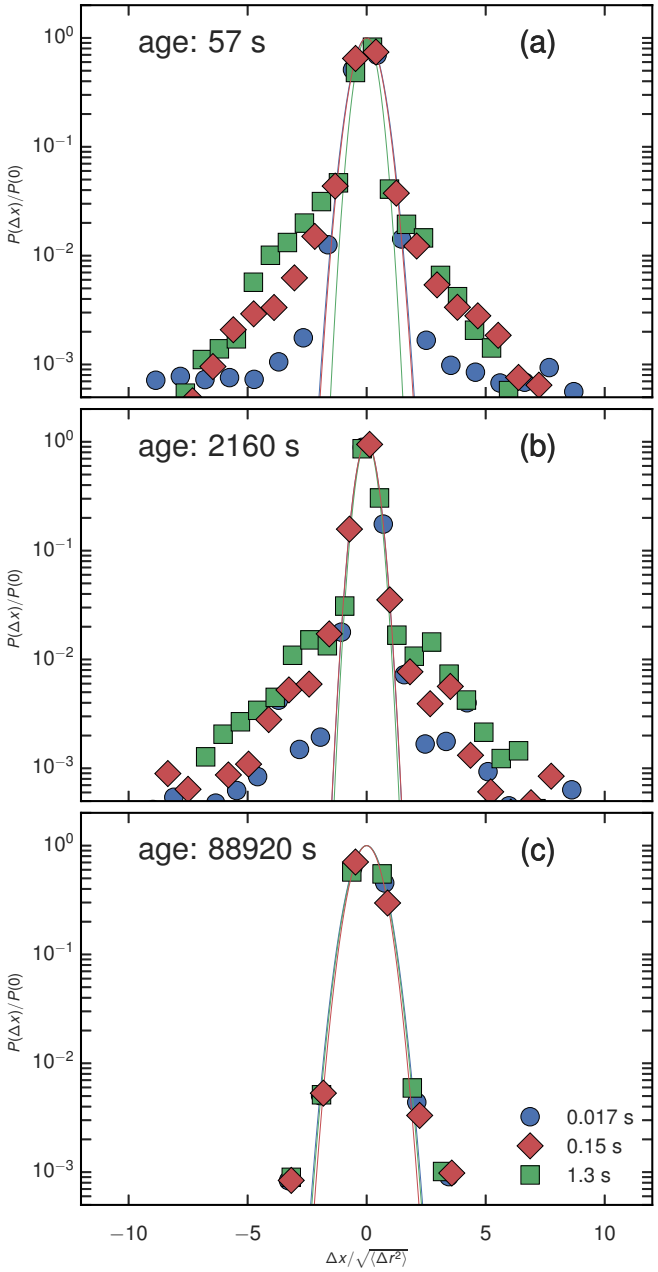

Figure 6.9: Normalized probability distribution functions for colloidal displacements at lag times of 0.016 s (blue), 0.15 s (green), and 1.3 s (red) at film ages (a) 57 s, (b) 2160 s, and (c) 88920 s during the viscoelastic stage of biofilm formation. The solid lines display the results of fitting Gaussian lineshapes in the regions of the peaks of the distributions, highlighting the enhanced, non-Gaussian probability for large displacements.

systems approaching a glass transition as $n \to 0$. Thus, the steady decrease in n with layer age reported in Fig. 6.8 points to increasingly glassy dynamics characterizing the structural response of the biofilm.

An important property of soft glassy systems is their non-equilibrium behavior and spatial heterogeneity. As a measure of these features, Figs. 6.9(a)-(c) show the PDFs of colloidal displacements at three ages during the viscoelastic transition. In each case, the PDF is shown at three lag times normalized by the mean-squared displacement at that lag time. At the earlier two ages, (t_a = 57 and 2160 s), during which the viscoelastic character of the film is evolving rapidly, the PDFs show a pronounced non-Gaussian components corresponding to enhanced probability of large displacements. These non-Gaussian contributions resemble those characterizing the colloidal dynamics in the active stage (Figs. 6.3 and 6.4); however, their origin in this case is different. Unlike at the active interface, the perturbations here are thermal, and each individual particle's displacements are Gaussian. The non-Gaussian distributions result from variation in the mobility of different particles, evincing a spatially heterogeneous interface of rheological microenvironments.[166] Surprisingly, this heterogeneity diminishes at late ages, as illustrated by the closer-to-Gaussian distributions in Fig. 6.9(c), when the interface's evolution has slowed and the film is nearly elastic. An interesting future study would be to compare this spatial heterogeneity with that of films formed in the presence of an extended stage of activity by swimming bacteria to investigate the role of biomixing in suppressing such heterogeneity.

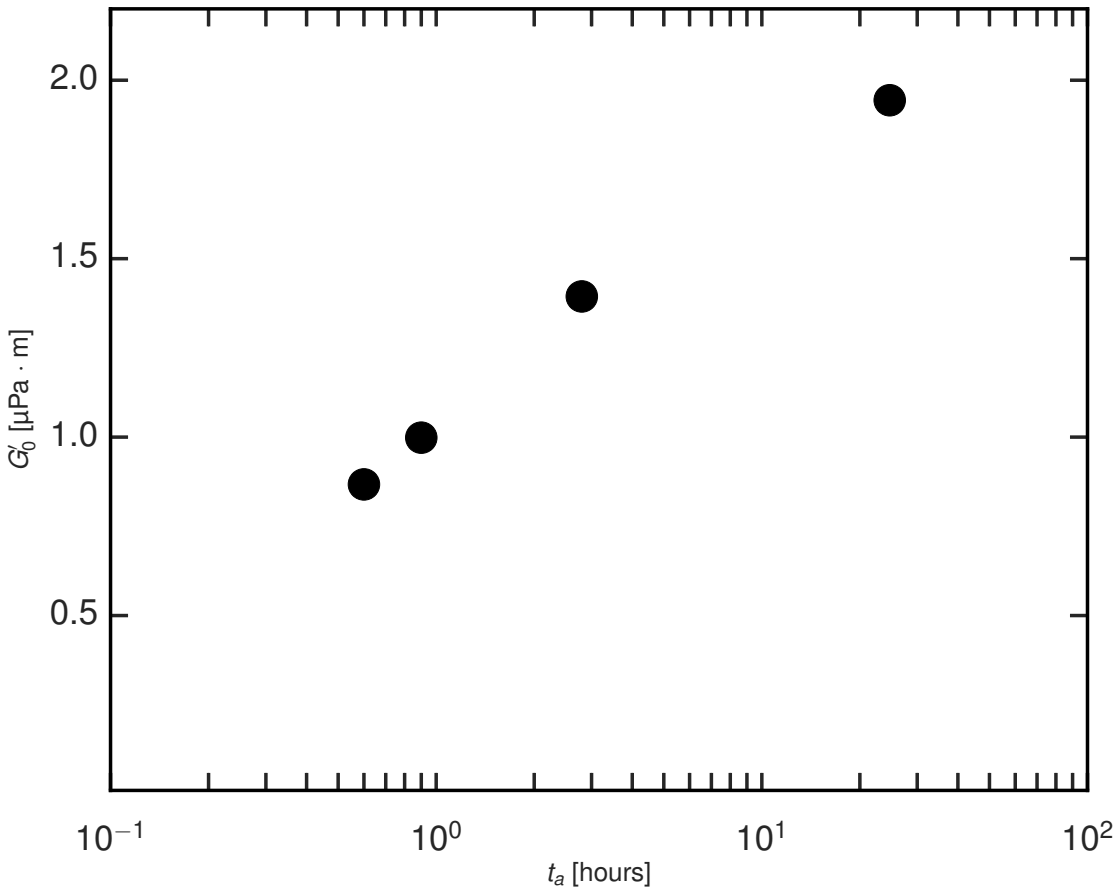

Figure 6.10: The interfacial elastic shear modulus G_0' at late ages, where the interface behaves like an elastic film. The elastic modulus grows logarithmically with age.

At late ages, when they layer behaves like an elastic film and $\langle \Delta r^2 \rangle$ asymptotes to a constant value, we can extract an interfacial elastic shear modulus G_0'.

$$G_0' = \frac{k_B T}{\langle \Delta r^2 (t \to \infty) \rangle} \tag{6.7}$$

As shown in Figure 6.10, we observe G_0' growing logarithmically with age. This has been observed by others in biofilms of Escherichia coli[167] and P. putida KT2442 and S. typhimurium.[168]

6.4 Conclusion

In this study, the dynamical and mechanical evolution of a bacterial biofilm at an oil–water interface was studied by tracking embedded colloidal particles, first as tracers among motile bacteria, then as passive microrheological probes. At early ages, an active stage could sometimes be observed, in which bacteria swimming near the interface or moving along the interface interacted hydrodynamically with the colloidal probes, driving superdiffusive motion. Once bacterial motility (if present) had ceased, the colloids could be used to measure the interfacial rheology. The films were found to be viscoelastic, becoming more elastic with age through the percolation of increasingly elastic patches and eventually forming a uniformly elastic film. The elastic shear modulus of the layer grew logarithmically with age. As mentioned above, these particle-tracking studies are part of a broader project that also includes pendant-

drop experiments that probe the biofilms' development of a bending rigidity at age ages. Taken as a whole, this combined study portrays a rich sequence of behaviors. Ultimately, these properties of the biofilm must be tied to the behavior of the bacteria that assures their viability. Further studies that can make such links would provide an insightful connection between biology and soft matter physics.

Chapter 7

Multiscale Nanoparticle Mobility Measurements in Biological Gels Using Photoactivatable Fluorescent Probes

7.1 Introduction

Drug-delivery nanoparticles often must diffuse through biological barriers to achieve therapeutic efficacy at their target site. In some instances, such as tear film at the ocular surface, the barrier is only a few micrometers thick.[169,170] In other cases, nanoparticles must penetrate tens of micrometers or more through viscoelas-

tic biological gels or tissue.[171–173] Measurements *in vitro* at physiologically relevant length scales are valuable for designing nanoparticles that will exhibit favorable *in vivo* biodistribution. Here, we present a strategy for measuring nanoparticle mobility in biological gels over length scales ranging from sub-micrometer to tens of micrometers using photoactivatable fluorescent probes. This work is part of a collaboration with Benjamin Schuster and Joshua Kays in the laboratory of Professor Justin Hanes in the Center for Nanomedicine of JHU.

The study involved polymeric nanoparticles with a dense polyethylene glycol (PEG) coating to minimize particle adhesion to the gel. The particle core was imbued with photoactivatable (caged) rhodamine, which becomes fluorescent only if the rhodamine is "uncaged" through momentary exposure to UV light. This functionality permitted us to selectively photoactivate a region of particles with a brief pulse of UV light, and then observe the spread of the fluorescent particles in the gel over tens of micrometers and tens of minutes, all using confocal microscopy. Complementing these measurements, we were also able to quantify the motion of the photoactivated particles at high spatiotemporal resolution — tens of nanometers and tens of milliseconds — using multiple particle tracking (MPT) on a widefield microscope. MPT has been harnessed recently to measure transport of drug delivery nanoparticles in many biological materials, including brain tissue,[171] mucus,[173–175] vitreous,[172] and inside cells.[73] MPT is a powerful technique that permits examination of individual particles and analysis of heterogeneous transport behavior. However, because of the limited

depth-of-field of high-numerical-aperture objectives, tracking particles diffusing in three dimensions for more than a few seconds and a few micrometers is difficult. The photoactivation method described here provides another approach to directly observe percolation through biological gels over longer distance and time scales. Hence, particle tracking and the photoactivation technique are complementary methods that, together, permit multiscale diffusion measurements.

We first confirmed agreement between measurements from MPT and the photoactivation technique on particles diffusing in water. Then, we applied our method to fibrin, a model protein gel system, and found that both MPT and the photoactivation method reveal mobile and immobile populations of particles. Finally, we examined nanoparticle diffusion in sputum collected from cystic fibrosis (CF) patients. Sputum is a major barrier to inhaled CF therapeutics, and our approach enabled us to measure particle diffusion over distances relevant to drug delivery in the lungs, revealing large-scale heterogeneity in the mobility that might be missed with techniques surveying motion over shorter length scales.

7.2 Experimental Methods

7.2.1 Materials

Cholalic acid sodium salt (CHA), NVOC2-5-carboxy-Q-rhodamine-NHS ester (caged rhodamine-NHS ester), N-hydroxysulfosuccinimide sodium salt (sulfo-NHS),

and N-(3-Dimethylaminopropyl)-N'-ethylcarbodiimide hydrochloride (EDC) were purchased from Sigma-Aldrich (St. Louis, MO). Poly(lactide-co-glycolide(75:25)) amine endcap (PLGA-NH2), Mn 10kDa-15kDa was purchased from Polyscitech (West Lafayette, IN). Poly(lactide-co-glycolide(67:33))-polyethylene glycol (45kDa-5kDa) diblock copolymer (PLGA-PEG) was custom-synthesized by Jinan Daigang Biomaterial Co., Ltd, (Jinan, China). 5 kDa methoxy-PEG-amine was purchased from Creative PEGWorks (Winston Salem, NC). Fluorescent carboxylate-modified polystyrene microspheres (PS-COOH) of diameter 100, 200, and 500 nm were purchased from Molecular Probes (Eugene, Oregon). Human α-thrombin (activity 3059 NIH U/ml) and human fibrinogen (plasminogen depleted, activity 100%) were purchased from Enzyme Research Laboratories (South Bend, IN).

7.2.2 Particles

The particles were designed and synthesized by my collaborators, Benjamin Schuster and Joshua Kays. Their protocol is presented here for context.

7.2.2.1 Labeling of PLGA with caged rhodamine

Caged rhodamine-NHS ester and PLGA-amine were conjugated through formation of an amide bond. Briefly, 90 mg of PLGA-NH2 was added to 5 mg of caged rhodamine-NHS ester (for a slight molar excess of dye compared to PLGA, 1:1.23) and put under vacuum for 1 h. The mixture was then flushed with nitrogen gas, dis-

solved in 500 µl of anhydrous dichloromethane (DCM), and reacted for 12 h at room temperature under nitrogen gas. Additional DCM was added as needed to facilitate transfer of the product into 10 ml of -20 °C diethyl ether to precipitate the product. The PLGA, now conjugated with rhodamine, was washed twice in cold ether by centrifugation. Excess ether was decanted off and the final product, the purified PLGA, was placed in a lyophilizer (FreeZone 4.5 Plus; Labconco) for 12 h. The dried PLGA was stored at -20 C in a shielded container to prevent exposure to incident UV light.

7.2.2.2 Particle formulation: PS-PEG

PEGylated polystrene (PS-PEG) particles were used a control in particle tracking experiments to verify that the mobility photoactivatable particles was the same as more widely used PS-PEG particles. PS-PEG particles were prepared as previously described[171] by coupling PS-COOH with PEG-amine using carbodiimide chemistry1. Generally, 100 µl of stock (2% solids) PS-COOH particle solution was added to borate buffer (pH 8) with 4 fold molar excess 5k mPEG-amine, EDC, and sulfo-NHS. The particles were reacted for at least 2 h, then washed three times by centrifugation and stored in DI water at 4 C.

7.2.2.3 Particle formulation: PLGA-PEG

Photoactivatable PLGA/PLGA-PEG nanoparticles were prepared by using the emulsion method according to the literature.[172] Briefly, a 40 mg mixture (19:1 by

mass) of PLGA-b-PEG5k and PLGA-caged rhodamine was dissolved in 400 μl of DCM, making a 100 mg/ml solution. This solution was injected into an ice-cooled 5 ml of 0.5% CHA aqueous solution, and sonicated at 30% amplitude for 2 min using a 130 Watt probe sonicator (Sonics & Materials, Newtown, CT) to form an oil-in-water emulsion of the organic phase (polymer and DCM) into the aqueous phase, stabilized by the CHA surfactant. The emulsion was immediately added to 35 ml of 0.5% CHA solution and stirred at 600 rpm for at least 3 h to allow for complete particle hardening. The final particle suspension was filtered through a 5 μm and then 0.45 μm syringe filter, then the particles were collected and washed three times via centrifugation at 20,000 g for 25 min. The particles are depicted in Figure **??** in a TEM image and in suspension in water, demonstrating their photo activatable capability.

7.2.2.4 Particle Characterization

The diameter and ζ-potential of the nanoparticles were determined by dynamic light scattering and laser Doppler electrophoresis, respectively, using a Zetasizer Nano ZS90 (Malvern Instruments, Southborough, MA). Transmission Electron Microscopy (TEM) images of dried particles were taken on standard 400 mesh copper TEM grids (TedPella, Redding, CA) with a Hitachi H7600 Electron Microscope. Particles were 160 ± 10 nm in diameter with a PDI of 0.11 ± 0.02 and a ζ-potential of -3 ± 1 mV, where error bars report variation between batches.

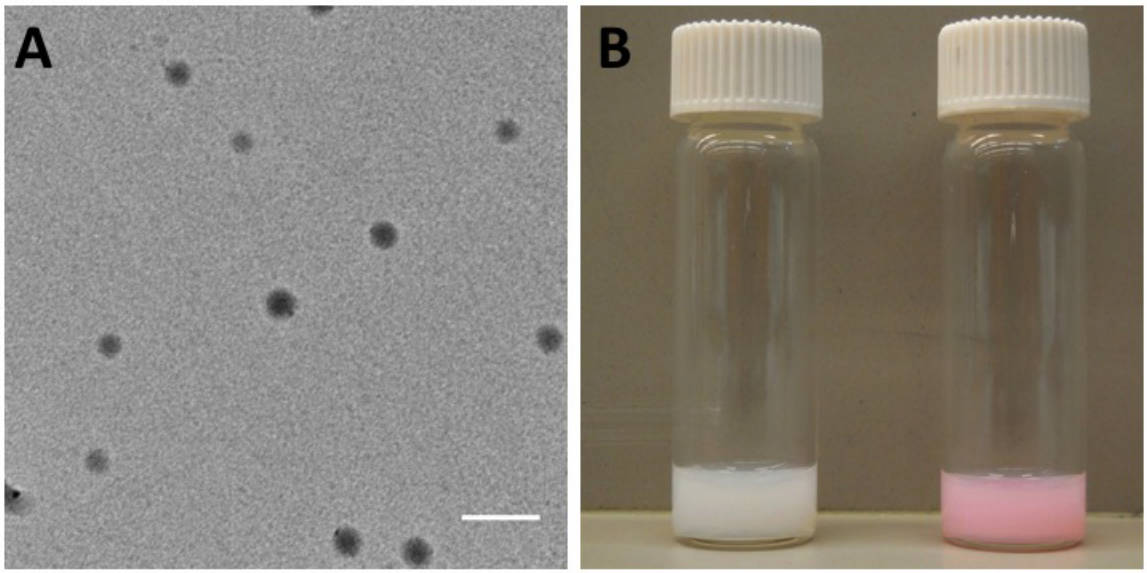

Panel A shows a TEM image of PLGA nanoparticles after dehydration. The white scale bar is 200 μm. Panel B shows the particles in suspension in water before (left) and after (right) UV light exposure, demonstrating the activation of the caged rhodamine.

7.2.3 Sample Preparation

7.2.3.1 Fibrin gel

Human fibrin gel was made from defrosted aliquots of thrombin and fibrinogen. Appropriate particle concentrations (between 0.005-0.00004% by mass) for tracking PS-PEG or PLGA-PEG particles were made in 2 U/ml thrombin in PBS, with a total volume of 180 μl. 20 μl of 40 mg/ml fibrinogen was pipetted to the solution, yielding a 4 mg/ml concentration of fibrinogen.[176] Vortex was immediately applied at high speed for 2 s to homogenize the solution. 30 μl of the solution was immediately pipetted into a 30 μl well on a glass slide, covered with a glass coverslip, and sealed with a cyanoacrylate glue. The slide was then incubated at 37 C for 20 min to ensure

gelation. In all cases, slides were wrapped in aluminum foil to prevent premature exposure to UV light.

7.2.3.2 CF Sputum

CFS was collected from adult patients at the Johns Hopkins Cystic Fibrosis Center in accordance with Institutional Review Board-approved protocols. Samples were stored at 4°C immediately after collection, and were analyzed the next day. CFS slides were made according to a similar procedure as the above for fibrin gels: 30 μl aliquots of CFS were withdrawn using a Wiretrol (Drummond Scientific Company, Broomall, PA) and injected into 30 μl wells on glass slides. 1 μl of appropriate particle suspensions for tracking or for photoactivation was added to the aliquot and mixed thoroughly. The slide was then sealed and allowed to incubate at room temperature for 1-2 hours (to prevent convection effects).

7.2.4 Measurements

7.2.4.1 Multiple Particle Tracking (MPT)

Particle motion in the CF sputum and fibrin samples was observed at room temperature using an inverted epifluorescence microscope (Axio Observer; Carl Zeiss, Thornwood, NY) with a 100X/1.46 NA oil-immersion objective. Movies were collected with 19-ms exposure at 20 fps for 500 frames using an EMCCD camera (Evolve

512; Photometrics, Tucson, AZ). Particle motion was tracked using the particle-tracking software described in Chapter 3.

7.2.4.2 Confocal imaging and photoactivation

Confocal imaging was performed on a Zeiss LSM510 laser scanning confocal microscope (Carl Zeiss, Thornwood, NY) in multi-tracking mode using either the 63x (Plan Apochromat 1.4 NA), 40x (PlanNeofluar 1.3 NA), or 20x (Plan Apochromat .75 NA) oil-immersion objective. Particles in the selected regions were activated by 10 to 25 iterations of the 405-nm laser at 100% power, while particles were excited to fluorescence by the 543-nm laser at 10–30% power. All videos were 512×512 pixels, and the activated region was 40×512 pixels. (For experiments performed using 20X, 40X and 63X objectives, this corresponds to 35×449, 18×225, or 11×143 μm^2, respectively.) Slide preparation for confocal experiments was identical to the above procedure for multiple particle tracking in CFS, with the exception of particle concentrations: PLGA-PEG particles were added to either water, CFS, or fibrin with final concentrations of 0.075% to 0.03% by mass.

7.3 Results

7.3.1 Water

Here we obtain the particles' diffusivity D in water from the evolution of the observed fluorescence intensity $I(x, y, t)$ from photoactivated particles. To begin, we will take the system to be homogenous, an assumption which of course holds for water, but which we must revisit when addressing more complex systems in later sections. Figure 7.1(a) displays a series of fluorescence images at different times following UV exposure to a strip-shaped region of the sample indicated by the red lines in the top image. We take the y-direction to be parallel to the strip and the x-direction to be perpendicular to it. The experiment is symmetric along y, and so the full image $I(x, y, t)$ can be summarized by an intensity profile $I(x, t) = \sum_y I(x, y, t)$. Under carefully tuned experimental conditions, intensity is directly proportional to the concentration of activated particles $c(x, t)$. Of course, this approximation is not universally applicable: particles overlap and scatter incident light and the emitted light from the particles around them, so at high concentrations the observed intensity must ultimately saturate. Also, the sensor imposes a sharp limit of the range of observable intensities. A carefully designed experiment, then, must match the particle concentration c and fluorescence (controlled in part by the intensity of incident light) to the sensitivity of camera. In our experiments, departures from the linear approximation $I \propto c$ were measurable but small, less than 5%.

In a viscous liquid such as water, the concentration profile evolves according to the diffusion equation:

$$\frac{\partial c}{\partial t} = D\frac{\partial^2 c}{\partial x^2} \tag{7.1}$$

An idealized, infinitely thin activation region at x' and time t', described by $c(x) = \delta(x - x')$, would evolve as a Gaussian that spreads during some time interval $t - t'$ as

$$c(x,t) = \frac{1}{\sqrt{4\pi D(t-t')}} \exp\left[-(x-x')^2/4D(t-t')\right] \tag{7.2}$$

This Gaussian is the Green function $G(x-x';t-t')$ for the diffusion equation. Therefore, for any distribution of activated particles $c(x',t')$ at time t', the distribution at some later time t will be

$$c(x,t) = \int_{-\infty}^{\infty} G(x-x';t-t')\, c(x',t')\, dx' \tag{7.3}$$

and therefore, if $I \propto c$,

$$I(x,t) = \int_{-\infty}^{\infty} G(x-x';t-t')\, I(x',t')\, dx'. \tag{7.4}$$

That is, the intensity profile at t' can be mapped onto the intensity profile at t through convolution with a Gaussian with width $\sigma = \sqrt{2D(t-t')}$. Breakdown of this mapping would indicate non-diffusive motion, which is not expected for water

but could occur in other materials.

During an experiment, hundreds of intensity profiles were captured at a regular interval. Every profile was mapped onto each future profile through convolution with a Gaussian, as in Eq. (7.4). The width σ of the Gaussian generating the most accurate mapping was determined using a nonlinear least-squares fit. Each mapping constituted a separate—though not strictly statistically independent—measurement of diffusivity D. Mappings corresponding to the same time interval $\Delta t = t - t'$ were averaged to produce the data points $\sigma^2(\Delta t)$ shown in Figure 7.1(c). Finally, an estimate of D was obtained through a linear regression to $\sigma^2(\Delta t)$. Its value, 2.4 $\pm$ 0.1 $\mu m^2/s$, is within 5% of the expected value for the diffusivity of 170-μm particles in water, thus demonstrating the utility of the photoactivation approach as a microrheology technique. Figure 7.1(d) shows the values of σ^2 from the photoactivation measurement along with those from MPT measurements. The two sets of results are consistent, and the figure indicates the complementary range of length and time scales each covers.

7.3.2 Fibrin

In experiments performed on samples of fibrin gel, some of the photoactivated nanoparticles spread with time outward from the activation region, but others remained immobilized, as evidenced by the still-bright activation region in Figure 7.2, which depicts the intensity 785 seconds after photoactivation. The mobile and immo-

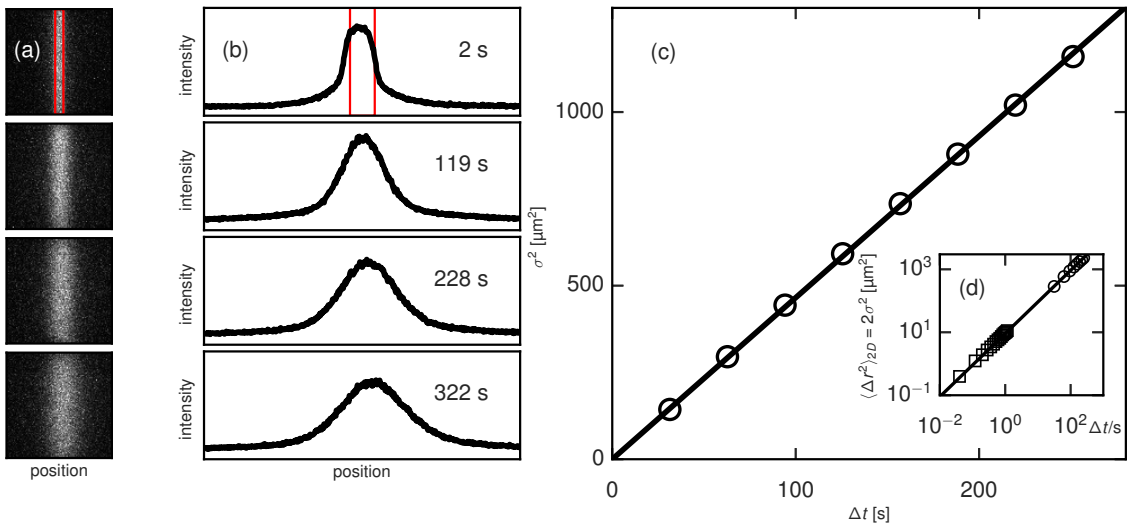

Figure 7.1: Photactivatable nanoparticles diffuse in water. (a) The region outlined in red, which is 34 microns wide, is momentarily exposed to UV laser light, and any particles within that region become fluorescent. (b) Their subsequent diffusion is characterized by an intensity profile representing the summed intensity of each individual column in the image. Profiles at different times can be mapped onto each other through convolution with a Gaussian, as described in the text. (c) The Gaussian that maps a given profile at any t' onto the profile at $t' + t$ has width $\sigma(t)$. This is related to the nanoparticles' diffusivity D through $\sigma^2 = 2Dt$. We extract the value D=2.4 $\pm$ 0.1 μm^2/s, which is within 5% of the theoretical diffusivity of 170-nm particles in water at room temperature. (d) The particles were also studied using traditional multiple-particle-tracking (MPT), where all particles were activated and individually tracked in two dimensions. The mean-squared displacement of their trajectories $\langle \Delta r^2 \rangle_{2D}$ (squares) is shown alongside the Gaussian widths from (c), plotted once again as circles. The diffusivity obtained from MPT was D=2.421 μm^2/s, in excellent agreement with the value obtained from photoactivation.

bile populations can separated by comparing the full intensity profile $I(x, t = 785\text{ s})$ to a Gaussian fit, where the fit is restricted to values of x outside the initial activation region and extrapolated to within the activation region (Figure 7.3). Comparing the integrated area of the Gaussian to the excess intensity in the activation region, we estimate that the mobile particles make up 40% of the total population. This fraction is compatible with our finding from MPT experiments in fibrin, which also show an approximately even split between mobile particles moving diffusively, $\langle \Delta r^2(t) \rangle \propto t$, and immobile particles characterized by a finite asymptotic MSD, $\langle \Delta r^2(t \to \infty) \rangle = \langle \Delta r^2 \rangle_0$. The MSDs of individual particles in fibrin derived from particle tracking are plotted in Figure 7.4, illustrating this division of mobility into two populations. A histogram of $\langle \Delta r^2(t = 1\text{ s})$, emphasizing the bimodal distribution of mobilities is shown in Figure 7.5.

We speculate that this bimodal distribution is a consequence of mesoscale heterogeneity in the fibrin gel that forms as a result of microphase separation during the gelation process. As the fibrogen polymerizes, the polymer solution undergoes spinodal decomposition. The phase separation is arrested, however, by the cross linking that locks in a bicontinuous structure of high and lower concentration gel. The porosity of the high-concentration regions is smaller than the particles, such that the particles are trapped in the gel. The fluorescence images directly capture this microstructure of the fibrin gel—the underlying spatial distribution of a polymer-rich phase, containing entrained particles, and a polymer-poor phase, which is essentially

a viscous liquid in which the particles freely diffuse. The apparent length scale of this micro-scale phase separation, visible in Figure 7.2, is about 10 μm, which is less than the typical linear spacing between particles in the MPT experiments. This result thereby illustrates another way in which photoactivation complements MPT: the higher particle densities in photoactivation experiments resolve underlying structural heterogeneity that gives rise to the dynamic heterogeneity in the MPT experiments. (MPT experiments cannot be performed at such high particle densities due to both experimental and fundamental limitations discussed in Chapter 2.)

7.3.3 Cystic Fibrosis Sputum

In particle-tracking studies, nanoparticles have been seen to diffuse through cystic fibrosis sputum (CFS)[173,175] over several micrometers, but in a CF patient the mucus barrier can be 20–50 μm thick, or more, so it is important to show that nanoparticles can actually traverse tens of microns, the distance necessary to deliver therapeutic nanoparticles to lung cells. Heterogeneity in CFS has been seen in these particle-tracking studies, and it is unknown what impact this heterogeneity has on the long-distance mobility of nanoparticles in the sputum.

In addition to heterogeneity within a sputum sample, there is also patient-to-patient variation, which has been found to be the larger of these two effects.[177] Characterization of nanoparticle mobility must contend with these variations. In our study, samples from one patient were found to be spatially homogeneous and approximately

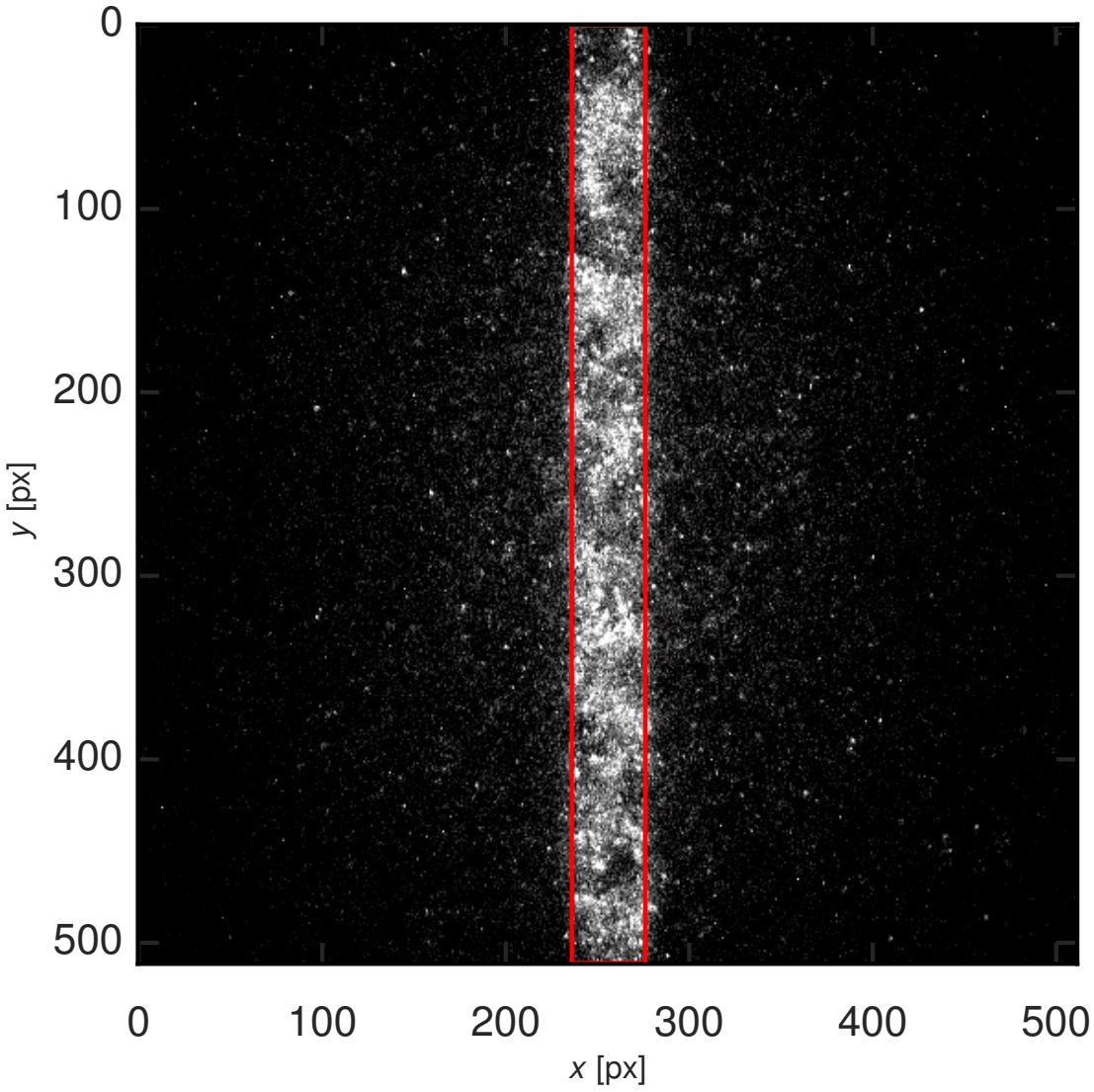

Figure 7.2: Fluorescence intensity from photoactivated nanoparticles in fibrin 785 seconds after those in the activation region (outlined in red) were activated with UV light. While some have spread outward as in Figure 7.1, the lingering intensity in the activation region shows that others remain immobilized in the immediate neighborhood of their initial position.

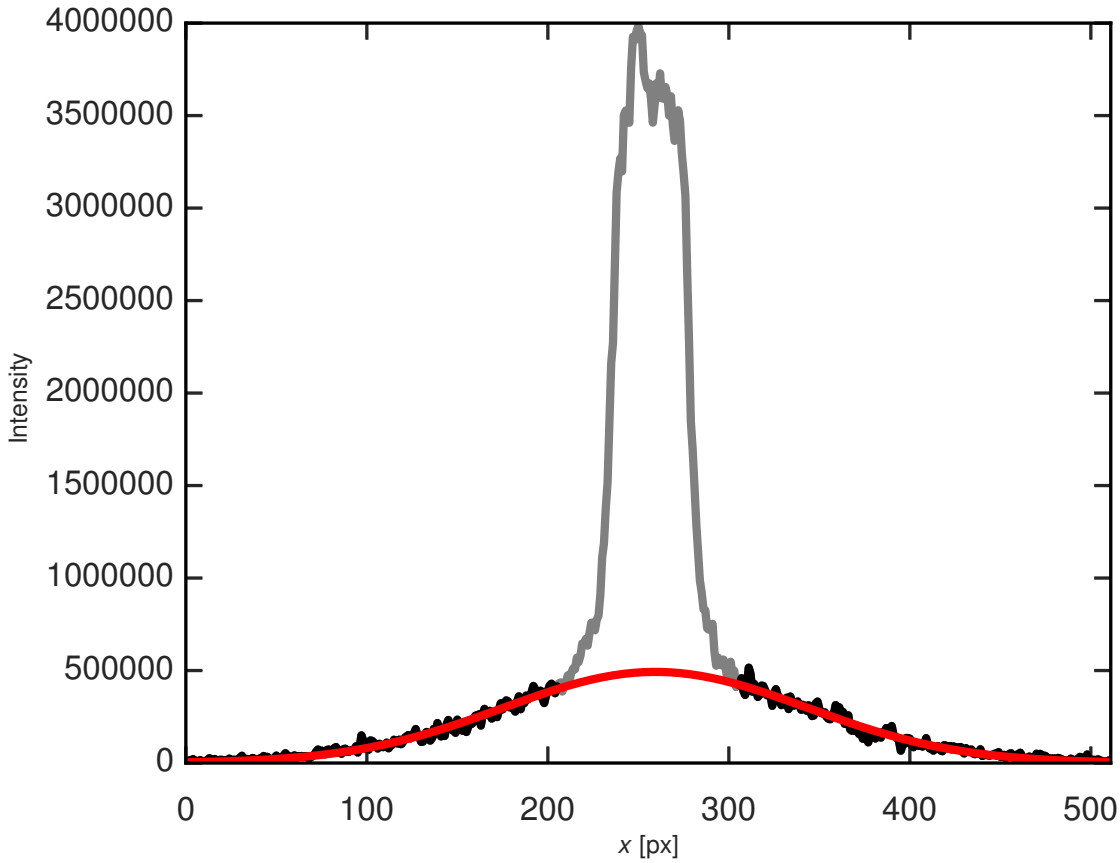

Figure 7.3: The gray-and-black curve shows the intensity profile $I(x,t)$ at t=785 seconds. In red is a Gaussian, fit only to the black portion of I outside the initial activation region. We posit that the intensity under the Gaussian is due to mobile particles that happen to be diffusing in that region while the intensity over the Gaussian is due to immobilized particles that are not diffusing.

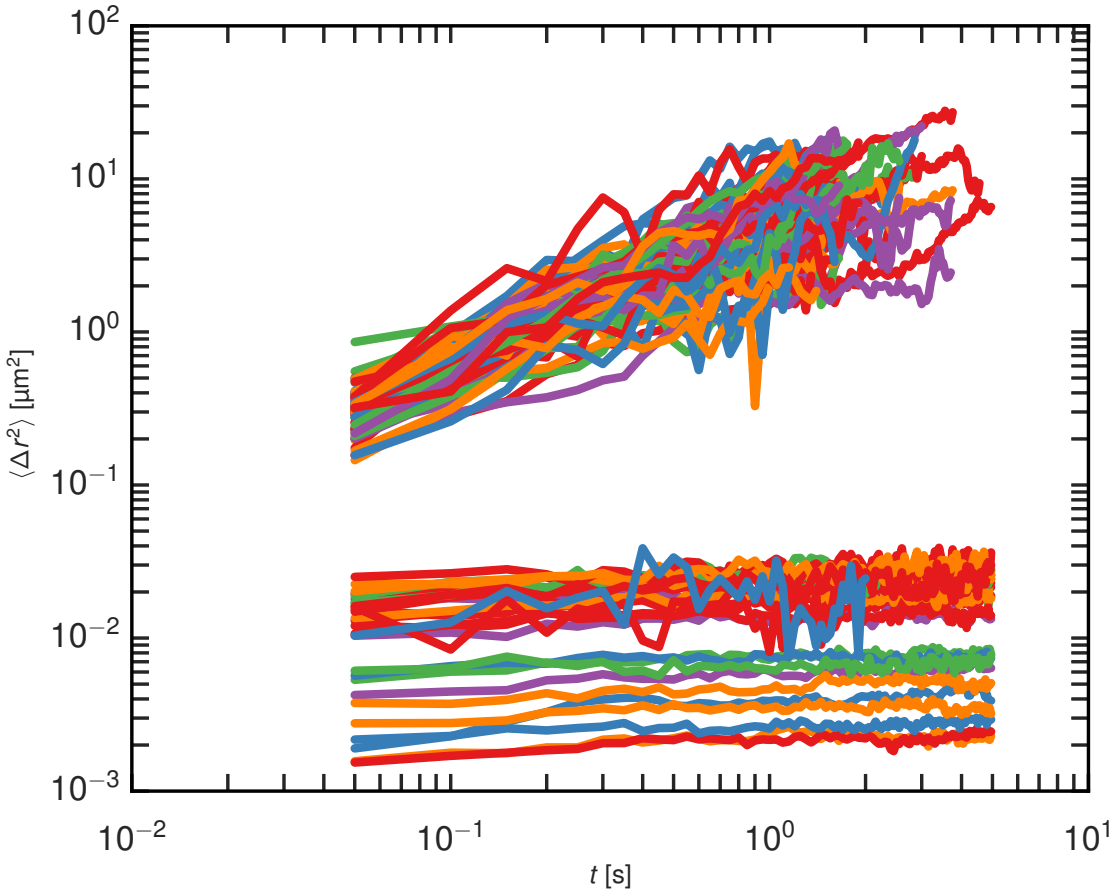

Figure 7.4: The MSD of individual PLGA-PEG particles in fibrin shows some particles moving diffusively and others jostling in place with an asymptotic MSD.

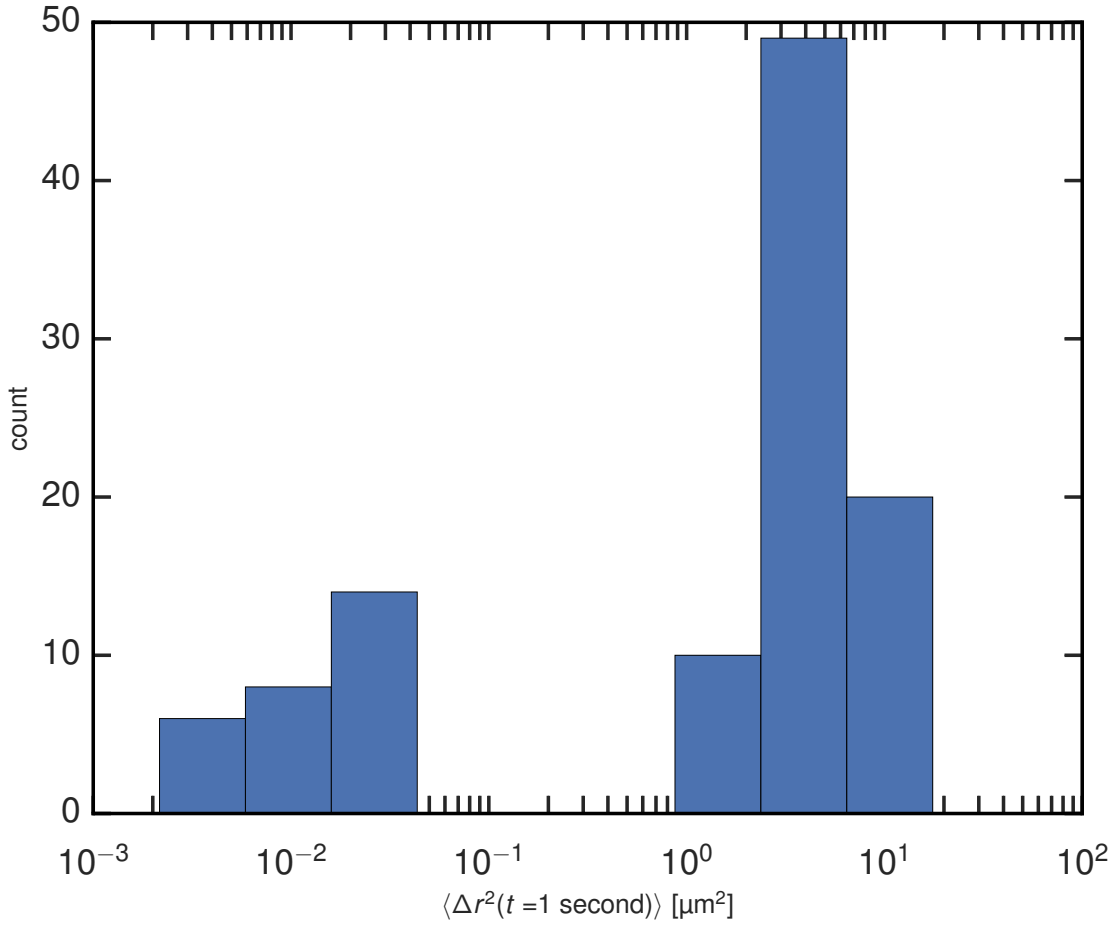

Figure 7.5: A histogram of the particles' MSD at lag time $t = 1$ second shows an approximately equal division between mobile and immobile populations.

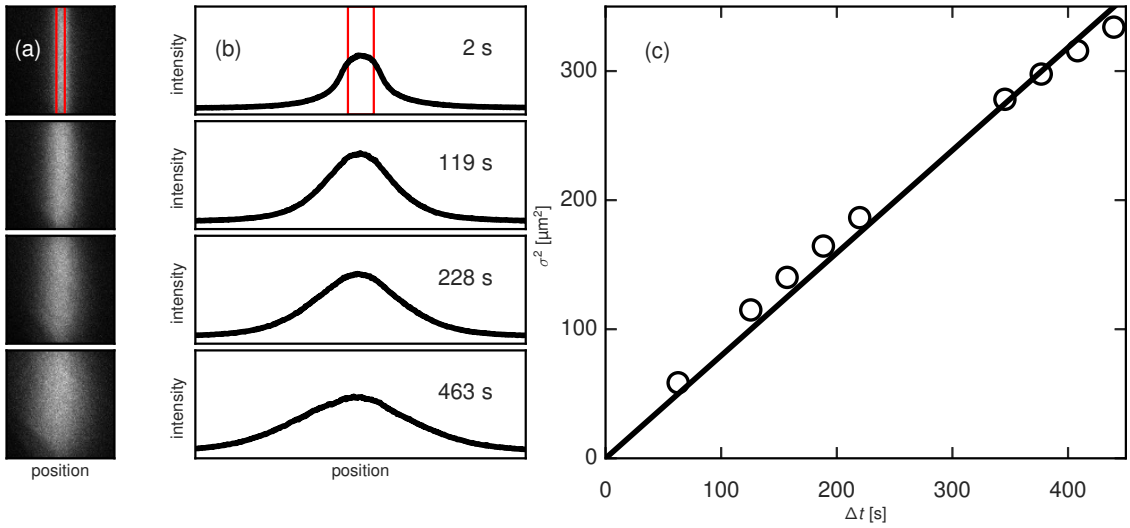

Figure 7.6: Photactivatable nanoparticles diffuse in sputum collected from a human cystic fibrosis patient. As in Figure 7.1: (a) The region outlined in red, which is 34 microns wide, is momentarily exposed to UV laser light, and any particles within that region become fluorescent. (b) Their subsequent diffusion is characterized by an intensity profile representing the summed intensity of each individual column in the image. Profiles at different times can be mapped onto each other through convolution with a Gaussian, as described in the text. (c) The Gaussian that maps a given profile at any t' onto the profile at $t' + t$ has width $\sigma(t)$. This is related to the nanoparticles' diffusivity D through $\sigma^2 = 2Dt$. We extract the value $D = 0.3944$ μm^2/s. (Missing data points are due to technical problems with video capture that, unfortunately, intermittently affected this particularly interesting trial.)

Newtonian. Thus, they were amenable to the same analysis performed on water above, as shown in Figure 7.6. From this analysis, we extract the diffusion coefficient $D = 0.3994$ μm^2/s, about an order of magnitude smaller than that in water.

Nanoparticle motion in samples from other patients was more complex and less amenable to straightforward application of such analysis. We observed mesoscale spatial heterogeneity, breaking the y-symmetry of the system, wherein the spreading particles made greater progress in certain subregions of the field of view. Illustrative

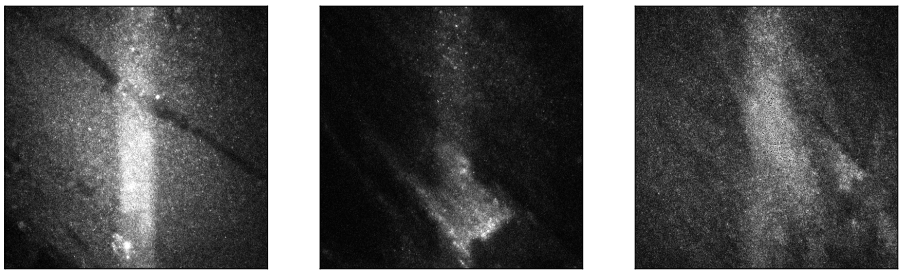

Figure 7.7: In samples from some patients, dramatic heterogeneity was observed. These images depect the fluorescence intensity of photoactivated nanoparticles in three different samples from the same patient. At left, long substructures in the fluid are not permeated by the nanoparticles. At center, the particles spread more easily in the region at the lower-right part of the frame. At right, both of these kinds of effects are evident. The left and right images are taken 600 seconds (10 minutes) after activation; the center, 1570 s.

examples are shown in Figure 7.7. On a basic level, we see that nanoparticles can traverse tens of micrometers, so from a practical point of view this shows that it is possible for a PEG-coated nanoparticles to traverse CF sputum over a distance necessary to deliver therapeutic nanoparticles. To our knowledge, this is a new result. Of course, from the uneven permeability observed in Figure 7.7, that delivery seems likely to be uneven across regions of the lung. Further, as with fibrin, photoactivation reveals the underlying microstructure of permeability that is difficult to discern from MPT analysis.

7.4 Discussion & Conclusion

We have developed a strategy of combining MPT with photoactivation for measuring nanoparticle diffusion in biological gels over multiple scales, ranging in time from tens of milliseconds to tens of minutes, and ranging in length from less than one micrometer to hundreds of micrometers.

The two techniques offer complimentary strengths. Particle tracking permits analysis of individual particles, and at high spatial and temporal resolutions, but the time and length of observation are limited. The photoactivation technique can monitor diffusion over longer times and distances, which are relevant in many drug-delivery applications, although spatial and temporal resolutions are not as good. Importantly, particle-tracking suffers from a sampling bias toward immobile particles, which stay in view longer and thus make up a disproportionate fraction of trackable particles.[73] The photoactivation technique, taking a wider view, captures the leading edge of diffusion and does not suffer from that particular bias.

In water, results from particle tracking and the photoactivation technique agree quantitatively. In fibrin, the two techniques portray compatible pictures of heterogeneous nanoparticle mobility. Finally, we directly observed PEG-coated PLGA nanoparticles diffusing over physiological distances in CFS and quantitified their diffusivity for one particular case that was unusually amenable to straightforward analysis. These findings extend prior, related work from the Hanes lab.[173]

Appendix A

Appendix

A.1 Trackpy Documentation

Trackpy, the particle-tracking software discussed Chapter 3, is thoroughly documented by the community of researchers who use and develop it. The documentation includes easy installation instructions, detailed tutorials, a reference guide, and much more. A large portion of the documentation was written as part of this thesis. It available online at `http://soft-matter.github.io/trackpy/`.

Bibliography

[1] J. R. Samaniuk and J. Vermant, "Micro and macrorheology at fluid-fluid interfaces." *Soft matter*, vol. 10, no. 36, pp. 7023–33, Sep. 2014. [Online]. Available: http://pubs.rsc.org/en/content/articlehtml/2014/sm/c4sm00646a

[2] J. Ferry, *Viscoelastic Properties of Polymers*. Wiley, 1980. [Online]. Available: http://books.google.com/books?id=9dqQY3Ujsx4C

[3] G. G. Fuller and J. Vermant, "Editorial: dynamics and rheology of complex fluidfluid interfaces," *Soft Matter*, vol. 7, no. 17, p. 7583, 2011. [Online]. Available: http://xlink.rsc.org/?DOI=c1sm90055b

[4] S. R. Derkach, J. Krägel, and R. Miller, "Methods of measuring rheological properties of interfacial layers (Experimental methods of 2D rheology)," *Colloid Journal*, vol. 71, no. 1, pp. 1–17, May 2009. [Online]. Available: http://link.springer.com/10.1134/S1061933X09010013

[5] A. Levine, T. Liverpool, and F. MacKintosh, "Mobility of extended bodies in viscous films and membranes," *Physical Review E*, vol. 69, no. 2, p. 021503,

Feb. 2004. [Online]. Available: http://link.aps.org/doi/10.1103/PhysRevE.69.021503

[6] G. G. Fuller and J. Vermant, "Complex fluid-fluid interfaces: rheology and structure." *Annual review of chemical and biomolecular engineering*, vol. 3, pp. 519–43, Jan. 2012. [Online]. Available: http://www.ncbi.nlm.nih.gov/pubmed/22541047http://www.annualreviews.org/doi/abs/10.1146/annurev-chembioeng-061010-114202?journalCode=chembioeng

[7] J. Boussinesq, "On the existence of a superficial viscosity grade, in the thin layer of transition which separates a liquid from another adjacent fluid," *Ann. Chim. Phys.*, vol. 29, pp. 349–57, 1913.

[8] S.-g. Oh and J. C. Slattery, "Disk and Biconical Interfacial Viscometers," *Journal of colloid and interface science*, vol. 67, no. 3, 1978.

[9] S. Vandebril, A. Franck, G. Fuller, P. Moldenaers, and J. Vermant, "A double wall-ring geometry for interfacial shear rheometry," *Rheologica Acta*, vol. 49, no. 2, pp. 131–144, 2010. [Online]. Available: http://dx.doi.org/10.1007/s00397-009-0407-3

[10] C. F. Brooks, G. G. Fuller, C. W. Frank, and C. R. Robertson, "An interfacial stress rheometer to study rheological transitions in monolayers at the airwater interface," *Langmuir*, vol. 15, no. 7, pp. 2450–2459, 1999. [Online]. Available: http://dx.doi.org/10.1021/la980465r

BIBLIOGRAPHY

[11] M. H. Lee, C. P. Lapointe, D. H. Reich, K. J. Stebe, and R. L. Leheny, "Interfacial hydrodynamic drag on nanowires embedded in thin oil films and protein layers." *Langmuir : the ACS journal of surfaces and colloids*, vol. 25, no. 14, pp. 7976–82, Jul. 2009. [Online]. Available: http://www.ncbi.nlm.nih.gov/pubmed/19594180

[12] M. H. Lee, D. H. Reich, K. J. Stebe, and R. L. Leheny, "Combined passive and active microrheology study of protein-layer formation at an air-water interface." *Langmuir : the ACS journal of surfaces and colloids*, vol. 26, no. 4, pp. 2650–8, Feb. 2010. [Online]. Available: http://www.ncbi.nlm.nih.gov/pubmed/19919016

[13] Z. A. Zell, A. Nowbahar, V. Mansard, L. G. Leal, S. S. Deshmukh, J. M. Mecca, C. J. Tucker, and T. M. Squires, "Surface shear inviscidity of soluble surfactants." *Proceedings of the National Academy of Sciences of the United States of America*, vol. 111, no. 10, pp. 3677–82, Mar. 2014. [Online]. Available: http://www.pnas.org/content/111/10/3677.full

[14] T. G. Mason, J. Bibette, and D. A. Weitz, "Letters." *Physical Review Letters*, vol. 75, no. 10, pp. 2051–2053, Feb. 1995. [Online]. Available: http://www.ncbi.nlm.nih.gov/pubmed/24573262

[15] T. G. Mason, "Estimating the viscoelastic moduli of complex uids using the

generalized Stokes Einstein equation," *Rheologica Acta*, vol. 39, pp. 371–378, 2000.

[16] T. M. Squires and T. G. Mason, "Fluid Mechanics of Microrheology," *Annual Review of Fluid Mechanics*, vol. 42, no. 1, pp. 413–438, Jan. 2010. [Online]. Available: http://www.annualreviews.org/doi/abs/10.1146/annurev-fluid-121108-145608

[17] T. Larsen and E. Furst, "Microrheology of the Liquid-Solid Transition during Gelation," *Physical Review Letters*, vol. 100, no. 14, p. 146001, Apr. 2008. [Online]. Available: http://link.aps.org/doi/10.1103/PhysRevLett.100.146001

[18] T. a. Waigh, "Microrheology of complex fluids," *Reports on Progress in Physics*, vol. 68, no. 3, pp. 685–742, Mar. 2005. [Online]. Available: http://stacks.iop.org/0034-4885/68/i=3/a=R04?key=crossref.13db41e971bf049d3528e867f566ccd9

[19] G. Saffman and M. Delbrock, "Brownian motion in biological membranes," *Proceedings of the National Academy of Sciences of the United States of America*, vol. 72, no. 8, pp. 3111–3113, 1975.

[20] B. D. Hughes, B. A. Pailthorpe, and L. R. White, "Extraction Of Membrane Microviscosity From Translational And Rotational," *Biophysical Journal*, vol. 37, no. March, pp. 673–676, 1982.

[21] E. P. Petrov and P. Schwille, "Translational diffusion in lipid membranes beyond the Saffman-Delbruck approximation." *Biophysical journal*, vol. 94, no. 5, pp. L41–3, Mar. 2008. [Online]. Available: http://www.pubmedcentral.nih.gov/articlerender.fcgi?artid=2242757&tool=pmcentrez&rendertype=abstract

[22] T. M. Fischer, P. Dhar, and P. Heinig, "The viscous drag of spheres and filaments moving in membranes or monolayers," *Journal of Fluid Mechanics*, vol. 558, no. 2006, p. 451, Jul. 2006. [Online]. Available: http://www.journals.cambridge.org/abstract_S002211200600022X

[23] A. Maestro, L. J. Bonales, H. Ritacco, T. M. Fischer, R. G. Rubio, and F. Ortega, "Surface rheology: macro- and microrheology of poly(tert-butyl acrylate) monolayers," *Soft Matter*, vol. 7, no. 17, p. 7761, 2011. [Online]. Available: http://xlink.rsc.org/?DOI=c1sm05225j

[24] D. Graham, M. Phillips, D. Mobius, and R. Miller, "Proteins at Liquid Interfaces," *Journal of Colloid and Interface Science*, vol. 70, no. 3, pp. 403–414, 1998. [Online]. Available: http://www.elsevier.com/wps/find/bookdescription.print/524544/description#description

[25] A. Saint-Jalmes, M.-L. Peugeot, H. Ferraz, and D. Langevin, "Differences between protein and surfactant foams: Microscopic properties, stability and coarsening," *Colloids and Surfaces A: Physicochemical and Engineering*

Aspects, vol. 263, no. 1-3, pp. 219–225, Aug. 2005. [Online]. Available: http://www.sciencedirect.com/science/article/pii/S0927775705001226

[26] D. J. McClements, "Protein-stabilized emulsions," *Current Opinion in Colloid & Interface Science*, vol. 9, no. 5, pp. 305–313, Dec. 2004. [Online]. Available: http://www.sciencedirect.com/science/article/pii/S1359029404000883

[27] C. Alonso, A. Waring, and J. A. Zasadzinski, "Keeping lung surfactant where it belongs: protein regulation of two-dimensional viscosity." *Biophysical journal*, vol. 89, no. 1, pp. 266–73, Jul. 2005. [Online]. Available: http://www.sciencedirect.com/science/article/pii/S000634950572676X

[28] G. B. Proctor, S. Hamdan, G. H. Carpenter, and P. Wilde, "A statherin and calcium enriched layer at the air interface of human parotid saliva." *The Biochemical journal*, vol. 389, no. Pt 1, pp. 111–6, Jul. 2005. [Online]. Available: http://www.pubmedcentral.nih.gov/articlerender.fcgi?artid=1184543&tool=pmcentrez&rendertype=abstract

[29] D. Graham and M. Phillips, "Proteins at liquid interfaces: molecular structures of adsorbed films," *Advances in colloid and interface science*, vol. 70, no. 30, pp. 427–429, Dec. 1978.

[30] M. A. Bos and T. van Vliet, "Interfacial rheological properties of adsorbed protein layers and surfactants: a review." *Advances in colloid and interface*

science, vol. 91, no. 3, pp. 437–71, Jul. 2001. [Online]. Available: http://www.ncbi.nlm.nih.gov/pubmed/11511044

[31] B. S. Murray, "Rheological properties of protein films," *Current Opinion in Colloid & Interface Science*, vol. 16, no. 1, pp. 27–35, Feb. 2011. [Online]. Available: http://linkinghub.elsevier.com/retrieve/pii/S1359029410000762

[32] G. B. Bantchev and D. K. Schwartz, "Surface Shear Rheology of -Casein Layers at the Air / Solution Interface : Formation of a Two-Dimensional Physical Gel," *Langmuir*, no. 15, pp. 2673–2682, 2003.

[33] S. a. Roberts, I. W. Kellaway, K. M. G. Taylor, B. Warburton, and K. Peters, "Combined surface pressure-interfacial shear rheology study of the effect of pH on the adsorption of proteins at the air-water interface." *Langmuir : the ACS journal of surfaces and colloids*, vol. 21, no. 16, pp. 7342–8, Aug. 2005. [Online]. Available: http://www.ncbi.nlm.nih.gov/pubmed/16042464

[34] E. M. Freer, K. S. Yim, G. G. Fuller, and C. J. Radke, "Interfacial Rheology of Globular and Flexible Proteins at the Hexadecane/Water Interface: Comparison of Shear and Dilatation Deformation," *The Journal of Physical Chemistry B*, vol. 108, no. 12, pp. 3835–3844, Mar. 2004. [Online]. Available: http://dx.doi.org/10.1021/jp037236k

[35] J. T. Petkov, T. D. Gurkov, B. E. Campbell, and R. P. Borwankar, "Dilatational and Shear Elasticity of Gel-like Protein Layers on Air/Water

Interface," *Langmuir*, vol. 16, no. 8, pp. 3703–3711, Apr. 2000. [Online]. Available: http://pubs.acs.org/doi/abs/10.1021/la991287k

[36] C. M. Wijmans and E. Dickinson, "Simulation of Interfacial Shear and Dilatational Rheology of an Adsorbed Protein Monolayer Modeled as a Network of Spherical Particles," *Langmuir*, vol. 14, no. 25, pp. 7278–7286, Dec. 1998. [Online]. Available: http://dx.doi.org/10.1021/la980687p

[37] P. A. Wierenga, H. Kosters, M. R. Egmond, A. G. J. Voragen, and H. H. J. de Jongh, "Importance of physical vs. chemical interactions in surface shear rheology." *Advances in colloid and interface science*, vol. 119, no. 2-3, pp. 131–9, Mar. 2006. [Online]. Available: http://www.ncbi.nlm.nih.gov/pubmed/16445882

[38] P. Cicuta and E. M. Terentjev, "Viscoelasticity of a protein monolayer from anisotropic surface pressure measurements." *The European physical journal. E, Soft matter*, vol. 16, no. 2, pp. 147–58, Feb. 2005. [Online]. Available: http://www.ncbi.nlm.nih.gov/pubmed/15729506

[39] P. Cicuta, E. Stancik, and G. Fuller, "Shearing or Compressing a Soft Glass in 2D: Time-Concentration Superposition," *Physical Review Letters*, vol. 90, no. 23, p. 236101, Jun. 2003. [Online]. Available: http://link.aps.org/doi/10.1103/PhysRevLett.90.236101

[40] P. Cicuta, "Compression and shear surface rheology in spread layers

of beta-casein and beta-lactoglobulin." *Journal of colloid and interface science*, vol. 308, no. 1, pp. 93–9, Apr. 2007. [Online]. Available: http://www.ncbi.nlm.nih.gov/pubmed/17234202

[41] R. Miller, R. Wüstneck, J. Krägel, and G. Kretzschmar, "Dilational and shear rheology of adsorption layers at liquid interfaces," *Colloids and Surfaces A: Physicochemical and Engineering Aspects*, vol. 111, no. 1-2, pp. 75–118, Jun. 1996. [Online]. Available: http://www.sciencedirect.com/science/article/pii/0927775795034927

[42] B. S. Murray, *Interfacial rheology of mixed food protein and surfactant adsorption layers with respect to emulsion and foam stability.* Elsevier: Amsterdam, 1998, vol. 7.

[43] D. B. Jones and A. P. J. Middelberg, "Micromechanical Testing of Interfacial Protein Networks Demonstrates Ensemble Behavior Characteristic of a Nanostructured Biomaterial," *Langmuir*, vol. 18, no. 14, pp. 5585–5591, Jul. 2002. [Online]. Available: http://dx.doi.org/10.1021/la020090g

[44] B. Rippner Blomqvist, M. J. Ridout, A. R. Mackie, T. Wärnheim, P. M. Claesson, and P. Wilde, "Disruption of viscoelastic beta-lactoglobulin surface layers at the air-water interface by nonionic polymeric surfactants." *Langmuir : the ACS journal of surfaces and colloids*, vol. 20, no. 23, pp. 10 150–8, Nov. 2004. [Online]. Available: http://dx.doi.org/10.1021/la0485475

[45] A. H. Martin, M. A. Cohen Stuart, M. A. Bos, and T. van Vliet, "Correlation between mechanical behavior of protein films at the air/water interface and intrinsic stability of protein molecules." *Langmuir : the ACS journal of surfaces and colloids*, vol. 21, no. 9, pp. 4083–9, Apr. 2005. [Online]. Available: http://dx.doi.org/10.1021/la047417t

[46] P. Erni, P. Fischer, E. J. Windhab, V. Kusnezov, H. Stettin, and J. Lauger, "Stress- and strain-controlled measurements of interfacial shear viscosity and viscoelasticity at liquid/liquid and gas/liquid interfaces," *Review of Scientific Instruments*, vol. 74, no. 11, p. 4916, Oct. 2003. [Online]. Available: http://scitation.aip.org/content/aip/journal/rsi/74/11/10.1063/1.1614433

[47] C. R. Vessely, J. F. Carpenter, and D. K. Schwartz, "Calcium-induced changes to the molecular conformation and aggregate structure of beta-casein at the air-water interface." *Biomacromolecules*, vol. 6, no. 6, pp. 3334–44, Jan. 2005. [Online]. Available: http://dx.doi.org/10.1021/bm050353w

[48] F. S. Ariola, A. Krishnan, and E. A. Vogler, "Interfacial rheology of blood proteins adsorbed to the aqueous-buffer/air interface." *Biomaterials*, vol. 27, no. 18, pp. 3404–12, Jun. 2006. [Online]. Available: http://www.sciencedirect.com/science/article/pii/S0142961206001359

[49] J. Krägel, S. R. Derkatch, and R. Miller, "Interfacial shear rheology of protein-surfactant layers." *Advances in colloid and interface science*,

vol. 144, no. 1-2, pp. 38–53, Dec. 2008. [Online]. Available: http://www.sciencedirect.com/science/article/pii/S0001868608001243

[50] P. Watnick and R. Kolter, "Biofilm, City of Microbes," *Journal of Bacteriology*, vol. 182, no. 10, pp. 2675–2679, May 2000. [Online]. Available: http://jb.asm.org/content/182/10/2675.short

[51] L. Cipelletti and L. Ramos, "Slow dynamics in glassy soft matter," *Journal of Physics: Condensed Matter*, vol. 17, no. 6, pp. R253–R285, Feb. 2005. [Online]. Available: http://stacks.iop.org/0953-8984/17/i=6/a=R01

[52] J. Mewis and N. J. Wagner, "Thixotropy." *Advances in colloid and interface science*, vol. 147-148, pp. 214–27, 2009. [Online]. Available: http://www.ncbi.nlm.nih.gov/pubmed/19012872

[53] J. R. Stokes and W. J. Frith, "Rheology of gelling and yielding soft matter systems," *Soft Matter*, vol. 4, no. 6, p. 1133, May 2008. [Online]. Available: http://pubs.rsc.org/en/content/articlehtml/2008/sm/b719677f

[54] R. Bandyopadhyay, D. Liang, R. Colby, J. Harden, and R. Leheny, "Enhanced Elasticity and Soft Glassy Rheology of a Smectic in a Random Porous Environment," *Physical Review Letters*, vol. 94, no. 10, p. 107801, Mar. 2005. [Online]. Available: http://link.aps.org/doi/10.1103/PhysRevLett.94.107801

[55] P. Sollich, "Rheological constitutive equation for a model of soft glassy

materials," *Physical Review E*, vol. 58, no. 1, pp. 738–759, Jul. 1998. [Online]. Available: http://link.aps.org/doi/10.1103/PhysRevE.58.738

[56] S. M. Fielding, P. Sollich, and M. E. Cates, "Aging and rheology in soft materials," *Journal of Rheology*, vol. 44, no. 2, p. 323, Mar. 2000. [Online]. Available: http://scitation.aip.org/content/sor/journal/jor2/44/2/10.1122/1.551088

[57] P. Coussot, "Rheophysics of pastes: a review of microscopic modelling approaches," *Soft Matter*, vol. 3, no. 5, p. 528, Apr. 2007. [Online]. Available: http://pubs.rsc.org/en/content/articlehtml/2007/sm/b611021p

[58] S. M. Fielding, M. E. Cates, and P. Sollich, "Shear banding, aging and noise dynamics in soft glassy materials," *Soft Matter*, vol. 5, no. 12, p. 2378, Jun. 2009. [Online]. Available: http://pubs.rsc.org/en/content/articlehtml/2009/sm/b812394m

[59] S. S. Rogers, C. V. D. Walle, and T. A. Waigh, "Microrheology of Bacterial Biofilms In Vitro : Staphylococcus aureus and Pseudomonas aeruginosa," *Langmuir*, vol. 67, no. 6, pp. 13 549–13 555, 2008.

[60] D. N. Hohne, J. G. Younger, and M. J. Solomon, "Flexible microfluidic device for mechanical property characterization of soft viscoelastic solids such as bacterial biofilms." *Langmuir : the ACS journal of*

surfaces and colloids, vol. 25, no. 13, pp. 7743–51, Jul. 2009. [Online]. Available: http://www.pubmedcentral.nih.gov/articlerender.fcgi?artid=2723186&tool=pmcentrez&rendertype=abstract

[61] J. N. Wilking, T. E. Angelini, A. Seminara, M. P. Brenner, and D. a. Weitz, "Biofilms as complex fluids," *MRS Bulletin*, vol. 36, no. 05, pp. 385–391, May 2011. [Online]. Available: http://www.journals.cambridge.org/abstract_S0883769411000716

[62] L. Pavlovsky, J. G. Younger, and M. J. Solomon, "In situ rheology of Staphylococcus epidermidis bacterial biofilms," *Soft Matter*, vol. 9, no. 1, p. 122, Nov. 2013. [Online]. Available: http://pubs.rsc.org/en/content/articlehtml/2013/sm/c2sm27005f

[63] H. Abbasnezhad, M. Gray, and J. M. Foght, "Influence of adhesion on aerobic biodegradation and bioremediation of liquid hydrocarbons." *Applied microbiology and biotechnology*, vol. 92, no. 4, pp. 653–75, Nov. 2011. [Online]. Available: http://www.ncbi.nlm.nih.gov/pubmed/21964551

[64] L. N. Warr, A. Friese, F. Schwarz, F. Schauer, R. J. Portier, L. M. Basirico, and G. M. Olson, "Bioremediating oil spills in nutrient poor ocean waters using fertilized clay mineral flakes: Some experimental constraints," *Biotechnology Research International*, vol. 2013, p. 19, 2013. [Online]. Available: http://dx.doi.org/10.1155/2013/704806

[65] G. E. Jenneman, R. M. Knapp, M. J. McInerney, D. Menzie, and D. Revus, "Experimental Studies of In-Situ Microbial Enhanced Oil Recovery," *Society of Petroleum Engineers Journal*, vol. 24, no. 01, pp. 33–37, Apr. 2013. [Online]. Available: https://www.onepetro.org/journal-paper/SPE-10789-PA

[66] Z. Kang, A. Yeung, J. M. Foght, and M. R. Gray, "Hydrophobic bacteria at the hexadecane-water interface: examination of micrometre-scale interfacial properties." *Colloids and surfaces. B, Biointerfaces*, vol. 67, no. 1, pp. 59–66, Nov. 2008. [Online]. Available: http://www.ncbi.nlm.nih.gov/pubmed/18778923

[67] ——, "Mechanical properties of hexadecane-water interfaces with adsorbed hydrophobic bacteria." *Colloids and surfaces. B, Biointerfaces*, vol. 62, no. 2, pp. 273–9, Apr. 2008. [Online]. Available: http://www.ncbi.nlm.nih.gov/pubmed/18093811

[68] D. A. Edwards, H. Brenner, and D. T. Wasan, *Interfacial transport processes and rheology*. Butterworth-Heinemann Boston, 1991, vol. 40.

[69] J. C. Crocker and D. G. Grier, "Microscopic Measurement of the Pair Interaction Potential of Charge-Stabilized Colloid," *Physical Review Letters*, vol. 60637, pp. 352–355, 1994.

[70] D. F. Williams, "9131724.pdf," Ph.D. dissertation, University of Washington,

1991. [Online]. Available: https://digital.lib.washington.edu/researchworks/bitstream/handle/1773/9912/9131724.pdf?sequence=1

[71] M. P. Lyne, "Electrostatic interactions between interfacial particles," Ph.D. dissertation, The University of British Columbia, 1989. [Online]. Available: https://circle.ubc.ca/handle/2429/27899

[72] T. Savin and P. S. Doyle, "Static and dynamic errors in particle tracking microrheology." *Biophysical journal*, vol. 88, no. 1, pp. 623–38, Jan. 2005. [Online]. Available: http://www.pubmedcentral.nih.gov/articlerender.fcgi?artid=1305040&tool=pmcentrez&rendertype=abstract

[73] J. C. Crocker and B. D. Hoffman, "Multiple-Particle Tracking and Two-Point Microrheology in Cells," *Cell*, vol. 83, no. 07, pp. 141–178, 2007.

[74] J. Crocker, "Methods of Digital Video Microscopy for Colloidal Studies," *Journal of Colloid and Interface Science*, vol. 179, no. 1, pp. 298–310, Apr. 1996. [Online]. Available: http://linkinghub.elsevier.com/retrieve/pii/S0021979796902179

[75] Y. Peng, W. Chen, T. M. Fischer, D. a. Weitz, and P. Tong, "Short-time self-diffusion of nearly hard spheres at an oilwater interface," *Journal of Fluid Mechanics*, vol. 618, p. 243, Dec. 2008. [Online]. Available: http://www.journals.cambridge.org/abstract_S0022112008004114

[76] A. Hultgren, M. Tanase, C. S. Chen, and D. H. Reich, "High-Yield Cell Separations Using Magnetic Nanowires," *IEEE Transactions on Magnetics*, vol. 40, no. 4, pp. 2988–2990, 2004.

[77] A. Hultgren, M. Tanase, E. J. Felton, K. Bhadriraju, A. K. Salem, C. S. Chen, and D. H. Reich, "Optimization of Yield in Magnetic Cell Separations Using Nickel Nanowires of Different Lengths," *Biotechnology Progress*, vol. 21, no. 2, pp. 509–515, 2005.

[78] L. Sun, P. C. Searson, and C. L. Chien, "Electrochemical deposition of nickel nanowire arrays in single-crystal mica films," *Applied Physics Letters*, vol. 74, no. 19, p. 2803, May 1999. [Online]. Available: http://scitation.aip.org/content/aip/journal/apl/74/19/10.1063/1.124019

[79] C. Chien, L. Sun, M. Tanase, L. Bauer, A. Hultgren, D. Silevitch, G. Meyer, P. Searson, and D. Reich, "Electrodeposited magnetic nanowires: arrays, field-induced assembly, and surface functionalization," *Journal of Magnetism and Magnetic Materials*, vol. 249, no. 1-2, pp. 146–155, Aug. 2002. [Online]. Available: http://www.sciencedirect.com/science/article/pii/S0304885302005231

[80] M. Tanase, "Ferromagnetic nanowires: Field-induced self-assembly, magneto-transport and biological applications," Ph.D. dissertation, Johns Hopkins University, 2004.

[81] H. Sugimura, A. Hozumi, T. Kameyama, and O. Takai, "Organosilane self-assembled monolayers formed at the vapour/solid interface," *Surface and Interface Analysis*, vol. 34, no. 1, pp. 550–554, Aug. 2002. [Online]. Available: http://doi.wiley.com/10.1002/sia.1358

[82] A. M. Fond, N. S. Birenbaum, E. J. Felton, D. H. Reich, and G. J. Meyer, "Preferential noncovalent immunoglobulin G adsorption onto hydrophobic segments of multi-functional metallic nanowires," *Journal of Photochemistry and Photobiology A: Chemistry*, vol. 186, no. 1, pp. 57–64, Feb. 2007. [Online]. Available: http://linkinghub.elsevier.com/retrieve/pii/S1010603006003996

[83] H. Shen, "Interactive notebooks: Sharing the code," *Nature*, vol. 515, no. 7525, pp. 151–152, Nov. 2014. [Online]. Available: http://www.nature.com/news/interactive-notebooks-sharing-the-code-1.16261

[84] B. J. Schnapp, J. Gelles, and M. P. Sheetz, "Nanometer-Scale Measurements Using Video Light Microscopy," *Cell Motility and the Cytoskeleton*, vol. 10, pp. 47–53, 1988.

[85] R. N. Ghosh and W. W. Webb, "Automated Detection and Tracking of Individual and Clustered Cell Surface Low Density Lipoprotein Receptor Molecules," *Biophysical journal*, vol. 66, no. May, pp. 1301–1318, 1994.

[86] P. Y. Huang, S. Kurasch, J. S. Alden, A. Shekhawat, A. A. Alemi, P. L. Mceuen, J. P. Sethna, U. Kaiser, and D. A. Muller, "Imaging atomic

rearrangements in two-dimensional silica glass: watching silica's dance." *Science (New York, N.Y.)*, vol. 342, no. 6155, pp. 224–7, Oct. 2013. [Online]. Available: http://www.sciencemag.org/content/342/6155/224

[87] Y. Xu, G. K. German, A. F. Mertz, and E. R. Dufresne, "Imaging stress and strain in the fracture of drying colloidal films," *Soft Matter*, vol. 9, no. 14, p. 3735, Mar. 2013. [Online]. Available: http://pubs.rsc.org/en/Content/ArticleHTML/2013/SM/C3SM27912J

[88] W. T. M. Irvine, V. Vitelli, and P. M. Chaikin, "Pleats in crystals on curved surfaces." *Nature*, vol. 468, no. 7326, pp. 947–51, Dec. 2010. [Online]. Available: http://dx.doi.org/10.1038/nature09620

[89] D. B. Allan, T. A. Caswell, and N. C. Keim, "Trackpy v0.2," May 2014. [Online]. Available: http://dx.doi.org/10.5281/zenodo.9971

[90] H. Deschout, K. Raemdonck, S. Stremersch, P. Maoddi, G. Mernier, P. Renaud, S. Jiguet, A. Hendrix, M. Bracke, R. Van den Broecke, M. Röding, M. Rudemo, J. Demeester, S. C. De Smedt, F. Strubbe, K. Neyts, and K. Braeckmans, "On-chip light sheet illumination enables diagnostic size and concentration measurements of membrane vesicles in biofluids." *Nanoscale*, vol. 6, no. 3, pp. 1741–7, Jan. 2014. [Online]. Available: http://www.ncbi.nlm.nih.gov/pubmed/24346038

[91] R. Parthasarathy, "Rapid, accurate particle tracking by calculation of radial

symmetry centers." *Nature methods*, vol. 9, no. 7, pp. 724–6, Jul. 2012. [Online]. Available: http://www.ncbi.nlm.nih.gov/pubmed/22688415

[92] R. E. Thompson, D. R. Larson, and W. W. Webb, "Precise Nanometer Localization Analysis for Individual Fluorescent Probes," *Biophysical journal*, vol. 82, no. May, pp. 2775–2783, 2002.

[93] N. Bobroff, "Position measurement with a resolution and noise-limited instrument," *Review of Scientific Instruments*, vol. 57, no. 6, p. 1152, 1986. [Online]. Available: http://scitation.aip.org/content/aip/journal/rsi/57/6/10.1063/1.1138619

[94] D. S. Martin, M. B. Forstner, and J. A. Ka, "Apparent Subdiffusion Inherent to Single Particle Tracking," *Biophysical Journal*, vol. 83, no. October, pp. 2109–2117, 2002.

[95] R. J. Ober, S. Ram, and E. S. Ward, "Localization Accuracy in Single-Molecule Microscopy," *Biophysical journal*, vol. 86, no. February, pp. 1185–1200, 2004.

[96] H. Deschout, K. Neyts, and K. Braeckmans, "The influence of movement on the localization precision of sub-resolution particles in fluorescence microscopy." *Journal of biophotonics*, vol. 5, no. 1, pp. 97–109, Jan. 2012. [Online]. Available: http://www.ncbi.nlm.nih.gov/pubmed/22083848

[97] H. C. Berg, "How to Track Bacteria," *Review of Scientific Instruments*, vol. 42,

no. 6, p. 868, 1971. [Online]. Available: http://scitation.aip.org/content/aip/journal/rsi/42/6/10.1063/1.1685246

[98] G. Wilson, D. a. Aruliah, C. T. Brown, N. P. Chue Hong, M. Davis, R. T. Guy, S. H. D. Haddock, K. D. Huff, I. M. Mitchell, M. D. Plumbley, B. Waugh, E. P. White, and P. Wilson, "Best practices for scientific computing." *PLoS biology*, vol. 12, no. 1, p. e1001745, Jan. 2014. [Online]. Available: http://www.pubmedcentral.nih.gov/articlerender.fcgi?artid=3886731&tool=pmcentrez&rendertype=abstract

[99] R. Walder, N. Nelson, and D. K. Schwartz, "Single Molecule Observations of Desorption-Mediated Diffusion at the Solid-Liquid Interface," *Physical Review Letters*, vol. 107, no. 15, p. 156102, Oct. 2011. [Online]. Available: http://link.aps.org/doi/10.1103/PhysRevLett.107.156102

[100] L. Rosenfeld, C. Cerretani, D. L. Leiske, M. F. Toney, C. J. Radke, and G. G. Fuller, "Structural and Rheological Properties of Meibomian Lipid," *Investigative Ophthalmology & Visual Science*, vol. 54, no. 4, pp. 2720–2732, 2013.

[101] B. S. Murray, "Interfacial rheology of food emulsifiers and proteins," *Current Opinion in Colloid & Interface Science*, vol. 7, no. 5-6, pp. 426–431, Nov. 2002. [Online]. Available: http://linkinghub.elsevier.com/retrieve/pii/S1359029402000778

[102] M. H. Lee, S. P. Cardinali, D. H. Reich, K. J. Stebe, and R. L. Leheny,

"Brownian dynamics of colloidal probes during protein-layer formation at an oilwater interface," *Soft Matter*, vol. 7, no. 17, p. 7635, 2011. [Online]. Available: http://xlink.rsc.org/?DOI=c1sm05235g

[103] P. Dhar, Y. Cao, T. M. Fischer, and J. a. Zasadzinski, "Active Interfacial Shear Microrheology of Aging Protein Films," *Physical Review Letters*, vol. 104, no. 1, p. 016001, Jan. 2010. [Online]. Available: http://link.aps.org/doi/10.1103/PhysRevLett.104.016001

[104] V. Prasad, S. Koehler, and E. Weeks, "Two-Particle Microrheology of Quasi-2D Viscous Systems," *Physical Review Letters*, vol. 97, no. 17, p. 176001, Oct. 2006. [Online]. Available: http://link.aps.org/doi/10.1103/PhysRevLett.97.176001

[105] E. Helfer, S. Harlepp, L. Bourdieu, J. Robert, F. MacKintosh, and D. Chatenay, "Viscoelastic properties of actin-coated membranes," *Physical Review E*, vol. 63, no. 2, p. 021904, Jan. 2001. [Online]. Available: http://link.aps.org/doi/10.1103/PhysRevE.63.021904

[106] A. K. Kandar, R. Bhattacharya, and J. K. Basu, "Interfacial microrheology as a tool to study viscoelastic transitions in nanoconfined soft matter," *Physical Review E*, vol. 81, no. 4, p. 041504, Apr. 2010. [Online]. Available: http://link.aps.org/doi/10.1103/PhysRevE.81.041504

[107] M. Sickert, F. Rondelez, and H. a. Stone, "Single-particle Brownian dynamics for characterizing the rheology of fluid Langmuir monolayers,"

Europhysics Letters (EPL), vol. 79, no. 6, p. 66005, Sep. 2007. [Online]. Available: http://stacks.iop.org/0295-5075/79/i=6/a=66005?key=crossref.a69f4541d09ee8ef2bb61634956df822

[108] S. Q. Choi, S. Steltenkamp, J. a. Zasadzinski, and T. M. Squires, "Active microrheology and simultaneous visualization of sheared phospholipid monolayers." *Nature communications*, vol. 2, no. May, p. 312, Jan. 2011. [Online]. Available: http://www.pubmedcentral.nih.gov/articlerender.fcgi?artid=3113294&tool=pmcentrez&rendertype=abstract

[109] K. Kim, S. Q. Choi, J. a. Zasadzinski, and T. M. Squires, "Interfacial microrheology of DPPC monolayers at the airwater interface," *Soft Matter*, vol. 7, no. 17, p. 7782, 2011. [Online]. Available: http://xlink.rsc.org/?DOI=c1sm05383c

[110] C. Y. Park, H. D. Ou-Yang, and M. W. Kim, "Interface shear microrheometer with an optically driven oscillating probe particle." *The Review of scientific instruments*, vol. 82, no. 9, p. 094702, Sep. 2011. [Online]. Available: http://www.ncbi.nlm.nih.gov/pubmed/21974607

[111] D. Murakami, U. Langer, Z. Khattari, and T. M. Fischer, "Fluorinated Langmuir monolayers are more viscous than non-fluorinated monolayers." *The journal of physical chemistry. B*, vol. 114, no. 16, pp. 5376–9, Apr. 2010. [Online]. Available: http://www.ncbi.nlm.nih.gov/pubmed/20373785

[112] C.-Y. Wu, Y. Song, and L. L. Dai, "Two-particle microrheology at oil-water interfaces," *Applied Physics Letters*, vol. 95, no. 14, p. 144104, 2009. [Online]. Available: http://scitation.aip.org/content/aip/journal/apl/95/14/10.1063/1.3243334

[113] U. Langer, A. Ray, S. Aliaskarisohi, and T. M. Fischer, "Elastic properties of nanoparticle monolayer foams." *The journal of physical chemistry. B*, vol. 116, no. 22, pp. 6439–42, Jun. 2012. [Online]. Available: http://www.ncbi.nlm.nih.gov/pubmed/22578010

[114] A. Martin, K. Grolle, M. Bos, M. Stuart, and T. Vanvliet, "Network Forming Properties of Various Proteins Adsorbed at the Air/Water Interface in Relation to Foam Stability," *Journal of Colloid and Interface Science*, vol. 254, no. 1, pp. 175–183, Oct. 2002. [Online]. Available: http://linkinghub.elsevier.com/retrieve/pii/S0021979702985929

[115] A. S. Malcolm, A. F. Dexter, and A. P. J. Middelberg, "Mechanical properties of interfacial films formed by lysozyme self-assembly at the air-water interface." *Langmuir : the ACS journal of surfaces and colloids*, vol. 22, no. 21, pp. 8897–905, Oct. 2006. [Online]. Available: http://www.ncbi.nlm.nih.gov/pubmed/17014133

[116] J. Lu, T. Su, P. Thirtle, R. Thomas, A. Rennie, and R. Cubitt, "The Denaturation of Lysozyme Layers Adsorbed at the Hydrophobic Solid/Liquid

Surface Studied by Neutron Reflection." *Journal of colloid and interface science*, vol. 206, no. 1, pp. 212–223, Oct. 1998. [Online]. Available: http://www.sciencedirect.com/science/article/pii/S0021979798956806

[117] J. R. Lu, T. J. Su, and B. J. Howlin, "The Effect of Solution pH on the Structural Conformation of Lysozyme Layers Adsorbed on the Surface of Water," *The Journal of Physical Chemistry B*, vol. 103, no. 28, pp. 5903–5909, Jul. 1999. [Online]. Available: http://pubs.acs.org/doi/abs/10.1021/jp990129z

[118] Y. F. Yano, T. Uruga, H. Tanida, H. Toyokawa, Y. Terada, M. Takagaki, and H. Yamada, "Driving force behind adsorption-induced protein unfolding: a time-resolved X-ray reflectivity study on lysozyme adsorbed at an air/water interface." *Langmuir : the ACS journal of surfaces and colloids*, vol. 25, no. 1, pp. 32–5, Jan. 2009. [Online]. Available: http://www.ncbi.nlm.nih.gov/pubmed/19072146

[119] C. Postel, O. Abillon, and B. Desbat, "Structure and denaturation of adsorbed lysozyme at the airwater interface," *Journal of Colloid and Interface Science*, vol. 266, no. 1, pp. 74–81, Oct. 2003. [Online]. Available: http://linkinghub.elsevier.com/retrieve/pii/S002197970300571X

[120] M. D. Lad, F. Birembaut, J. M. Matthew, R. a. Frazier, and R. J. Green, "The adsorbed conformation of globular proteins at the air/water interface."

Physical chemistry chemical physics : PCCP, vol. 8, no. 18, pp. 2179–86, May 2006. [Online]. Available: http://www.ncbi.nlm.nih.gov/pubmed/16751876

[121] P. B. Stathopulos, G. A. Scholz, Y.-m. Hwang, J. A. O. Rumfeldt, J. R. Lepock, and E. M. Meiering, "Sonication of proteins causes formation of aggregates that resemble amyloid," *Protein Science*, vol. 13, pp. 3017–3027, 2004.

[122] G. Velicelebit and J. M. Sturtevant, "Thermodynamics of the Denaturation of Lysozyme in Alcohol-Water Mixtures," *Biochemistry*, vol. 18, no. 7, pp. 1180–1186, 1979.

[123] P. Dhar, T. M. Fischer, Y. Wang, T. E. Mallouk, W. F. Paxton, and a. Sen, "Autonomously moving nanorods at a viscous interface." *Nano letters*, vol. 6, no. 1, pp. 66–72, Jan. 2006. [Online]. Available: http://www.ncbi.nlm.nih.gov/pubmed/16402789

[124] T. M. Fischer, "The drag on needles moving in a Langmuir monolayer," *Journal of Fluid Mechanics*, vol. 498, pp. 123–137, Jan. 2004. [Online]. Available: http://www.journals.cambridge.org/abstract_S0022112003006608

[125] A. Levine, T. Liverpool, and F. MacKintosh, "Dynamics of Rigid and Flexible Extended Bodies in Viscous Films and Membranes," *Physical Review Letters*, vol. 93, no. 3, p. 038102, Jul. 2004. [Online]. Available: http://link.aps.org/doi/10.1103/PhysRevLett.93.038102

[126] M. Tanase, L. A. Bauer, A. Hultgren, D. M. Silevitch, L. Sun, D. H. Reich, P. C. Searson, and G. J. Meyer, "Magnetic Alignment of Fluorescent Nanowires," *Nano Letters*, vol. 1, no. 3, pp. 155–158, Mar. 2001. [Online]. Available: http://dx.doi.org/10.1021/nl005532s

[127] A. Anguelouch, R. L. Leheny, and D. H. Reich, "Application of ferromagnetic nanowires to interfacial microrheology," *Applied Physics Letters*, vol. 89, no. 11, p. 111914, Sep. 2006. [Online]. Available: http://scitation.aip.org/content/aip/journal/apl/89/11/10.1063/1.2349841

[128] A. N. Alexandrou, T. M. McGilvreay, and G. Burgos, "Steady HerschelBulkley fluid flow in three-dimensional expansions," *Journal of Non-Newtonian Fluid Mechanics*, vol. 100, no. 1-3, pp. 77–96, Sep. 2001. [Online]. Available: http://linkinghub.elsevier.com/retrieve/pii/S0377025701001276

[129] A. Savitzky and M. J. E. Golay, "Smoothing and Differentiation of Data by Simplified Least Squares Procedures," *Analytical Chemistry*, vol. 36, no. 8, pp. 1627–1639, 1964.

[130] X. Huang and M. H. García, "A HerschelBulkley model for mud flow down a slope," *Journal of Fluid Mechanics*, vol. 374, no. September 2000, pp. 305–333, Nov. 1998. [Online]. Available: http://www.journals.cambridge.org/abstract_S0022112098002845

[131] F. D. Larrard, C. F. Ferraris, and T. Sedran, "Fresh concrete : A HerscheI-

Bulkley material," *Materials and Structures*, vol. 31, no. September, pp. 494–498, 1998.

[132] R. J. Ketz and W. W. Graessley, "Rheology of concentrated microgel solutions," *Rheologica Acta*, vol. 27, pp. 531–359, 1988.

[133] S. a. Khan, "Foam Rheology: III. Measurement of Shear Flow Properties," *Journal of Rheology*, vol. 32, no. 1, p. 69, 1988. [Online]. Available: http://link.aip.org/link/?JOR/32/69/1&Agg=doi

[134] M. Mackley, R. T. J. Marshall, and F. D. Zhao, "THE RHEOLOGICAL AND COLLOIDAL OF POLYMERIC v *_! J _," *Chemical Engineering Science*, vol. 49, no. 16, pp. 2551–2565, 1994.

[135] B. Fabry, G. Maksym, J. Butler, M. Glogauer, D. Navajas, and J. Fredberg, "Scaling the Microrheology of Living Cells," *Physical Review Letters*, vol. 87, no. 14, p. 148102, Sep. 2001. [Online]. Available: http://link.aps.org/doi/10.1103/PhysRevLett.87.148102

[136] D. Bonn, P. Coussot, H. T. Huynh, and F. Bertrand, "Rheology of soft glassy materials," *Europhysics Letters (EPL)*, vol. 59, no. 5, pp. 786–792, 2002.

[137] H. H. Winter, "Analysis of Linear Viscoelasticity of a Crosslinking Polymer at the Gel Point," *Journal of Rheology*, vol. 30, no. 2, p. 367, Apr. 1986. [Online].

Available: http://scitation.aip.org/content/sor/journal/jor2/30/2/10.1122/1.549853

[138] C. Veerman, K. Rajagopal, C. S. Palla, D. J. Pochan, J. P. Schneider, and E. M. Furst, "Gelation Kinetics of β-Hairpin Peptide Hydrogel Networks," *Macromolecules*, vol. 39, no. 19, pp. 6608–6614, Sep. 2006. [Online]. Available: http://dx.doi.org/10.1021/ma0609331

[139] J. S. Erickson, S. Sundaram, and K. J. Stebe, "Evidence that the Induction Time in the Surface Pressure Evolution of Lysozyme Solutions Is Caused by a Surface Phase Transition," *Langmuir*, vol. 16, no. 11, pp. 5072–5078, 2000.

[140] T. R. Garrett, M. Bhakoo, and Z. Zhang, "Bacterial adhesion and biofilms on surfaces," *Progress in Natural Science*, vol. 18, no. 9, pp. 1049–1056, Sep. 2008. [Online]. Available: http://www.sciencedirect.com/science/article/pii/S1002007108002049

[141] H. M. Dalton and P. E. March, "Molecular genetics of bacterial attachment and biofouling," *Current Opinion in Biotechnology*, vol. 9, no. 3, pp. 252–255, Jun. 1998. [Online]. Available: http://www.sciencedirect.com/science/article/pii/S0958166998800554

[142] H.-C. Flemming and J. Wingender, "The biofilm matrix." *Nature reviews. Microbiology*, vol. 8, no. 9, pp. 623–33, Sep. 2010. [Online]. Available: http://dx.doi.org/10.1038/nrmicro2415

[143] C. Kokare, S. Chakraborty, A. Khopade, and K. Mahadik, "Biofilm: Importance and applications," *Indian Journal of Biotechnology*, vol. 8, no. 2, pp. 159–168, 2009.

[144] S. Guelli de Souza, "Applications of biofilm in the degradation of contaminants in industrial effluents," *Signpost Open Journal of Biochemistry and Biotechnology*, vol. 1, no. 1, 2012.

[145] M. Rosenberg and E. Rosenberg, "Bacterial adherence at the hydrocarbon-water interface," *Oil and Petrochemical Pollution*, vol. 2, no. 3, pp. 155–162, Jan. 1985. [Online]. Available: http://www.sciencedirect.com/science/article/pii/S0143712785901784

[146] P. Stoodley, I. Dodds, J. D. Boyle, and H. M. Lappin-Scott, "Influence of hydrodynamics and nutrients on biofilm structure." *Journal of applied microbiology*, vol. 85 Suppl 1, pp. 19S–28S, Dec. 1998. [Online]. Available: http://www.ncbi.nlm.nih.gov/pubmed/21182689

[147] I. Klapper, C. J. Rupp, R. Cargo, B. Purvedorj, and P. Stoodley, "Viscoelastic fluid description of bacterial biofilm material properties." *Biotechnology and bioengineering*, vol. 80, no. 3, pp. 289–96, Nov. 2002. [Online]. Available: http://www.ncbi.nlm.nih.gov/pubmed/12226861

[148] J. N. Wilking, T. E. Angelini, A. Seminara, M. P. Brenner, and D. a. Weitz, "Biofilms as complex fluids," *MRS Bulletin*, vol. 36, no. 05, pp.

385–391, May 2011. [Online]. Available: http://www.journals.cambridge.org/abstract_S0883769411000716

[149] A. S. Griffin, S. A. West, and A. Buckling, "Cooperation and competition in pathogenic bacteria." *Nature*, vol. 430, no. 7003, pp. 1024–7, Aug. 2004. [Online]. Available: http://dx.doi.org/10.1038/nature02744

[150] L. Keller and M. G. Surette, "Communication in bacteria: an ecological and evolutionary perspective." *Nature reviews. Microbiology*, vol. 4, no. 4, pp. 249–58, Apr. 2006. [Online]. Available: http://dx.doi.org/10.1038/nrmicro1383

[151] A. Houry, M. Gohar, J. Deschamps, E. Tischenko, S. Aymerich, A. Gruss, and R. Briandet, "Bacterial swimmers that infiltrate and take over the biofilm matrix." *Proceedings of the National Academy of Sciences of the United States of America*, vol. 109, no. 32, pp. 13 088–93, Aug. 2012. [Online]. Available: http://www.pubmedcentral.nih.gov/articlerender.fcgi?artid=3420162&tool=pmcentrez&rendertype=abstract

[152] C. Wu, J. Y. Lim, G. G. Fuller, and L. Cegelski, "Quantitative analysis of amyloid-integrated biofilms formed by uropathogenic Escherichia coli at the air-liquid interface." *Biophysical journal*, vol. 103, no. 3, pp. 464–71, Aug. 2012. [Online]. Available: http://www.pubmedcentral.nih.gov/articlerender.fcgi?artid=3414876&tool=pmcentrez&rendertype=abstract

[153] J. Sheng and M. Molaei, "Bacterial encountering with oil droplet," *Bulletin of*

the American Physical Society, vol. Volume 59,, Nov. 2014. [Online]. Available: http://meetings.aps.org/Meeting/DFD14/Session/H9.2

[154] L. Lemelle, J.-F. Palierne, E. Chatre, and C. Place, "Counterclockwise circular motion of bacteria swimming at the air-liquid interface." *Journal of bacteriology*, vol. 192, no. 23, pp. 6307–8, Dec. 2010. [Online]. Available: http://www.pubmedcentral.nih.gov/articlerender.fcgi?artid=2981220&tool=pmcentrez&rendertype=abstract

[155] A. Be'er and R. M. Harshey, "Collective motion of surfactant-producing bacteria imparts superdiffusivity to their upper surface." *Biophysical journal*, vol. 101, no. 5, pp. 1017–24, Oct. 2011. [Online]. Available: http://www.pubmedcentral.nih.gov/articlerender.fcgi?artid=3164129&tool=pmcentrez&rendertype=abstract

[156] X.-l. Wu and A. Libchaber, "Particle Diffusion in a Quasi-Two-Dimensional Bacterial Bath," *Physical Review Letters*, vol. 84, no. 13, pp. 3017–3020, 2000.

[157] C. Dombrowski, L. Cisneros, S. Chatkaew, R. E. Goldstein, and J. O. Kessler, "Self-Concentration and Large-Scale Coherence in Bacterial Dynamics," *Physical Review Letters*, vol. 93, no. 9, p. 098103, Aug. 2004. [Online]. Available: http://link.aps.org/doi/10.1103/PhysRevLett.93.098103

[158] L. G. Wilson, V. a. Martinez, J. Schwarz-Linek, J. Tailleur, G. Bryant, P. N. Pusey, and W. C. K. Poon, "Differential Dynamic Microscopy of Bacterial

Motility," *Physical Review Letters*, vol. 106, no. 1, p. 018101, Jan. 2011. [Online]. Available: http://link.aps.org/doi/10.1103/PhysRevLett.106.018101

[159] G. Soni, B. Jaffar Ali, Y. Hatwalne, and G. Shivashankar, "Single Particle Tracking of Correlated Bacterial Dynamics," *Biophysical Journal*, vol. 84, no. 4, pp. 2634–2637, Apr. 2003. [Online]. Available: http://linkinghub.elsevier.com/retrieve/pii/S0006349503750681

[160] D. Chen, a. Lau, L. Hough, M. Islam, M. Goulian, T. Lubensky, and a. Yodh, "Fluctuations and Rheology in Active Bacterial Suspensions," *Physical Review Letters*, vol. 99, no. 14, p. 148302, Oct. 2007. [Online]. Available: http://link.aps.org/doi/10.1103/PhysRevLett.99.148302

[161] G. Miño, T. E. Mallouk, T. Darnige, M. Hoyos, J. Dauchet, J. Dunstan, R. Soto, Y. Wang, A. Rousselet, and E. Clement, "Enhanced Diffusion due to Active Swimmers at a Solid Surface," *Physical Review Letters*, vol. 106, no. 4, p. 048102, Jan. 2011. [Online]. Available: http://link.aps.org/doi/10.1103/PhysRevLett.106.048102

[162] A. Jepson, V. a. Martinez, J. Schwarz-Linek, A. Morozov, and W. C. K. Poon, "Enhanced diffusion of nonswimmers in a three-dimensional bath of motile bacteria," *Physical Review E*, vol. 88, no. 4, p. 041002, Oct. 2013. [Online]. Available: http://link.aps.org/doi/10.1103/PhysRevE.88.041002

[163] K. Leptos, J. Guasto, J. Gollub, A. Pesci, and R. Goldstein, "Dynamics

of Enhanced Tracer Diffusion in Suspensions of Swimming Eukaryotic Microorganisms," *Physical Review Letters*, vol. 103, no. 19, p. 198103, Nov. 2009. [Online]. Available: http://link.aps.org/doi/10.1103/PhysRevLett.103.198103

[164] I. Rushkin, V. Kantsler, and R. E. Goldstein, "Fluid Velocity Fluctuations in a Suspension of Swimming Protists," *Physical Review Letters*, vol. 105, no. 18, p. 188101, Oct. 2010. [Online]. Available: http://link.aps.org/doi/10.1103/PhysRevLett.105.188101

[165] H. Kurtuldu, J. S. Guasto, K. a. Johnson, and J. P. Gollub, "Enhancement of biomixing by swimming algal cells in two-dimensional films." *Proceedings of the National Academy of Sciences of the United States of America*, vol. 108, no. 26, pp. 10 391–5, Jun. 2011. [Online]. Available: http://www.pubmedcentral.nih.gov/articlerender.fcgi?artid=3127909&tool=pmcentrez&rendertype=abstract

[166] M. Valentine, P. Kaplan, D. Thota, J. Crocker, T. Gisler, R. Prudhomme, M. Beck, and D. Weitz, "Investigating the microenvironments of inhomogeneous soft materials with multiple particle tracking," *Physical Review E*, vol. 64, no. 6, p. 061506, Nov. 2001. [Online]. Available: http://link.aps.org/doi/10.1103/PhysRevE.64.061506

[167] C. Wu, J. Y. Lim, G. G. Fuller, and L. Cegelski, "Disruption of Escherichia

coli Amyloid-Integrated Bio fi lm Formation at the Air Liquid Interface by a Polysorbate Surfactant," *Langmuir*, vol. 29, no. 3, pp. 920–926, 2013.

[168] P. a. Rühs, L. Böcker, R. F. Inglis, and P. Fischer, "Studying bacterial hydrophobicity and biofilm formation at liquid-liquid interfaces through interfacial rheology and pendant drop tensiometry." *Colloids and surfaces. B, Biointerfaces*, vol. 117, pp. 174–84, May 2014. [Online]. Available: http://www.ncbi.nlm.nih.gov/pubmed/24632390

[169] P. E. King-Smith, B. A. Fink, N. Fogt, K. K. Nichols, R. M. Hill, and G. S. Wilson, "The thickness of the human precorneal tear film: evidence from reflection spectra." *Investigative ophthalmology & visual science*, vol. 41, no. 11, pp. 3348–59, Oct. 2000. [Online]. Available: http://www.ncbi.nlm.nih.gov/pubmed/11006224

[170] K. Azartash, J. Kwan, J. R. Paugh, A. L. Nguyen, J. V. Jester, and E. Gratton, "Pre-corneal tear film thickness in humans measured with a novel technique." *Molecular vision*, vol. 17, pp. 756–67, Jan. 2011. [Online]. Available: http://www.pubmedcentral.nih.gov/articlerender.fcgi?artid=3081798&tool=pmcentrez&rendertype=abstract

[171] E. A. Nance, G. F. Woodworth, K. A. Sailor, T.-Y. Shih, Q. Xu, G. Swaminathan, D. Xiang, C. Eberhart, and J. Hanes, "A dense poly(ethylene glycol) coating improves penetration of large polymeric nanoparticles within

brain tissue." *Science translational medicine*, vol. 4, no. 149, p. 149ra119, Aug. 2012. [Online]. Available: http://www.pubmedcentral.nih.gov/articlerender.fcgi?artid=3718558&tool=pmcentrez&rendertype=abstract

[172] Q. Xu, N. J. Boylan, S. Cai, B. Miao, H. Patel, and J. Hanes, "Scalable method to produce biodegradable nanoparticles that rapidly penetrate human mucus." *Journal of controlled release : official journal of the Controlled Release Society*, vol. 170, no. 2, pp. 279–86, Sep. 2013. [Online]. Available: http://www.pubmedcentral.nih.gov/articlerender.fcgi?artid=3730524&tool=pmcentrez&rendertype=abstract

[173] B. S. Schuster, J. S. Suk, G. F. Woodworth, and J. Hanes, "Nanoparticle diffusion in respiratory mucus from humans without lung disease." *Biomaterials*, vol. 34, no. 13, pp. 3439–46, Apr. 2013. [Online]. Available: http://www.pubmedcentral.nih.gov/articlerender.fcgi?artid=3590854&tool=pmcentrez&rendertype=abstract

[174] S. K. Lai, Y.-Y. Wang, D. Wirtz, and J. Hanes, "Micro- and macrorheology of mucus." *Advanced drug delivery reviews*, vol. 61, no. 2, pp. 86–100, Feb. 2009. [Online]. Available: http://www.pubmedcentral.nih.gov/articlerender.fcgi?artid=2736374&tool=pmcentrez&rendertype=abstract

[175] Y.-Y. Wang, S. K. Lai, J. S. Suk, A. Pace, R. Cone, and J. Hanes, "Addressing the PEG mucoadhesivity paradox to engineer nanoparticles

that "slip" through the human mucus barrier." *Angewandte Chemie (International ed. in English)*, vol. 47, no. 50, pp. 9726–9, Jan. 2008. [Online]. Available: http://www.pubmedcentral.nih.gov/articlerender.fcgi?artid=2666733&tool=pmcentrez&rendertype=abstract

[176] R. C. Spero, R. K. Sircar, R. Schubert, R. M. Taylor, A. S. Wolberg, and R. Superfine, "Nanoparticle diffusion measures bulk clot permeability." *Biophysical journal*, vol. 101, no. 4, pp. 943–50, Aug. 2011. [Online]. Available: http://www.pubmedcentral.nih.gov/articlerender.fcgi?artid=3175063&tool=pmcentrez&rendertype=abstract

[177] B. S. Schuster, "Probing and overcoming extracellular barriers to inhaled nanomedicine," Ph.D. dissertation, Johns Hopkins University, 2014.

Vita

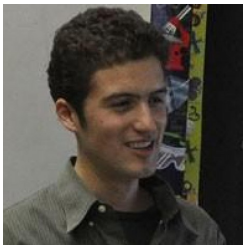

Dan Allan was raised in Corning, New York by a physicist and a schoolteacher. His first job was presenting a science demonstration on breaking glass at the Corning Museum of Glass, where he caused thousands of dollars of damage. He attended the University of Rochester as a Renaissance Scholar, where he earned bachelor's degrees in physics, music, and applied math. During his graduate studies at JHU, he has been active in Baltimore's Lindy Hop and choral singing communities.